Modelling of Batteries in Electric Vehicles

By

Parisa Amiribavandpour

A thesis submitted in fulfilment of the requirements for the degree of

Doctor of Philosophy

Faculty of Science, Engineering and Technology

Swinburne University of Technology
Hawthorn, Victoria, Australia
2017

Abstract

Electric vehicles (EVs) can be considered an ideal solution for transportation as they are pollutant free and independent of petroleum. Of all cell chemistries, Lithium-ion (Li-ion) batteries are the best candidate for energy storage systems in EVs due to their high specific energy, high power and high discharge capacity. Despite the rapid growth of Li-ion applications in the EV market, its market share in the automotive industry remains limited. In addition to high battery cost, Li-ion batteries suffer from poor performance in different conditions. They are highly temperature dependent and temperature affects several aspects of the batteries in the operation of EVs: charge acceptance, power and energy capability, reliability, safety issues (e.g. thermal runaway) and life. There is thus an urgent need to explore Li-ion battery cell and battery pack performance and safety to understand their performance in EVs in different conditions.

To understand the fundamental principles of Li-ion batteries and battery packs and determine their suitability for particular applications, modelling and numerical simulation is a better option than costly and time-consuming experimental tests. Moreover, modelling indicates detailed physical field information inside the battery, impossible to obtain by experiments. Thus, modelling and numerical simulation was used to study thermal phenomena of battery packs in constant current discharge and EV driving cycle based variable currents, crucial for designing EV thermal management systems.

Coupled electrochemical-thermal models are generally more accurate than empirical models or black-box neural network models as these only simulate battery behaviours from the input-output point of view while neglecting the mass transfer balance taking place inside the battery. To solve the governing equations of the electrochemical-thermal models, existing numerical methods are time-consuming and computationally expensive. In this study, a novel numerical method was proposed to accelerate the solution of the electrochemical-thermal model for a Li-ion battery. The method was implemented in four steps. In the first step, a physical analogy of the electrochemical process to an electric circuit was used to solve charge conservation equations. In the second and third steps, a control-volume method was used to solve species conservation equations. The simulation results show that the proposed method

was 2.2 times faster than the existing standard methods while maintaining high accuracy, verified by both simulation and experimental data.

In EV applications, the Li-ion battery pack consisting of multiple cells in series and parallel must meet the high demands of current, voltage, power and energy. The temperatures of each cell in the pack are monitored to prevent them from gradually rising to the maximum allowable value which accelerate the degradation rate and leads to thermal runaway. Hence, it is necessary to fully understand the thermal characteristics of Li-ion battery packs under EV driving cycles and ensure the cell temperature in the pack is effectively controlled below the maximum allowable value. In this study, a theoretical electrochemical- thermal model combined with a thermal resistive network was proposed to investigate thermal behaviours of a battery pack. The combined model was used to study heat generation and heat dissipation as well as their influences on the temperatures of the battery pack with and without a fan under constant current discharge and variable current discharge based on EV driving cycles.

The poor performance of Li-ion batteries at low temperatures poses a technical barrier for EV applications. A theoretical electrochemical-thermal model was also proposed to evaluate performance of a Li-ion cell and a Li-ion battery pack at low temperatures. The purpose-designed Li-ion pouch cells were made in the laboratory with known internal parameters and a battery pack was built from four pouch cells connected in series. The proposed model was validated on both the cell and pack over a wide range of temperatures from -10 to 20 degrees at various constant discharge currents and discharge profiles based on EV driving cycles. It was found that the terminal voltages of the cell and pack calculated from the proposed model agree well with those obtained from the experiments. A simulation was also carried out in the validated model to provide insights into cell and pack performance. The study reveals that at the low temperature of -10 degrees, a high discharge rate can cause low diffusivity of the salt in electrolyte and lithium ion in graphite particles and hence in high Ohmic surface and concentration resistances, leading to the poor performance (low available capacity) of the Li-ion cell and Li-ion battery pack, particularly under current profiles of EV driving cycles with high power demand.

Acknowledgement

First of all, I would like to express my deepest gratitude to my principal supervisor Associate Professor Weixiang Shen for his continuous support, valuable guidance and encouragements throughout my research work. I would like to also thank my second supervisor, Dr. Daobin Mu, for his valuable inputs especially on experimental studies. Initial support of my third supervisor, Professor Ajay Kapoor is also highly appreciated.

Thanks to Swinburne University of Technology for giving me the opportunity to undertake my PHD degree, and for the services provided to students, which have been extremely valuable to make this journey to the end. I would also like to thank all of my colleagues at Swinburne for their support and discussion at times during my research. The financial contribution by Swinburne University of Technology through SUPRA scholarship to support my PhD is highly acknowledged.

I wish to express my eternal gratitude to my parents, who sacrificed their life and their youth for me and for encouraging me to follow my dreams. I would like to deeply thank my brother, who always stands on my side, for being my most important confidants, and for being for me whenever I need, for listening to me, advising me, and making me laugh.

Thanks to my husband, Sahel, for being next to me every day with his energy and his patience. Thanks for believing in me and helping me to be strong in hard times. Thanks for accompanying me through every choice, success and difficulty and being my strongest supporter. Last but not least, thanks to my two kids, Liam and Hannah, for the time I was not with them during my research, for accepting me as a tired mom, and disregarding all the motherhood failures I did to them both.

Declaration

This thesis contains no material which has been accepted for the award of any other degree or diploma at any university and to the best of my knowledge and belief contains no materials previously published or written by another person or persons except where reference is made. I understand that my thesis may be available to others electronically.

Part of this thesis have been copyedited and proofread by Dr Gershon Maller (Literati: Academic & Literary Editors), whose services are consistent with those outlined in Section D of the Australian Standards for Editing Practice (ASEP).

Parisa Amiribavandpour

July 2016

Table of Contents

List of Figures:

List of Tables

Chapter 1 Introduction

1-1 Background and motivation

Electric vehicles (EVs) have been in existence ever since the inception of the automobile [1]. However, in the early race for dominance, the internal combustion engine (ICE) quickly overtook EVs as the prime propulsion power system for road vehicles. Although the electric powertrain was superior in terms of performance and energy conversion efficiency, the restrictive factor remained the source of electrical energy. Battery powered vehicles simply cannot match the high energy density, abundant supply and logistical attributes of petroleum based propulsion [2]. Even with ICE energy conversion efficiency figures below 20%, the energy density (Joules/kg) of petroleum far surpasses the energy density of any known battery technology. While economically recoverable petroleum deposits continue to diminish, the automobile population is ever increasing, causing cities to become congested with toxic hydrocarbon by-products. As a result, the ICE is increasingly becoming a target of environmental debate.

Assuming that personal transportation continues to be a vital link in the economic chain of modern societies, the private automobile appears to be the system of choice. This provides opportunities to rethink private transportation modes. At present, after more than a century since its introduction and decades since they were forced into near oblivion, EVs have regained a strong global presence [3, 4]. Industry efforts, coupled with paradigm shifts in transportation perspectives provide substantial grounds for continuing EV research. There are many reasons to seek more clean energy options to replace ICE vehicles. EVs are propelled by an electric motor using electrical energy stored in batteries, with the advantages of high energy efficiency, low air pollution, less dependence on foreign oil, reduced driving noise and smooth acceleration. Increases in gasoline price and greenhouse gas emissions have spurred the growth of EVs. Examples are the Nissan Leaf and Tesla Model S.

Table 1-1: Comparison of specific power and energy of batteries [5, 6]

	Lead Acid	NiMH	Li-ion
Energy Density(Wh/kg)	30-50	60-120	110-160
Cycle Life (to 80% of initial capacity)	200 to 300	300 to 500	500 to 1000
Cell Voltage(nominal)	$2V$	$1.25V$	$3.6V$
Operating Temperature (discharge only)	-10 to 50$^\circ C$	-20 to 60$^\circ C$	-30 to 60$^\circ C$
Maintenance Requirement	3 to 6 months	60 to 90 days	not required
Cost per Cycle (US\$)[11]	\$0.10	\$0.12	\$0.10

Applying batteries in EVs is already commercialised. In order to find the perfect battery for EV applications, different aspects should be reviewed. Table 1-1 compares the main factors of NiMH, Lead-acid and Lithium-ion (Li-ion) batteries. It can be found that although NiMH batteries are capable of delivering high discharge currents, repeated discharge with high load currents reduces the battery's cycle life. Also, NiMH batteries have limited service life if repeatedly deep cycled especially at high load currents. Lead-acid batteries are inexpensive and simple to manufacture, but they have low energy density and the danger of thermal runaway in high temperatures.

On the other hand, the objectives of EVs by 2020 (Table 1-2) should be considered when choosing batteries for EVs. Li-ion batteries almost meet the main required criteria for EVs and make them a perfect candidate for EV applications.

During the past two decades, the energy density and life span of Li-ion batteries have experienced a significant increase. Table 1-3 demonstrates the details of some popular EVs, their battery-pack manufacturer, usable capacity, and price at the calendar year 2015. In the meantime, the cost of Li-ion batteries keeps decreasing. Some of the required characteristics for EVs are already achieved by Li-ion batteries and the rest are being currently researched. Li-ion batteries are used in a variety of portable electronics and hand-held devices, and owing the primary energy source for EVs.

Table 1-2: EV battery objectives by 2020 by the United States Advanced Battery Consortium [7]

	System level	Cell level
Energy Density at C/3 discharge rate (Wh/kg)	500	750
Cycle Life (to 80% of initial capacity)	1000	1000
Cell Voltage (nominal)	380V	N/A
Operating Temperature (discharge only)	-40 to 66^oC	-40 to 66°C
Maintenance Requirement	not required	not required
Cost per Cycle (US$)[11]	$0.08	$0.06

Despite the rapid growth of Li-ion applications in the EV market, its market share in the automotive industry is still limited. In addition to high battery cost, Li-ion batteries suffer from poor performance in different conditions. Li-ion batteries are highly temperature dependent and temperature affects several aspects of the batteries in the operation of EVs: charge acceptance, power and energy capability, reliability, safety issues like thermal runaway, and life and life-cycle costs. It is thus timely to explore the Li-ion battery cell, battery-pack performance and safety using computer modelling to understand their performance in EVs in different conditions.

To understand the fundamental principles of Li-ion batteries and battery packs and determine their suitability for a particular application, numerical simulation is proposed to predict battery behaviours and internal physical limitations [8-16] rather than experiments, which are costly and time-consuming. Comprehensive modelling of Li-ion batteries and battery packs, which are highly dependent on temperature, are required to predict battery-pack behaviour under different EV-driving cycles. In addition, poor performance of Li-ion batteries at low temperatures is also a significant barrier to commercialization of EVs. Li-ion batteries need to handle bursts of power during quick acceleration (high rate discharge) and regenerative braking (high rate charge). For plug-in hybrid electric vehicles (HEVs), batteries are required to function under unassisted operation, charge at -30°C, and survive at -46°C [7]. For power assisted HEVs, batteries should be able to deliver 5kW cold-cranking power (three 2-s pulses, 10-s rests between) at -30°C. Research on low-temperature performance of Li-ion batteries should be conducted to meet these stringent goals.

Table 1-3: Details of selected EVs with Li-ion batteries as energy storage in 2015

Car	Battery-pack manufacturer	Usable capacity (*kWh*)	Price ($)
Tesla model S[17]	Panasonic	40	91,400
Nissan Leaf[18]	NEC	24	39,900
BMW i3[19]	A123 system	22	42,275
Renault Zoe[20]	LG-Chem	22	20,350
Chevy Spark EV[21]	LG-Chem	19	25,995
VW e-Golf[22]	Panasonic/Volkswagen	24.2	30,000
Kia Soul EV[23]	SK innovation	27	33,700
Ford Focus Electric[24]	LG-Chem	23	29,950
Fiat 500e[25]	Bosch/Samsung	24	31,800

In this chapter, the operating principles of the Li-ion battery are briefly introduced. The relevant literature in the areas of fundamental numerical modelling of the Li-ion battery cell and battery packs, and the poor performance of Li-ion batteries at low temperatures are also reviewed.

1-2 Basic principle of the Li-ion battery

A basic Li-ion battery consists of a negative electrode and positive electrode (or anode and cathode, respectively), which are separated by a separator as shown in Figure 1-1. The electrolyte acts as an electronic insulator, but also functions as a good ionic conductor that provides a transport-medium for Li-ions to travel from one electrode to another while keeping the electrons in the external circuit.

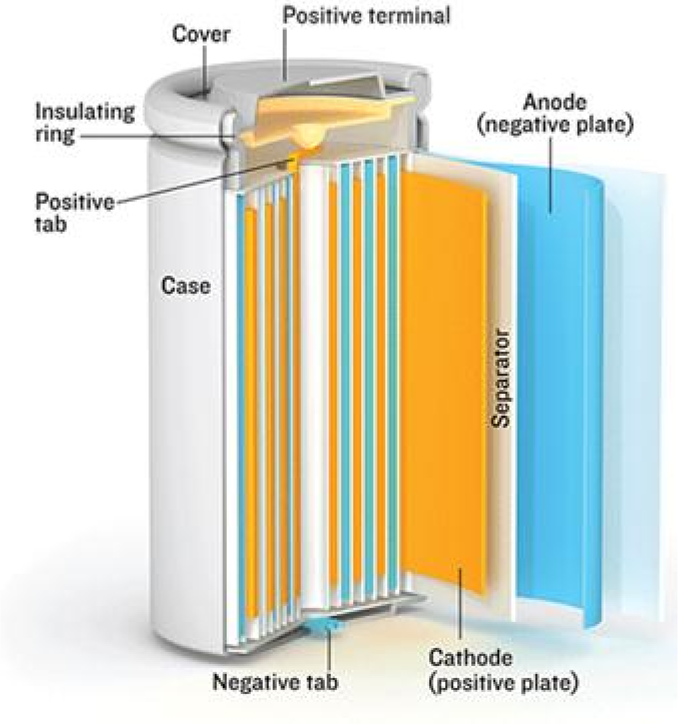

Figure 1-1: Internal regions of a Li-ion cell

Take a cell with a graphite anode and a $LiFePO_4$ cathode for example. During the charge process, Li-ions de-insert from $Li_{1-x}FePO_4$ solid particles and travel through the electrolyte solution to intercalate[1] into Li_xC_6 [6]. Electrons are forced to follow an opposite path through an external circuit. During the discharge process, Li-ions and electrons then travel in reverse. These kinds of batteries are thus called Li-ion (rechargeable) batteries with Li-ions shuttling between the cathode and the anode hosts during the charge and discharge processes that can be described by the electrode reactions. Electrochemical reactions occurring at the electrode/electrolyte interfaces are as follows:

- negative electrode reaction:

$$Li_xC_6 \underset{\rightarrow}{\overset{\leftarrow}{}} C_6 + xLi^+ + ze^-$$

- positive electrode reaction:

---

[1] In Chemistry, intercalation is used to describe the process of inserting a guest atom or ion into a planar crystalline host without losing the structural integrity of the host-like graphite. Any other Li storage process without significant layered structure is considered as insertion.

$$Li_{1-x}FePO_4 + xLi^+ + ze^- \leftrightarrows LiFePO_4$$

- net reaction

$$Li_{1-x}FePO_4 + Li_xC_6 \leftrightarrows LiFePO_4 + C_6$$

Here, the two way reaction refers to the battery discharge (right arrow) and the battery charge (left arrow).

Carbon (such as graphite and coke) being light weight and having a low electrode potential of less than 1 V versus Li/Li+ has become an attractive anode material. It has a theoretical capacity of 372*Ah/kg*, which corresponds to an insertion of one lithium per 6 carbon atoms (x = 1 in Li_xC_6). On the cathode side, $LiFePO_4$, $LiCoO_2$, $LiNiO_2$ and $LiMn_2O_4$ oxides, having a high electrode potential of 4*V* versus Li/Li+, have become the materials of choice for cathode in the present generation of Li-ion cells [26].

Besides the electrode materials, the electrolyte is also important in designing a good Li-ion battery that can offer high performance with long cycle life. The working voltage for Li-ion cells (in the range of 2.5-4.5 *V*) requires an electrolyte having a wide electrochemical stability window. Only a few non-aqueous alternatives (including solid, liquid, and polymeric electrolytes) are among other choices and liquid electrolytes are most commonly exploited to date because of their superior ionic conductivity at ambient temperatures [27].

Commonly used electrolytes in Li-ion batteries are solvent mixtures of alkyl carbonates together with a lithium salt. Solvents used include Ethylene carbonate (EC) [28], dimethy carbonate (DMC) [29], diethyl carbonate (DEC) [30], ethylmethyl carbonate (EMC) [31] and methyl propylene carbonate (MPC) [32]. EC is the preferred solvent, but is solid at room temperature; therefore, EC is often mixed with other solvents such as DMC and EMC to obtain a working electrolyte over a wider temperature interval.

Lithium hexafluorophosphate ($LiPF_6$) is the most commonly used salt in research studies and commercial cells. It has good anodic stability and high ionic conductivities in alky-carbonate solutions. It shows excellent cycling properties at room temperature, but poor cycling behaviour for some electrode materials at elevated temperature. A pronounced disadvantage of $LiPF_6$ solutions is that when $LiPF_6$ decomposes into LiF, high resistive LiF surface films form on the electrode, increasing the electrode's impedance [33].

Finding a replacement for the currently used alkyl-carbonate solvents ($LiPF_6$) is difficult and it is much easier to use functional additives that improve electrode interfaces and enhance conductivity. Alkyl nitrates, sulfates and phosphonates were suggested as passivation-improving additives whose presence reduces the irreversible capacity of Li-C anodes [6].

1-3 Modelling studies of Li-ion batteries

In tandem with experimental studies, electrochemical models were developed to understand cell behaviours. Due to the limitation of experimental characterization techniques, especially during high charge or discharge rates or low and high temperature operation, electrochemical models are of great help in understanding the fundamental mechanisms that dictate cell behaviours.

To understand the fundamental principles of Li-ion batteries and determine their suitability for a particular application, electrochemical models of batteries are proposed to predict battery behaviours and internal physical limitations [8-15] rather than experiments. The electrochemical models are generally more accurate than empirical models, such as equivalent circuit models (ECMs) [34] and others, such as black-box neural network models [35-37], as these only simulate battery behaviours from the input-output point of view while neglecting the mass-transfer balance taking place within batteries.

The electrochemical models can provide a detailed physical field information inside the cell, including concentration distributions, reversible and irreversible heat generations, and heat dissipations. This internal information is difficult to obtain through in-situ observations. By using electrochemical models, engineers are able to find rate-limiting mechanisms and performance controls in EV applications.

Electrochemical models are effective in aiding cell design—a critical process for battery manufacturers. The capacity of 18650 cells has been increased from 1.2Ah to above 2.4Ah with active electrode materials remaining nearly the same ($LiCoO_2$ and graphite). The gain in capacity is mainly attributed to optimization in cell design. Cell design seeks an optimal set of parameters (electrode thickness, porosity, capacity ratio, etc.) with the goal of achieving the highest performance under a specific operational condition. As a result, batteries are usually designed to suit to different levels of power applications (e.g. automotive applications). While the optimization concept is intuitively well known, a great number of experiments are needed to generate an optimum solution, which is an expensive task in terms of time. Mathematical models are able to perform this task in a rapid and cost-effective manner.

In 1990s, Newman and his co-workers developed a macro-homogeneous electrochemical model for the Li-ion battery based on porous electrodes and concentrated solution theories [11, 12], followed by various experimental validations [8, 38]. This model is widely used in subsequent literature. Based on a volume-averaged micro-macroscopic modelling approach, in 2000, Gu and Wang [39] proposed an electrochemical-thermal (ECT) fully coupled framework able to simultaneously predict battery electrochemical and thermal behaviours. Song and Evans [40] also attempted the modelling of lithium polymer batteries by solving electrochemical and thermal equations simultaneously, although only electrolyte conductivity and salt diffusivity were considered as functions of temperature. In 2003, Srinivasan and Wang [41] incorporated all relevant kinetic and transport properties as dependences on temperature, as well as the state of charge (SOC) dependence of entropic heat. In 2008, Kumaresan et al. [42] updated the temperature and concentration dependence of electrolyte properties obtained from recent experimental data. However, the model was validated only at low discharge rates (no larger than 1C) from 15°C to 45°C, where electrochemical-thermal coupling is insignificant.

In the past decade, while multi-dimension modelling was scarce [43, 44] several studies have modelled thermal effects in one dimension by including the energy balance equation and temperature-dependent material properties [41, 42, 45, 46]. Only most recently, multi-dimensional modelling of Li-ion batteries revived its attention due to the huge interest in large-format batteries for electric and hybrid vehicles. Both Gerver and Meyers [47] and Kim et al. [48] attempted multi-dimensional modelling of large-format cells under simplifying assumptions in order to render the computational task manageable. Gerver and Meyers [47] modelled current distribution in current-collecting foils through a network of empirically determined resistors. Kim et al. [48] employed a state-variable model (consisting of algebraic equations) to model electrochemical and transport processes occurring across the thickness of a cell by assuming linear electrolyte transport and also updates of cell temperature. Both simplified models have severe limitations in dynamic operating conditions of vehicle batteries.

Heat conduction in cylindrical cells has been studied in various simplified geometry models: lumped thermal mass[49], 1-D radial direction [50, 51], 2-D spiral geometry [52-54], 1-D radial spiral modelling with the domain reduced from a 2-D spiral model through the coordinate-transform technique [55], 2-D concentric rings [56], and 3-D concentric rings [57]. On the other hand, several studies only solve electrical current along cylindrical metal current collectors assuming uniform kinetics over a cell volume without temperature calculation [58].

1-4 Numerical method studies for Li-ion battery simulation

In order to study Li-ion battery behaviours, numerical methods are used to solve governing equations. The numerical methods are required as electrochemical battery models cannot be solved analytically. The mathematical method used to solve the equations of battery system can also have a significant impact on the computational cost. Including additional physical phenomena in a model increases the computational cost in terms of both solution time and memory. As mentioned in the previous section, several modelling approaches for Li-ion batteries exist, there is a trade-off between accuracy and computational cost. An ideal model would be perfectly predictive under all operating conditions for the entire life of the battery with minimal computational requirements. However, such a model does not exist for battery models due to the many coupled and nonlinear physical phenomena in battery systems. To reduce the computational time, some simplifications can be done on electrochemical model based on their applications. Considering model simplifications, electrochemical models can be generally classified into two groups:

Single Particle Model.—The single-particle model (SPM) is a simple model that represents each electrode as a single particle [59] and considers diffusion in the solid phase. But, it neglects solution phase effects [60-62]. The SPM battery models are typically solved by discretization of the spatial derivatives. Hence, equations become a set of first-order differential algebraic equations (DAEs) [63, 64] that can be solved using optimized solvers for initial value problems.

DAEs can be difficult to solve because the initial conditions must be consistent with the algebraic equations, which causes many solvers to fail if inconsistent conditions are provided, especially when nonlinear algebraic equations are considered [65, 66].

The SPM has been used to predict capacity fade due to the growth of the SEI layer[59], which makes the SPM a good choice as an initial attempt for implementation in a microcontroller. The SPM has been validated for rates up to a 1C discharge rate. At higher rates of discharge, the electrolyte characteristics become important and cannot be neglected. Hence, this SPM model cannot be used for the discharge rates higher than 1C [60, 61, 67].

The SPM can be further reduced if a parabolic profile approximation in the solid phase is considered [68]. After reduction, it can only track the average and surface lithium concentration in the solid phase by solving the minimum number of DAEs, e.g. 4 DAEs, which makes the SPM very efficient for use in simulations for low current rate (or power) applications. However, for applications in which high current rates are experienced, a more comprehensive model is needed to accurately estimate the internal states to develop aggressive control strategies.

Electrochemical engineering models—The pseudo-two-dimensional model, mentioned in the previous section, is a more detailed physics-based model that considers the electrochemical potentials within the solid phase and electrolyte along with lithium concentration in both the solid- and liquid-phases [11], and is flexible to include additional physical phenomena [8, 12, 38, 54, 61, 69-72]. The improved predictive capability of this model has contributed to its popularity among battery researchers. It has two independent spatial variables: x to track the variables across the thickness of the cell sandwich and r to track the lithium concentration radially in the solid electrode particles [11]. Multiple spatial variables increase the dimensionality of the problem, which greatly increases the number of equations to be solved and computational cost if a finite difference approach is used to discretize both x and r directions. If 15 node points are used in the radial direction, 50 node points across each electrode, and 25 node points for the separator, nearly 2000 DAEs must be solved. With such a large number of DAEs, appropriate mathematical techniques are required to reduce computational time which allows the model to be implemented in EV applications [66]. This motivates researchers to develop mathematical techniques to simplify the battery models and enable faster simulation. For example, proper orthogonal decomposition has been used to reduce the total number of states simulated in [73]. Quasi-linearization combined with a Pade approximation has also been used to simplify the model and simplify simulation [74].

Many commercial software packages, such as COMSOL and Fluent, use well-understood numerical methods to solve ordinary differential equations (ODEs) or partial differential equations (PDEs). However, many nodes, control volumes, or elements are required for convergence, which makes these software packages computationally expensive.

Even for linear problems, it is difficult to implement into an EV application. Furthermore, many commercial solvers are over-designed in order to handle a wide variety of problems with minimal input from the user. They do not exploit the structure and unique characteristics of the underlying models, which can be used to improve the computational performance without compromising on the robustness.

In order to reduce the number of DAEs that must be solved for the electrochemical-thermal model, the reformulation methods described previously for the SPM can be implemented for the solid phase diffusion in the electrochemical-thermal model. Using the parabolic profile approximation for the concentration profile can significantly reduce the number of DAEs, thereby improving computational efficiency [63]. For the case with 50 nodes across each electrode and 25 nodes for the separator, roughly 500 DAEs must be solved, much less than the 2000 for a full finite difference approach. The parabolic profile approximation is valid for long times and low rates, but has inaccuracies when there is a large gradient in the solid phase particles, which become significant for rates greater than 4C and high variable discharge rates [63].

Reformulation in x-direction can also be applied to further reduce the computational demands of simulation. To solve the reformulated equations, spectral methods are used to find the solution which have faster convergence comparing to the finite difference methods. The disadvantage of the reformulation is that the method implantation is not easy and the resulting set of equations is not sparse, unlike for the finite difference method.

In spectral methods, the unknowns are approximated as a series solution of trial functions, such as cosines, with time-dependent coefficients. The coefficients are determined by minimizing the residual of the governing equations across the domain typically by using the Galerkin or orthogonal collocation (OC) methods [66], though OC can better handle non-linear parameters, the integration required for the Galerkin approach is computationally prohibitive. Since each dependent variable is approximated as a series solution, it may be possible to solve some equations analytically. Symbolic math tools such as Maple or Mathematica can play an important role in solving unknown variables to reduce the number of equations that the solver must compute. This can increase the complexity of the remaining equations, testing is often required to determine if this approach is indeed advantageous."

1-5 Modelling studies of the Li-ion battery pack

In EV applications, a Li-ion battery pack consisting of multiple cells in series and parallel is required to meet high demands of current, voltage, and energy. The temperature of each cell in the pack is monitored to prevent it from gradually rising to the maximum allowable value, leading to the acceleration of the degradation rate and thermal runaway [75]. Hence, it is necessary to fully understand the thermal characteristics of Li-ion battery packs under EV-driving cycles and ensure cell temperature in the pack is effectively controlled below the maximum allowable value.

Numerical modelling and simulation is a better way to improve the fundamental understanding of thermal behaviour of battery packs compared with costly and time-consuming experimental tests. Thus, in this study, numerical modelling and simulation was used to study thermal phenomena of battery packs in constant current discharge and EV driving-cycles based variable currents—crucial for properly designing the EV thermal management system.

The precise temperature prediction of battery packs strongly relies on heat-generation and dissipation rates. According to the differences in the calculation methods of heat-generation and dissipation rates, existing thermal models can be classified into empirical, semi-empirical, and theoretical-thermal models.

In empirical-thermal models, the heat-generation rate is calculated by Joule's law with internal resistances determined by fitting the experimental data at different temperatures [76] or measuring the temperature evolution of the battery [77]. The heat-dissipation rate is found by using the experimental results of measured temperature at different discharge rates and the temperature relaxation curve [39, 78]. The determined heat-dissipation rate accounts for the effect of heat conduction and convection. Since reliable predictions of heat-generation and dissipation rates rely on experimental data, the application of this empirical-thermal model is limited to a few specific battery packs.

In semi-empirical thermal models, the heat-generation rate is calculated on the general energy balance equation [79], which is derived from the electrochemical reaction and charge-transfer processes inside the Li-ion battery. The parameters in the general energy balance equation are determined from experimental data [57, 80]. For the calculation of the heat-dissipation rate, it is assumed that heat transfer was a function of the location and the surrounding temperature of the battery, where the required functional parameters are determined by experiment [81]. The semi-empirical thermal model has wide application scope for battery packs compared with empirical-thermal models, but model accuracy needs to be improved because the spatial variation of the parameters in the electrodes (such as reaction current density, active material concentration etc.) were neglected, which leads to significant errors in heat-generation estimates [82].

In theoretical-thermal models, the heat-generation rate is determined from the porous electrode theory, electrode-reaction mechanisms, and concentration solution theory [83]. The heat-dissipation rate is calculated based on boundary-layer theory to specify the convective heat coefficient in the battery pack [84]. Considering the fact that the theoretical-thermal model assumes the universal electrode reaction and the spatial variation of electrode parameters in the heat-generation rate calculation as well the application of boundary-layer theory [85] in the heat-dissipation rate calculation, this thermal model can be used for varieties of battery packs with high accuracy compared to the other thermal models. less, the current theoretical-thermal model neglects both reversible heat, which contributes to a significant proportion of heat generation, and conduction-heat transfer, which plays an important role in heat dissipation in battery packs for EV applications.

1-6 Studies of Li-ion batteries at low temperatures

The energy and power capability of Li-ion batteries reduces significantly at low temperatures. It has been reported that 1.4*Ah* Panasonic 18650 cells retained only 5% of energy density and 1.25% of power density at -40°*C* as compared to their 25°*C* values [86]. Significant research has been undertaken to understand and improve the low-temperature performance of Li-ion batteries. However, the main performance-limiting mechanisms remain contentious.

1-6-1 Electrolyte

The electrolyte solution is considered the main limitation by many researchers. The ionic conductivity of 1*M* solution of $LiPF_6$ in 1:1 EC-DMC reduces from 18*mS/cm* at 25°*C* to 3*mS/cm* at -20°*C* [87]. The solution even freezes at about -30°*C*. It is expected that Li-ion cells using this electrolyte will have a significant performance drop at -20°*C* and die at -30°*C*. Investigations currently seek electrolyte solutions with a lower freezing point and higher conductivity. Due to the high freezing points of widely used carbonate-based solvents, such as Ethylene carbonate (EC) and dimethyl carbonate (DMC), binary, ternary, and quaternary electrolytes were used to reduce freezing points. Smart et al. [88] found that the ternary, equi-proportion formula of EC, DMC, and DEC, displayed higher ionic conductivity, faster Li intercalation kinetics, and better surface-film characteristics than the binary analogues, especially at low temperatures (-20°*C*). Ethylmethyl carbonate (EMC) was found to be a useful co-solvent because of its low freezing point (-55°*C*) [89]. Plichta and Behl proposed the use of a 1:1:1 EC-DMC-EMC mixture for the electrolyte. Li-ion cells using it were found to deliver most capacity at -20°*C* at 1/20C rate. Quaternary formulas were also investigated. Using 1*M* $LiPF_6$ in the quaternary mixture of EC, DEC, DMC, and EMC (1:1:1:3), prototype 9*Ah* cells were able to deliver 76% of their room temperature capacity at -40°*C* with C/10 rate [90].

Co-solvents are also incorporated into multicomponent electrolyte formulations for enhanced performance at low temperatures. Solvents that possess very low freezing points and viscosities, such as esters, are very effective in improving ionic conductivity of the carbonate electrolyte. Shiao et al. [91] found that the use of methyl acetate (MA) in an EC:EMC mixture significantly improved cell capacity below -20$°C$. Cells using an EC:EMC:MA:toluene solvent were able to deliver 50% nominal capacity at -40$°C$ with C/10 rate. Herreyre et al. [92] tested the use of ethyl acetate (EA) and methyl butyrate (MB) as co-solvents in EC/PC and linear carbonate in 5.5Ah Gr-LCO cells. EA and MB enabled very good performance (90% nominal capacity) down to -40$°C$, even under C/2 rate. A more comprehensive study was given by Smart et al. [93].

A number of ester co-solvents, including MP (methyl propionate), EP (ethyl propionate), MB, EB (ethyl butyrate), PB (propyl butyrate), BB (butyl butyrate), in EC and EMC mixtures were investigated. Prototype 7Ah cells containing the electrolyte with co-solvents were capable of delivering over six times the amount of capacity than those with call-carbonate blend electrolyte, and supported moderate rates down to -60$°C$. Smart et al. [94] studied more electrolyte additives, including mono-fluoroethylene carbonate (FEC), lithium oxalate, vinylene carbonate (VC), and lithium bis (oxalato borate) (LiBOB). The cell using any of these electrolyte additives demonstrated more than double discharge capacities compared with the cell without additives. The additives helped to form favourable film characteristics, leading to faster charge transfer kinetics. With the use of solvent blends, co-solvent, novel electrolyte salts, and electrolyte additives, the Li-ion cells survived and even showed good performance down to -60$°C$ [87, 88, 91, 93, 95, 96].

1-6-2 Surface film

Besides the ionic conductivity, the nature of films formed on the surface of active materials is also strongly related to the electrolyte. The surface film affects the performance of Li-ion cells because it changes the interfacial kinetics and Li-ion transport through the film. It also dictates the life of the cell because it protects active materials from side reactions.

Electrolyte solutions able to form surface film with lower resistance, higher stability, and faster kinetics of lithium intercalation and deintercalation are preferred. Smart et al. [95] found that the electrolyte composition affected the stabilities of surface film. Low molecular weight co-solvents made the film resistive and inadequately protective, whereas high molecular weight esters resulted in surface films with more desirable attributes. One example is using EA or EB as co-solvents. Despite lower conductivity, an electrolyte using EB was able to deliver five times more capacity at -20°C, compared with the use of EA [95].

Zhang et al. [96] also found that adding PC into an EC:EMC mixture improved the discharge capacity below -20°C in spite of a slight decrease in ionic conductivity. The increased low-temperature performances were attributed to improved characteristics of the surface film. Wang et al. [97] employed GITT and electrochemical impedance spectroscopy (EIS) to study Li graphite coin-cell behaviour at -30°C. The performance-limiting mechanism was found to be the resistance of solid electrolyte interphase film, which increased by a factor of over 27 from 25°C to 30°C. In contrast, the resistivity of the electrolyte showed only a 10-fold increase. Fan [98] studied the discharge behaviour of commercial 18650 graphite-$LiCoO_2$ (LCO) cells down to -40°C. When the temperature dropped from room temperature to -30C, cell impedance at 1 kHz changed minimally. However, dc impedance was increased by a factor of ten. He concluded that the ionic conductivity of the electrolyte did not limit cell-discharge capability, while the lithium diffusion in the cathode surface film could be the limiting factor.

1-6-3 Charge transfer kinetics

Charge transfer kinetics in Li-ion cells is an interfacial phenomenon at the solid particle electrolyte interface, including Li+ solvation/desolvation, Li^+ transport through surface films, the release/acceptance of an electron from the external circuit, and lithium leaving/inserting into the active materials. Slow reactions generate large overpotential, leading to reduced cell voltage. Although the charge-transfer process is closely associated with other transport processes, these processes are staying at different time scales. Therefore, it is possible to separate them by using EIS, where small voltage permutations (<10mV) are applied to the cell and complex impedance is calculated from the current response. The resistance associated with charge-transfer Rk can be obtained from the diameter of the lower frequency semi-circle in the Nyquist plot.

Suresh et al. [99] analysed the impedance of Samsung 0.9Ah Gr-LCO cells from -10°C to 40°C using EIS. The high-frequency resistance was invariant, and kinetic resistance showed the strongest dependence on temperature. He concluded that the poor discharge capacity of Li-ion cells at low temperature was due to the very low values of exchange current. Zhang et al.

[100, 101] found that replacing LiPF6 with LiBF4 salt in PC-EC-EMC mixed solvent increased the discharge capacity from 72% to 86% at -30°*C*. Although the LiBF4 based electrolyte had lower ionic conductivity than the LiPF6 analogue, it achieved improved performance due to reduced charge-transfer resistance.

In addition, Zhang et al. [102] performed EIS analysis on various kinds of Li-ion cells, including coin-size full cells, coin-size symmetric cells, and 18650 Gr-LCO 2.4*Ah* cells [103]. The cell resistance was separated into bulk resistance, film resistance, and charge-transfer resistance. It was found that the charge-transfer resistance increased most significantly as the temperature decreased. At room temperature, bulk resistance occupied half the cell resistance. However, at low temperature (-20°*C*), charge-transfer resistance dominated. Jansen et al. [104] surprisingly found that the impedance rise at low temperature was not significantly impacted by the choice of active material. Because the main rise in impedance occurred in the mid-frequency range, the responsible phenomenon was most likely a charge-transfer process at the electrolyte interface. Abraham et al. [105] performed an impedance analysis on film-free active materials (LTO), binder-free electrodes, and conducting carbon-free electrodes. The charge-transfer processes, whose impedance dwarfed ohmic resistance and diffusional resistance, were observed to have the same activation energies regardless of the active material, binder, and conducting agent. He suggested that the limiting process was the electrochemical-reaction step at the interface.

1-6-4 Solid-phase diffusion

Solid-phase diffusion depicts lithium transport inside the particles of active materials. Due to limited solid-phase diffusivity, concentration polarizations are expected inside active material particles. Since solid-phase diffusivity decreases with reducing temperature, large solid-phase concentration polarization occurs at sub-zero temperatures. During discharge, the lithium concentration at the anode-particle surface might be depleted, lower cell voltage below cut-off level, and lead to reduced cell capacity.

Huang et al. [106] found that the discharge capacity of the graphite half-cell differed greatly from its charge capacity at -40°*C*, which cannot be explained by electrolyte or surface-film conductivity. It was also found that particle size affected capacity at sub-zero temperatures, which further supported the contention that Li diffusivity limited low-temperature performance. Lin et al. [107] tested 100*mAh* Gr-LCO cell behaviour using a high conductivity electrolyte at -20°C. Large permanent capacity loss was found, which was attributed to the high polarization of the anode due to the limited solid-state diffusion of lithium. Zhang et al. [108] measured solid-phase diffusivity of graphite at different temperatures. A dramatic decrease in diffusivity occurred in the temperature range of 0°C to -20°C, which was responsible for the large capacity drop of the graphite electrode. Sides and Martin [109] investigated the effect of active material particle size on Li-V_2O_5 cell performance. They found that, at -20°C, cell performance always improved with decreasing particle diameter, but sometimes decreased with increasing specific surface area.

Since the particle diameter represented diffusion length, while the latter denoted the reaction area, the result implied the dominance of solid-state diffusion. Allen et al. [110] compared the electrochemical performance of Li/$Li_4Ti_5O_{12}$ (LTO) button cells using LTO with 350nm and 700nm diameter respectively. The cell using the 350nm particle exhibited double capacity at -20°C and -30°C (C/8 rate) compared to the one using 700nm particle, due to the shortened solid-state diffusion length. Liao et al. [111] characterized the low-temperature performance of Li/$LiFePO_4$ (LFP) cells made of quaternary electrolyte. This electrolyte was shown to have excellent performance at low temperatures by Smart et al. [90] Despite the optimized electrolyte solutions, the Li/LFP cell displayed reduced voltage and capacity at sub-zero temperatures. EIS tests demonstrated that increased charge-transfer resistance and decreased Li-ion solid-phase diffusivity were the main performance-limiting aspects. Fan and Tan [112] investigated the charging of Li-ion cells at -20°C. Two peaks were found in the charge and subsequent discharge-voltage profiles.

This phenomenon cannot be explained by increases of charge-transfer or surface-film resistance, which generated smoothly increased cell voltage during charge. The two peaks, however, can be explained by the two minimums in solid-state diffusivity. It was therefore concluded that the lithium solid diffusion in the graphite was the ultimate rate-limiting factor. In summary, the performance-limiting factors of Li-ion cells at sub-zero temperatures are still under debate. Various sources have been reported by different investigators, including poor electrolyte conductivity, sluggish kinetics of charge transfer, increased resistance of particle-surface films, and slow Li diffusion through the surface layers and the bulk of active material particles. Although there is no widely accepted limiting mechanism, all the above factors contributed to poor low-temperature performance.

The theoretical-thermal models based on concentrated solution theory and the technique of volume averaging for porous electrodes was introduced in [8, 11, 12].

Subsequently, electrochemical-thermal fully coupled frameworks able to simultaneously predict battery electrochemical and thermal behaviours were developed [113, 114]. Recently, Ji et al. [115] have applied the electrochemical-thermal model for the 18650 Li-ion and examined the basic nature of cell operation at low temperatures for constant current-discharge rates.

1-7 Scope of the thesis

1-7-1 Major contribution

As discussed, there are still some key features of the Li-ion battery which need improvement for EV applications. In particular, electrochemical-thermal coupled phenomena in Li-ion batteries must be captured as they determine the current major technological hurdles, such as thermal runaway at high temperatures and greatly reduced performance at sub-zero temperatures.

To date, both experimental and modelling research on thermal and electrochemical characteristics are mostly limited to Li-ion cells. For example, early models of Li-ion cells were developed by Newman and co-workers using porous electrode and concentrated solution theories [11, 116] under isothermal and one-dimensional assumptions. Subsequently, Wang and co-workers have focused on electrochemical-thermal coupled modelling for Li-ion batteries [44, 46, 113]. Model validation was performed against experimental data of full cells only. Thus, extensive research is required to deal with the current issues.

Firstly, the governing equations of a Li-ion battery based on the above models are a set of coupled nonlinear partial differential equations (PDEs). To solve the PDEs, iterative methods are implemented that are computationally expensive and highly time-consuming. Stringent automotive application, however, calls for fast and online solutions. The first objective of this thesis is to propose a cost-effective method to solve the PDEs and achieve required parameters with high accuracy.

Secondly, a number of coupled thermal-electrochemical battery models are only introduced at Li-ion cell levels. There is lack of extensive research in this area at the battery-pack level. The second objective of this research is to develop a comprehensive thermal-electrochemical battery model in Li-ion pack levels.

Thirdly, the electrochemical-thermal model of a Li-ion battery is used to examine the basic nature of cell operation at low temperatures under constant current-discharge rates. However, for EV applications, battery-pack performance under EV-driving cycles at sub-zero temperatures are of great interest. The third objective of this study is to explore the basic nature of the Li-ion battery operation at sub-zero temperatures under current profiles based on EV-driving cycles both numerically and experimentally.

1-7-2 Thesis outline

The dissertation proceeds by introducing a general electrochemical-thermal coupled model in Chapter 2. A cost-effective numerical method proposed to solve the electrochemical-thermal coupled model and obtain required parameters with high accuracy is introduced in Chapter 3. This model is then validated with experimental data. To determine Li-ion battery-pack behaviour in EV applications, the electrochemical-thermal coupled model is developed and validated with experimental data for constant current-discharge rates and EV driving cycles in chapter 4. In chapter 5, the validated model is used to investigate the rate-limiting factors of Li-ion cells operating at low temperatures in EV applications. Chapter 6 provides conclusions and future recommendations.

Chapter 2 Electrochemical-thermal model for Li-ion battery cell

2-1 Introduction

Modelling and numerical simulation is a better way to improve the fundamental understanding of Li-ion batteries in EVs compared with the costly and time-consuming experimental tests [8-15]. Furthermore, using the numerical simulation has the added advantage of providing the detailed physical field information inside the battery which is almost impractical to obtain through in-situ observations such as electrochemical characteristics and internal heat generation and dissipation. Hence, the Li-ion battery model will be introduced to study Li-ion battery behaviour in EV application purposes.

Despite vast difference in geometry and capacity (coin cells, cylindrical cells, prismatic cells), all lithium ion cells are composed of five basic layers: negative current collector (Cu foil), negative electrode (anode), separator, positive electrode (cathode) and positive current collector (Al foil). The present study employs 26650 cells, where the sandwich of these layers is rolled up to form a jelly roll, as shown in Figure 2-1. The anode, the cathode and the separator are porous structures, containing large void spaces where electrolyte is filled to provide the media for lithium ion transport.

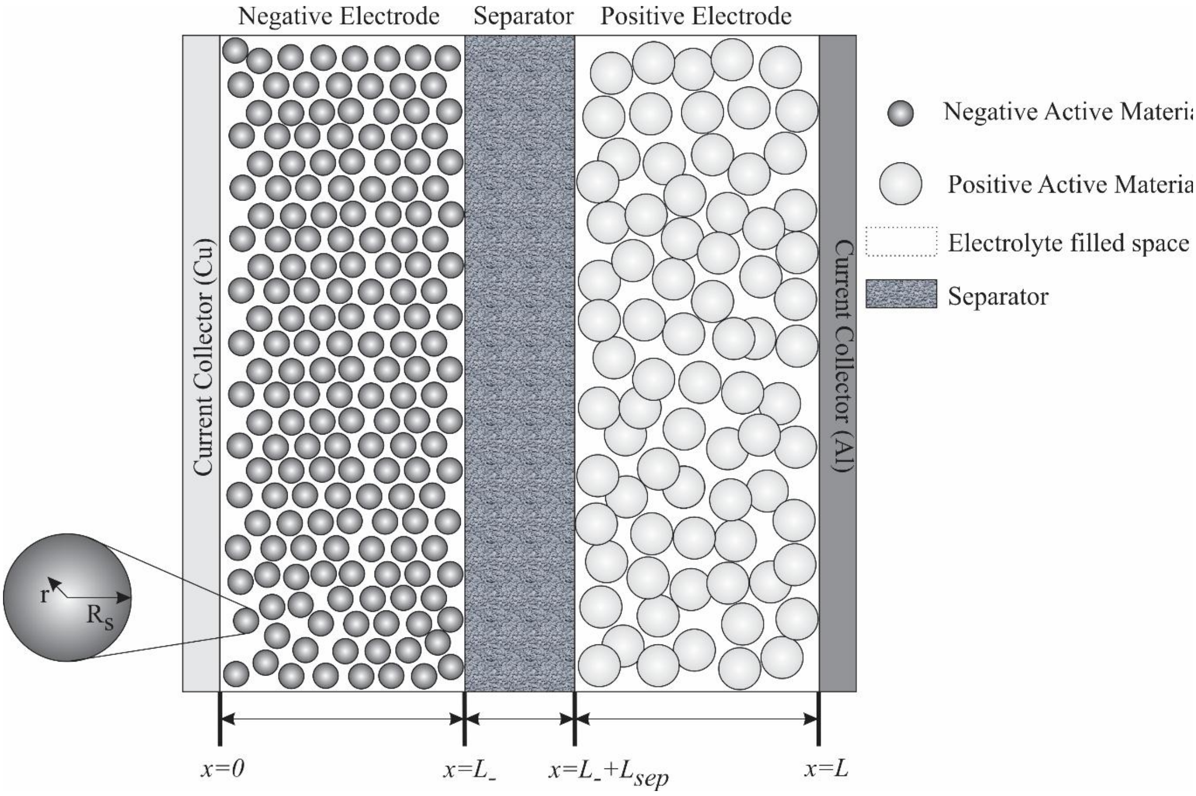

Figure 2-1: Schematic of five basic layers of Li-ion cell

Electron goes out/into the current collectors from external circuit, while lithium ion transfers internally as a shuttle between the anode and the cathode through the electrolyte. Li-ion cell electrodes have three dimensional structures. However, current flow and species transport take place mainly in the thickness direction of the anode, separator and cathode layers, owing to the extremely high electrical conductivity of current collectors. It is a good approximation to employ one dimensional model to simulate Li-ion cell behaviours.

In this chapter, the assumption to develop the Li-ion battery model is outlined. The governing electrochemical equations and also the governing thermal equations are described. Then the coupling equation which makes the electrochemical-thermal coupled Li-ion model is discussed.

2-2 Mathematical model

The main assumptions are made to develop a lithium ion battery model as follows.

- Based on porous electrode theory [116], electrodes are divided into solid phase (active materials) and electrolyte phase. Gas generated during operation is neglected.
- Active materials in solid electrodes are considered to be homogenous and are composed of spherical components.
- The transport process of lithium ions between the electrodes is via diffusion and migration.
- The effect of current collectors on lithium ion transfer is neglected.
- The point at the boundary line between the negative electrode and current collector (Cu) is set to be the origin of x-coordinate.

Porous electrode theory is adopted in modelling the composite electrodes consisting of active material and electrolyte solution. The solid and electrolyte phases are treated as superimposed continua with each phase having its own volume fraction, while the microstructure of each phase is not considered. Therefore, the material balances should be averaged in a volume large enough to treat electrochemical reaction as a homogeneous term but small compared to the overall dimension of the electrode. For tortuosity effect, electrolyte diffusion coefficient and ionic conductivity are corrected using Bruggeman relationships, $D_e^{eff} = D_e \varepsilon_e^{\tau}$ and $\kappa^{eff} = \kappa \varepsilon_e^{\tau}$, respectively, where τ is the Bruggeman exponent. And electronic conductivity is corrected as $\sigma^{eff} = \sigma \varepsilon_e^{\tau}$, for each electrode. Here, ε_e and ε_s are electrolyte and solid phase volume fractions, respectively.

The governing equations are divided to three main groups explained as below: (1) charge transport equations, (2) species conservation equations and (3) thermal equations. The list of the symbols used in the governing equations is shown in Table 2-1.

Table 2-1: List of symbols for a lithium ion battery model

Symbol	Name	Unit
i_e	Electrolyte current density	Acm^{-2}
i_s	Solid current density	Acm^{-2}
ϕ_e	Electrolyte potential	V
ϕ_s	Solid potential	V
c_e	Electrolyte concentration	$mol\ cm^{-3}$
c_s	Solid concentration	$mol\ cm^{-3}$
c_{se}	Solid concentration at electrolyte interface	$mol\ cm^{-3}$
j^{Li}	Butler-Volmer current density	Acm^{-3}
U	Open circuit voltage	V
U_n	Anode open circuit voltage	V
U_p	Cathode open circuit voltage	V
η	Overpotential	V
F	Faraday’s number, 96487	$Cmol^{-1}$
$I_{applied}$	Applied battery current	Amp
R	Gas constant, 8.314	$JK^{-1}mol^{-1}$
T	Temperature	K

θ	normalized solid electrolyte concentration ($c_{se}/c_{s\max}$)	-

2-2-1 Charge transport equations

The charge transport equation in solid phase is described by Ohm's law

$$\frac{\partial}{\partial x}(\sigma^{eff}\frac{\partial\phi_s}{\partial x}) = j^{Li} \tag{2-1}$$

with boundary conditions at the current collector proportional to applied current density: $\sigma^{eff}\frac{\partial\phi_s}{\partial x}\Big|_{x=0,L} = \frac{I_{applied}}{A}$ and $\frac{\partial\varphi_s}{\partial x}\Big|_{x=L_-} = \frac{\partial\varphi_s}{\partial x}\Big|_{x=L_-+L_{sep}} = 0$. The positive applied current density indicates charge while the negative applied current density indicates discharge. The transport flux of lithium ion in electrolyte is derived from concentration theory [116]

$$\frac{\partial}{\partial x}(\kappa^{eff}\frac{\partial\phi_e}{\partial x}) + \frac{\partial}{\partial x}(\kappa_D{}^{eff}\frac{\partial}{\partial x}\ln c_e) = -j^{Li} \tag{2- 2}$$

with boundary conditions $\frac{\partial\varphi_e}{\partial x}\Big|_{x=L_-} = \frac{\partial\varphi_e}{\partial x}\Big|_{x=L_-+L_{sep}} = 0$. The transfer current density is described by Butler-Volmer equation at the solid/electrolyte interface

$$j^{Li} = a_s j_0\{\exp(\frac{\alpha_a F}{RT}\eta) - \exp(-\frac{\alpha_c F}{RT}\eta)\} \tag{2- 3}$$

where the overpotential, η is obtained from

$$\eta = \phi_s - \phi_e - U \tag{2- 4}$$

In Eq.(2- 4), U is the open circuit voltage (OCV) which is a function of solid concentration at the electrolyte interface and the potential difference between the positive and negative electrodes. They are expressed in the positive and negative electrode as [117]

$$\begin{aligned} U_p &= 3.4323 - 0.8428\exp(-80.2493(1-\theta)^{1.3198}) - 3.2474\times10^{-6}\exp(20.2645(1-\theta)^{3.8003}) \\ &+ 3.2482\times10^{-6}\exp(20.2646(1-\theta)^{3.7995}) \end{aligned} \tag{2-5}$$

$$U_n = 0.6379 + 0.5416\exp(-305.5309\theta) + 0.044\tanh(-\frac{\theta - 0.1958}{0.1088}) - 0.1978\tanh(\frac{\theta - 1.0571}{0.0854})$$
$$- 0.6875\tanh(\frac{\theta + 0.0117}{0.0529}) - 0.0175\tanh(\frac{\theta - 0.5692}{0.0875}) \quad (2\text{-}6)$$

respectively. The value of θ is the normalized Li concentration at the surface of the electrode

$$\theta = \frac{c_s}{c_{s,\max}} \quad (2\text{-}7)$$

The coefficient i_0 in Eq. (2- 3) exhibits the solid and electrolyte concentration dependency

$$i_0 = (c_e)^{\alpha_a}(c_{s,\max} - c_{se})^{\alpha_a}(c_{se})^{\alpha_c} \quad (2\text{-}8)$$

The terminal voltage across the battery can be determined by

$$V(t) = \phi_s\big|_{x=L} - \phi_s\big|_{x=0} - \frac{R_f}{A}I_{applied} \quad (2\text{-}9)$$

where R_f is the film resistance on the electrode area [10].

2-2-2 Species conservation equations

The centre of the lithium ion sphere is considered as the origin, the conservation of particle in solid phase using Fick's law of diffusion is

$$r^2\frac{\partial c_S}{\partial t} = D_S\frac{\partial}{\partial r}(r^2\frac{\partial c_S}{\partial r}) \quad (2\text{-}10)$$

with boundary conditions $\left.\frac{\partial c_s}{\partial r}\right|_{r=0} = 0$ and $\left.\frac{\partial c_S}{\partial r}\right|_{r=R_S} = -\frac{j^{Li}}{D_S F}$. The model can also simulate cylindrical and planar particles; the treatment is analogous. For an electrode composed of spherical particles of radius R_s, the initial specific surface area is given by

$$a_s = \frac{3\varepsilon_s}{R_s} \quad \textbf{(2-11)}$$

where ε_s is the volume fraction of solid phase. Corresponding formula should be used to calculate this specific surface area if cylindrical or planar particle is assumed. For modelling of irregularly shaped particles however, it is proposed to directly base the micro-macroscopic model on the measured specific surface area because its inverse is a more accurate representation of the length scale of a complex micro-macro structure than the average particle sizes [10].

In general, decreasing the particle size while keeping the porosity results in high surface area which usually gives higher rate capability and higher utilization. However, it should be noted that small particle would make it difficult to bind the particles together and hence may result in greater ohmic drops because of poor contact. In addition, smaller particle size electrodes would increase the use of carbon to coat the particles, resulting in a decrease in the tape density, therefore the decrease of the cell volumetric energy density. These issues indicate that it should be careful to make a recommendation on the optimum particle size. While uniform particle size is adopted in most models, the particle sizes may have a distribution in real electrode. The model study in this paper [118] shows that the performance of an electrode with two-particle distribution is worse than that of the electrode with uniform particle at the average size because the larger particles will give rise to transport limitations.

The conservation of Li ion in electrolyte phase yields

$$\frac{\partial(\varepsilon_e c_e)}{\partial t} = \frac{\partial}{\partial x}(D_e^{eff}\frac{\partial c_e}{\partial x}) + \frac{1-t_+^0}{F} j^{Li} \tag{2-12}$$

with the boundary condition $\left.\frac{\partial c_e}{\partial x}\right|_{x=0,L} = 0$.

2-2-3 Thermal equations

For a multicomponent battery system consisting of porous electrode and electrolyte, the general differential equation of thermal energy balance can be rewritten as

$$\rho_k c_{pk}(\frac{\partial T_k}{\partial t} + v_k.\nabla T_k) = -\nabla.Q_k + \sum_{species} \widehat{H}_k \nabla.J_k \tag{2-13}$$

where v is the velocity vector, J is the molar flux of a species due to diffusion and migration, and $\hat{H}$ is the species partial molar enthalpy, with subscript k denoting in phase k.

The assumptions to develop Eq. (2-13) are: negligible heat effect due to viscous dissipation and no body force, and no homogenous chemical reactions[39]. The second term on the right hand side of Eq. (2-13) represents thermal transport due to species diffusion and migration, with the summation carried out over all species in phase k. In general, the heat flux Q includes conductive flux (or Fourier flux), flux caused by inter-diffusion of various species, and the Dufour energy flux (or diffusion-thermo effect). Because Dufour energy flux is usually negligible [119], the heat flux Q can be expressed as

$$Q_k = -\lambda_k \nabla T_k + \sum_{species} \hat{H}_k J_k \tag{2-14}$$

Applying Eq. (2-14) and the continuity equation for phase k

$$\nabla . v_k = 0 \tag{2-15}$$

Equation (2-13) becomes

$$\rho_k c_{pk} (\frac{\partial T_k}{\partial t} + \nabla.(v_k T_k)) = \nabla.(\lambda_k \nabla T_k) - \sum_{species} J_k . \nabla \hat{H}_k \tag{2-16}$$

Use the thermodynamic relationship [119]

$$\hat{H}_k = \mu_k - T\frac{\partial \mu_k}{\partial T} \tag{2-17}$$

and also the electrochemical potential [119]

$$\mu_k = \mu_k^0 + RTln(\frac{a_k}{a_{k,ref}}) + zF\phi_k \tag{2-18}$$

where μ_0^k and a_k are the standard chemical potential and the activity of a species in phase k, respectively, we have

$$\nabla \hat{H}_k = -R\nabla \left[T^2 \frac{\partial \ln(\frac{a_k}{a_{k,ref}})}{\partial T} \right] + zF\nabla(\phi_k - T\frac{\partial \phi_k}{\partial T}) \tag{2-19}$$

The first term in right hand side of Eq. (2-19) is related to the enthalpy of mixing and has been neglected generally [82, 120, 121]. Also the temperature dependence of phase potential is neglected for simplicity. Then, Eq. (2-19) is simplified to

$$\nabla \widehat{H}_k = zF\nabla \phi_k \tag{2-20}$$

Substituting Eq. (2-20) into Eq. (2-16) yields

$$\rho_k c_{pk}(\frac{\partial T_k}{\partial t} + \nabla.(v_k T_k)) = \nabla.(\lambda_k \nabla T_k) - \sum_{species} zFJ_k.\nabla \phi_k \tag{2-21}$$

The current through phase k is the outcome of diffusion and migration of ionic species in the phase

$$i_k = \sum_{species} zFJ_k \tag{2-22}$$

Then, Eq. (2-21) can be rewritten as

$$\rho_k c_{pk}(\frac{\partial T_k}{\partial t} + \nabla.(v_k T_k)) = \nabla.(\lambda_k \nabla T_k) - i_k.\nabla \phi_k \tag{2-23}$$

Electrochemical reactions occur at the electrode/electrolyte interface. Heat balance over the interface results in [45, 122]

$$\lambda_e \nabla T_e.n_e + \lambda_s \nabla T_s.n_s = \bar{i}_n \eta + \bar{i}\,\Pi \tag{2-24}$$

where n represents the normal unit vectors pointing outward from a phase, with subscripts e and s denoting the phase of electrolyte and the phase of solid active material, respectively, and $\bar{i}_n$ is the local transfer current density due to the electrode reaction. The right hand side of Eq. (2-24) represents the heat generation at the electrode/electrolyte interface and is divided into two parts. The first term is the irreversible reaction heat due to the electrochemical reaction resistance at the interface, similar to Joule heating. It is proportional to the surface overpotential h of the electrode reaction and is always positive. The second term is the reversible part of the reaction heat mainly due to the entropy change of the electrode reaction. It is called Peltier heat and changes sign with changing current direction. The Peltier coefficient Π can be determined experimentally[123]. Equation (2-24) more generally can be rewritten as follows

$$\lambda_e \nabla T_e . n_e + \lambda_s \nabla T_s . n_s = \frac{\sum_j a_{sj} \bar{i}_{nj} (\eta_j + \Pi_j) + (h_k - h_m)\Gamma_{km}}{a_{km}} \tag{2-25}$$

where the phase transformation as well as multiple electrochemical reactions takes place at the electrode/electrolyte interface, subscripts *k* and *m* refer to phases *k* and *m*, respectively. Γ_{km} represents the phase transformation rate at the *k-m* interface from phase *m* to phase *k*, a_{sj} is the specific surface area active for electrode reaction *j*, a_{km} is the specific surface area of the *k-m* interface within the averaging volume V_o, and *h* is the enthalpy with subscripts *k* and *m* referring to phases *k* and *m*, respectively. The first term in the right hand side of Eq. (2-25) represents the heat effect due to electrochemical reactions and the second term refers to heat effect due to phase transformation at the electrode/electrolyte interface.

Assume V_0 is the elementary volume of V_k (where *k* = *e*, *s* or *g* for electrolyte, solid active material and gas, respectively), the volume averaging of Eq. (2-23) over the elementary volume yields

$$\rho_k c_{pk} \left[\frac{\partial \varepsilon_k < T_k >^k}{\partial T} + \nabla.(\varepsilon_k < T_k >^k < v_k >^k) \right] = \nabla.\left[(\lambda_k^{eff} + \lambda_{a,k}) \nabla < T_k >^k \right] \\ + \sum_m (Q_{km}^d + Q_{km}^\Gamma) - < i_k > . \nabla < \phi_k >^k + Q_k^{Joule} \tag{2-26}$$

with

$$Q_{km}^d = \frac{1}{V_0} \int_{A_{km}} \lambda_k \nabla T_k . n_k dA \tag{2-27}$$

$$Q_{km}^\Gamma = \frac{1}{V_0} \int_{A_{km}} \rho_k c_{pk} T_k (w_k - v_k) . n_k dA \tag{2-28}$$

$$Q_{km}^{Joule} = - < i_k >^k . \frac{1}{V_0} \int_{A_{km}} (\phi_k - < \phi_k >^k) n_k dA - \frac{1}{V_0} \int_{V_k} (i_k - < i_k >^k) . \nabla (\phi_k - < \phi_k >^k) dV \tag{2-29}$$

where λ_k^{eff} is the effective thermal conductivity of phase *k* and $\lambda_{a,k}$ is the dispersion coefficient in phase *k*. The term λ_k^{eff} includes the effect of tortuosity and may follow the Bruggeman correction. The term $\lambda_{a,k}$ represents the effect of hydrodynamic dispersion that results from variations of the microscopic velocity and temperature, and vanishes in the absence of fluid motion.

The second term on the right hand side of Eq. (2-26) is the sum of interfacial heat transfer effects. The term Q_{km}^d represents the interfacial heat-transfer rate due to conduction, and the term Q_{km}^Γ refers to the thermal effect due to the interface movement. In view of the mean values for integrals, Q_{km}^{Γ} can be modelled as the product of the average interfacial temperature by the phase transformation rate at the interface

$$Q_{km}^{\Gamma} = c_{pk}\overline{T}_{km}\Gamma_{km} \tag{2-30}$$

where $\overline{T}_{km}$ is the area-averaged temperature at the *k-m* interface. The last term on the right hand side of Eq. (2-26), Q_k^{Joule} arises from volume-averaging of the Joule heating term in Eq.(2-23). Apparently, it would vanish when electrical equilibrium holds true in a phase. However, electrical non-equilibrium is expected if the phase conductivity is low and/or the applied current density is high [10]. The conductivity of semiconductor-like active materials can be as low as 10^{-5} *S/cm*. Such a low electronic conductivity may cause a significant microscopic Ohmic drop across the active material layer coated on a substrate[10]. In this case, it can be shown that the first term on the right hand side of Eq. (2-29) is still negligible. Summation of Eq. (2-26) over all phases involved such as the electrolyte phase, the solid active material phase, and the gas phase and use of Eq. (2-27) yield

$$\begin{aligned}\sum_k \left\{\rho_k c_{pk}\left[\frac{\partial \varepsilon_k <T_k>^k}{\partial T} + \nabla.(\varepsilon_k <T_k>^k <v_k>^k)\right]\right\} &= \sum_k \left\{\nabla.\left[(\lambda_k^{eff} + \lambda_{a,k})\nabla <T_k>^k\right]\right\} \\ &+ \sum_{km}\sum_m \left(\frac{1}{V_0}\int_{A_{km}} \lambda_k \nabla T_k.n_k dA + c_{pk}\overline{T}_{km}\Gamma_{km}\right) - \sum_k \left(<i_k>.\nabla<\phi_k>^k\right)\end{aligned} \tag{2-31}$$

Applying Eq.(2-25), Eq. (2-31) becomes

$$\begin{aligned}\sum_k \left\{\rho_k c_{pk}\left[\frac{\partial \varepsilon_k <T_k>^k}{\partial T} + \nabla.(\varepsilon_k <T_k>^k <v_k>^k)\right]\right\} &= \sum_k \nabla.\left[(\lambda_k^{eff}\nabla <T_k>^k\right] + \sum_j a_{sj}\overline{i}_{nj}(\eta_j + \Pi_j) \\ &+ \sum_{km}\sum_m [(h_k - h_m)\Gamma_{km} + (c_{pk} - c_{pm})\overline{T}_{km}\Gamma_{km}] - \sum_k \left(<i_k>.\nabla<\phi_k>^k\right)\end{aligned} \tag{2-32}$$

Assuming that the local thermal equilibrium exists in the system under consideration

$$<T_k>^k = <T_m>^m = \overline{T}_{km} = \overline{T}_{mk} = T \tag{2-33}$$

Then Eq. (2-32) becomes

$$\frac{\partial(\rho c_p T)}{\partial t} + \nabla.(vT) = \nabla.\lambda\nabla T + Q \tag{2-34}$$

where

$$\rho c_p = \sum_k \varepsilon_k \rho_k c_{pk} \tag{2-35}$$

$$v = \sum_k \varepsilon_k \rho_k c_{pk} < v_k >^k \tag{2-36}$$

$$\lambda = \sum_k (\lambda_k^{eff} + \lambda_{a,k}) \tag{2-37}$$

$$Q = \sum_j a_{sj} \bar{i}_{nj} (\bar{\eta}_j + \Pi_j) + \sum_{k \neq m} \sum_m \Delta h^* \Gamma_{km} - \sum_{k=e\&s} (< i_k > . \nabla < \phi_k >^k) \tag{2-38}$$

$$\Delta h^* = (h_k - h_m) + (c_{pk} - c_{pm}) T \tag{2-39}$$

The volume averaged current density at phase of a concentrated binary electrolyte and for the phase of the solid active material are

$$< i_k > = -\kappa^{eff} \nabla < \phi_e >^e - \kappa_D^{eff} \nabla \ln < c_e^i > \tag{2-40}$$

$$< i_s > = -\sigma^{eff} \nabla < \phi_s >^s \tag{2-41}$$

According to Eq. (2-38), the heat sources inside the battery are due to electrochemical reactions, phase transformations, and Ohmic Joule heating in the electrolyte and electrodes. In order to find the heat generation rate using Eq.(2-38), the Peltier coefficient, Π_j, should be defined. An expression for Peltier coefficient has been derived by Newman [124] based on the general multicomponent transport equations and electrode reactions. With the Dufour energy flux neglected, it is reduced to

$$\Pi_j = \frac{T \Delta S_j}{n_j F} \tag{2-42}$$

where ΔS_j is the entropy change of electrode reaction *j*. The entropy changes of a number of electrode reactions are calculated [125, 126], or thermodynamic relationship between the OCP and the entropy changes can be used

$$\Delta S_j = n_j F \frac{\partial U_j}{\partial T} \tag{2-43}$$

Then Eq. (2-42) can be rewritten as

$$\Pi_j = T \frac{\partial U_j}{\partial T} \tag{2-44}$$

Substituting Eq. (2-44) and also $\bar{\eta}_j = \bar{\phi}_{se} - \bar{\phi}_{es} - U_j$ into Eq. (2-38) gives

$$Q = \sum_j a_{sj} \bar{i}_{nj} (U_j - T \frac{\partial U_j}{\partial T}) + \sum_j a_{sj} \bar{i}_{nj} (\bar{\phi}_{se} - \bar{\phi}_{es}) + \sum_{k \neq m} \sum_m \Delta h^* \Gamma_{km} - \sum_{k=e\&s} (< i_k > . \nabla < \phi_k >^k) \quad (2\text{-}45)$$

For most battery systems including Li-ion batteries, the lumped thermal model can be used, where the convection term in Eq. (2-34) can be neglected. In the lumped thermal model, the transient heat conduction is sufficient to describe temperature behaviour inside the battery

$$\frac{\partial(\rho c_p T)}{\partial t} = \nabla . \lambda \nabla T + Q \quad (2\text{-}46)$$

In summary, Eq. (2-46)along with Eq. (2-45) constitutes the general thermal model that describes the temperature field inside a battery.

The cell temperature prediction depends on energy source terms, Q in Eq. (2-46). Generally, the source term Q can be found using Eq. (2-45). In the following, this term is developed especially for Li-ion cell using the assumptions made in the section 2-1.

The source term ,Q, is considered in two parts: generation and dissipation. Generation occurs in reversible and irreversible manner. In addition to heat generation, heat is removed by dissipation of the energy to the surrounding environment.

The total heat generation can be classified into reversible heat, Q_{rev}, and irreversible heat, Q_{irr}.

$$Q_{gen} = Q_{rev} + Q_{irr} \quad \textbf{(2-47)}$$

The reversible heat is the part of energy which is needed to be released or absorbed in the electrochemical reactions to maintain the energy balance of the whole reactions, occurring at the electrode/electrolyte interface (first term in Eq. (2-45)). It can be calculated by

$$Q_{rev} = -A \int_0^L j^{Li} T \frac{\Delta S}{nF} dx \quad \textbf{(2-48)}$$

where $j^{Li} > 0$ means discharge and $j^{Li} < 0$ means charge. The entropy changes of electrode material for a reduction reaction can be obtained from [127]

$$\Delta S = nF\frac{\partial U}{\partial T} \tag{2-49}$$

The temperature dependent open circuit potential of the electrodes, $\frac{\partial U}{\partial T}$, in the positive and negative electrodes can be found from [128]

$$\frac{dU_p}{dT} = -0.353776\theta^8 + 1.3902\theta^7 - 2.2585\theta^6 + 1.9635\theta^5 \\ -0.98716\theta^4 + 0.288570\theta^3 - 0.046272\theta^2 + 0.00321580\theta - 1.9186\times10^{-5} \tag{2-50}$$

$$\frac{dU_n}{dT} = 344.1347148\times\frac{\exp(-32.96332870\theta + 8.316711484)}{1+749.0756003\exp(-34.790996460\theta + 8.887143624)} \\ -0.85202788050\theta + 0.36229922290\theta^2 + 0.2698001697 \tag{2-51}$$

respectively. The value of θ is the normalized Li concentration at the surface of the electrode

$$\theta = \frac{c_s}{c_{s,\max}} \tag{2-52}$$

The irreversible Joule heat (second term in Eq. (2-45)) due to Ohmic losses of electrons and lithium ions transport in the cell is expressed as

$$Q_j = A\int_0^L (\sigma^{eff}(\frac{\partial\phi_s}{\partial x})^2 + \kappa^{eff}(\frac{\partial\phi_e}{\partial x})^2 + \kappa_D^{eff}(\frac{\partial \ln c_e}{\partial x})(\frac{\partial\phi_e}{\partial x}))dx + I^2R_c \tag{2-53}$$

where the term I^2R_c represents the heat generation due to the contact resistance between current collector and electrode.

During charge and discharge, the energy used to overcome the activation energy of the chemical reaction would be released in the form of heat (last term in Eq. (2-45)). This heat is called polarization heat and can be expressed by

$$Q_p = A\int_0^L j^{Li}\eta dx \tag{2-54}$$

It should be noted that there is no gas phase in Li-ion cells therefore the third term in Eq. (2-45) is neglected.

In summary, the irreversible heat is the sum of Joule heat and active polarization heat

$$Q_{irr} = Q_j + Q_p \qquad \textbf{(2-55)}$$

Arrhenius equation is needed for the temperature and electrochemical model coupling

$$\Phi = \Phi_{ref} \exp(\frac{E_{act,\Phi}}{R_u}(\frac{1}{T_{ref}} - \frac{1}{T})) \qquad \textbf{(2-56)}$$

where Φ is a general temperature dependent variables, such as diffusion coefficient, conductivity of electrolyte or exchange current density, Φ_{ref} is the corresponding reference value at the reference temperature ($T_{ref} = 25^o C$). Activation energy of the evolution process of Φ is shown by $E_{act,\Phi}$. The magnitude of $E_{act,\Phi}$ shows sensitivity of the parameter to the temperature. The ionic conductivity and electrolyte diffusion coefficient are strong functions of temperature and have high value of $E_{act,\Phi}$.

The heat dissipation mechanism in Li-ion battery cell is heat convection. The inside heat convection can be determined by

$$Q_{conv} = hA(T - T_\infty) \qquad \textbf{(2-57)}$$

From the above analysis, the heat source term for the battery cell is:

$$Q = Q_{gen} + Q_{diss} \qquad \textbf{(2-58)}$$

2-3 Summary

In this chapter, the governing equations of Li-ion cell are introduced in terms of electrochemical equations and thermal equations. The details of electrochemical equations are discussed considering charge and species conservation equations. The thermal equations are reviewed based on general energy equations governing for the battery systems. The simplified thermal equations for Li-ion cell are also discussed which will be adopted in this study to calculate heat generation and heat dissipation in the following chapters. The coupling equation which connects the electrochemical and thermal equations is also presented.

Chapter 3 Numerical method to stimulate the electrochemical-thermal model for Li-ion battery cell

3-1 Introduction

The simulation plays an important role in understanding of electrochemical-thermal behavior and internal process of Li-ion batteries. The governing equations of the electrochemical-thermal model of a Li-ion cell model are described in Chapter 2. As it can be seen, the governing equations are a set of partial differential equations (PDEs) which are highly non-linear and contain nonlinear source terms. In order to solve the set of equations, various numerical methods are proposed to solve the PDEs and conduct the simulation of electrochemical-thermal processes. These existing methods mostly use the iterative methods or trial-and-error methods, which are really time-consuming and computationally expensive for the EV application stimulations.

In this chapter, a novel numerical method is proposed to accelerate the solution of the electrochemical-thermal model for a Li-ion battery cell. It is implemented in four steps. In the first step, physical analogy of electrochemical process to an electric circuit is used to solve charge conservation equations. In the second and third step, control volume method is used to solve species conservation equations. In the last step, the thermal equations are solved and the temperature distribution in the battery cell is found using the control volume methods.

3-2 Numerical procedure

The set of governing equations of an electrochemical-thermal model of a Li-ion cell introduced in Chapter 2 are a set of coupled nonlinear PDEs. The summary of the governing equations are shown in Table 3-1.

Table 3-1: A summary of electrochemical-thermal model equations

Conservation type	Equations and boundary equations	
Charge (Electrode)	$\frac{\partial}{\partial x}(\sigma^{eff}\frac{\partial \phi_s}{\partial x}) = j^{Li}$	(3-1)
	$\sigma^{eff}\frac{\partial \phi_s}{\partial x}\Big\vert_{x=0,L} = \frac{I_{applied}}{A}$	(3-2)
	$\frac{\partial \varphi_s}{\partial x}\Big\vert_{x=L_-} = \frac{\partial \varphi_s}{\partial x}\Big\vert_{x=L_-+L_{sep}} = 0$	(3-3)
Charge (Electrolyte)	$\frac{\partial}{\partial x}(\kappa^{eff}\frac{\partial \phi_e}{\partial x}) + \frac{\partial}{\partial x}(\kappa_D{}^{eff}\frac{\partial}{\partial x}\ln c_e) = -j^{Li}$	(3-4)
	$\frac{\partial \varphi_e}{\partial x}\Big\vert_{x=0} = \frac{\partial \varphi_e}{\partial x}\Big\vert_{x=L} = 0$	(3-5)
Species, Solid Phase	$r^2\frac{\partial c_s}{\partial t} = D_s\frac{\partial}{\partial r}(r^2\frac{\partial c_s}{\partial r})$	(3-6)
	$\frac{\partial c_s}{\partial r}\Big\vert_{r=0} = 0$	(3-7)
	$\frac{\partial c_s}{\partial r}\Big\vert_{r=R_s} = -\frac{j^{Li}}{D_s F}$	(3-8)
Species, Electrolyte	$\frac{\partial(\varepsilon_e c_e)}{\partial t} = \frac{\partial}{\partial x}(D_e^{eff}\frac{\partial c_e}{\partial x}) + \frac{1-t_+^0}{F}j^{Li}$	(3-9)
	$\frac{\partial c_e}{\partial x}\Big\vert_{x=0,L} = 0$	(3-10)
Thermal energy	$\frac{\partial(\rho c_p T)}{\partial t} = \nabla.\lambda\nabla T + Q$	(3-11)

There is difficulty for the existing numerical methods to solve these PDEs because (1) a set of nonlinear PDEs are numerically stiff and all the equations are highly coupled together. The iterative methods are used to solve these equations for achieving high accuracy, leading to higher computational cost. (2) The boundary conditions for charge conservation equations are the second type (Neumann boundary condition). To solve the PDEs in such a boundary condition, the initially guessed values are assigned at the computational domain to solve the governing equations, and then the solutions are modified to meet the conservation equation, consequently the nonlinear PDEs needs to be solved together with the modification of the boundary conditions iteratively. These iterative procedures are highly time-consuming.

In this chapter, a cost-effective numerical method with high accuracy is proposed. The proposed numerical method is implemented in four steps. In the first step, the discretization of the conservation of charge equations is considered in the new formulation, where the analogy between the electrochemical processes to the electric circuits is proposed and Kirchhoff's current law (KCL) and Kirchhoff's voltage law (KVL) are applied to the equivalent circuits. As a result, the distribution of ϕ_s and ϕ_e is obtained very fast as the iterations to solve the governing equations are limited in the new formulations. Moreover, the boundary conditions are changed to the first type (Dirichlet boundary condition) so that the required iteration procedure in the previous boundary conditions is eliminated. Once the charge distribution is calculated, the equations of conservation species and thermal equations are solved using the control volume method in the second, third and fourth steps. The control volume method used in the steps 2, 3 and 4 has higher stability and faster convergence among other numerical methods [129]. The detailed discussions of each step are shown in the following.

Step 1- Generally, total applied current to the battery should be conserved as there is no current loss in the battery. The total applied current enters the cell from an external circuit and enters the solid phase and then the current enters the electrolyte through surface reactions as shown in Figure 3-1. At the end of the electrode, the current enter the electrolyte phase and is carried to the other electrode through the ions. On the other electrode, this current enters the solid phase again in a reverse manner.

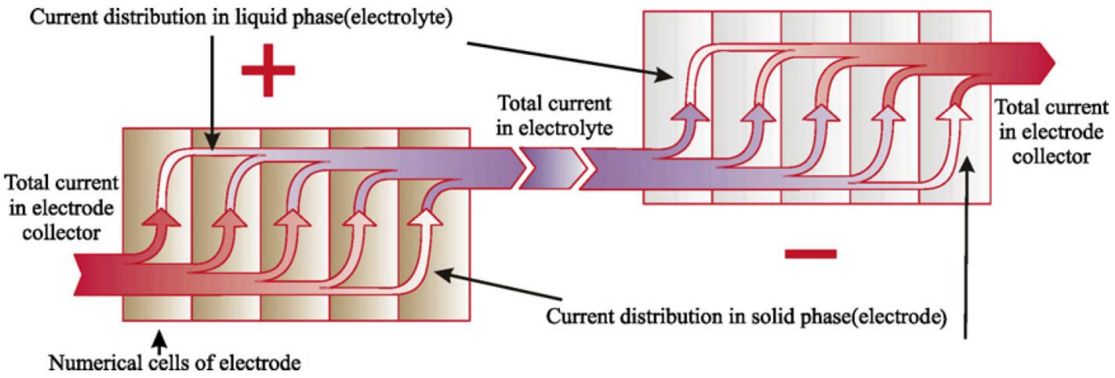

Figure 3-1: Current distribution in electrode and electrolyte

Based on the above discussion, the total applied current density in both electrodes could be divided to solid phase current density (i_s) and electrolyte phase current density (i_e). The solid phase and electrolyte phase current densities by using Eq. (3-1) and (3-4) can be expressed as

$$i_s = -\sigma^{eff} \frac{\partial \phi_s}{\partial x} \tag{3-12}$$

$$i_e = -\kappa^{eff} \frac{\partial \phi_e}{\partial x} - \frac{\kappa_D^{eff}}{c_e} \frac{\partial c_e}{\partial x} \tag{3-13}$$

The sum of Eqs. (3-1) and (3-4) gives

$$\frac{\partial}{\partial x}(i_s + i_e) = 0 \tag{3-14}$$

which implies that the total current has to be constant along the battery and can be found by considering the boundary conditions Eqs. (3-2), (3-3) and (3-5)

$$i_s + i_e = \frac{I_{applied}}{A} \tag{3-15}$$

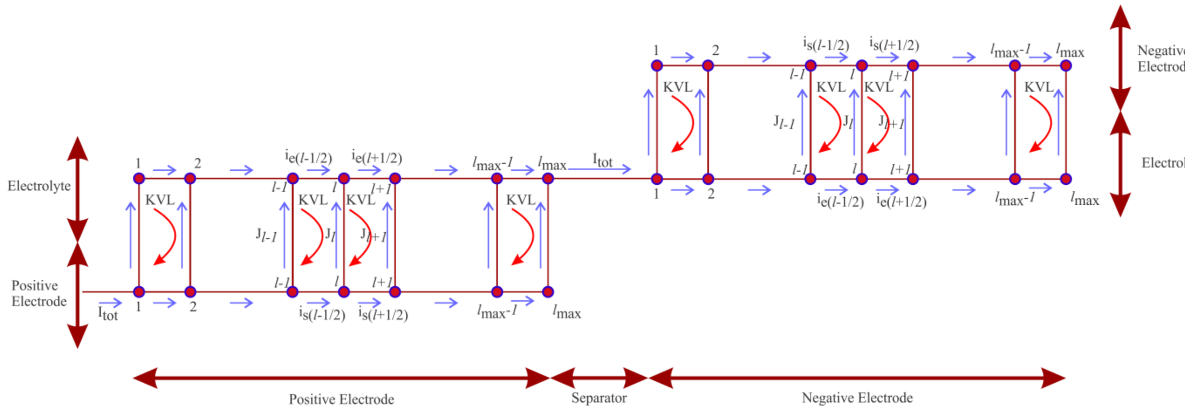

Figure 3-2: Distributions of current densities along battery thickness

As mentioned before, the current density in the solid/electrolyte interface is the transfer current density j^{Li}. Thus, three types of current densities: transfer, solid and electrolyte current densities occur in positive and negative electrodes which have been analogous to electrical circuits. As shown in Figure 3-2, each electrode is divided into a number of circuits (control volumes) to obtain the solid and electrolyte potentials. Considering there are N control volumes across the battery with the length of L and the distance of Δx between two nearby volumes. In the following formulation, $x_l + \frac{1}{2}\Delta x$ and $x_l - \frac{1}{2}\Delta x$ are denoted as $\Delta x_{l+\frac{1}{2}}$ and $\Delta x_{l-\frac{1}{2}}$, respectively. Applying KCL to the *l*th volume in solid phase and electrolyte phase gives

$$i_s(l+\frac{1}{2}) - i_s(l-\frac{1}{2}) = -J_l \tag{3-16}$$

$$i_e(l+\frac{1}{2}) - i_e(l-\frac{1}{2}) = J_l \tag{3-17}$$

where J_l is the transfer current density along the numerical volume ($J = j^{Li}\Delta x$). In Eq.(3-16), the solid current density is obtained by discretising Eq. (3-12)

$$i_s(l+\tfrac{1}{2}) = -\sigma_{l+\frac{1}{2}}^{eff} \frac{\varphi_s(l+1) - \varphi_s(l)}{\Delta x_{l+\frac{1}{2}}} \tag{3-18}$$

In this equation the ohmic resistance can be defined as $R_s(l) = \Delta x_l / \sigma_l^{eff}$. Assuming $R_s(l+\tfrac{1}{2}) = (R_s(l) + R_s(l+1))/2$, Eq. (3-18) can be rewritten as

$$i_s(l+\tfrac{1}{2}) = -\frac{\varphi_s(l+1)-\varphi_s(l)}{R_s(l+\tfrac{1}{2})} \tag{3-19}$$

In Eq. (3-17), the electrolyte current density is found by discretising Eq. (3-13)

$$i_e(l+\tfrac{1}{2}) = -\kappa_{l+\frac{1}{2}}^{eff}\frac{\varphi_e(l+1)-\varphi_e(l)}{\Delta x_{l+\frac{1}{2}}} - \frac{\kappa_D^{eff}}{c_e}\left.\frac{\partial c_e}{\partial x}\right|_{l+\frac{1}{2}} \tag{3-20}$$

The ohmic resistance can be defined as $R_e(l) = \Delta x_l / \kappa_l^{eff}$. Assuming $R_e(l+\tfrac{1}{2}) = (R_e(l)+R_e(l+1))/2$, Eq. (3-20) becomes

$$i_e(l+\tfrac{1}{2}) = -\frac{\varphi_e(l+1)-\varphi_e(l)}{R_e(l+\tfrac{1}{2})} - \frac{\kappa_D^{eff}}{c_e}\left.\frac{\partial c_e}{\partial x}\right|_{l+\frac{1}{2}} \tag{3-21}$$

In Eq. (3-21), the concentration gradient is known from the previous time step by solving species conservation equations in the next steps.

Moreover, applying KVL to the control volume l yields the relation for solid and electrolyte potentials

$$(\phi_{s(l+1)}-\phi_{s(l)})+(\phi_{e(l+1)}-\phi_{s(l+1)})+(\phi_{e(l)}-\phi_{e(l+1)})+(\phi_{s(l)}-\phi_{e(l)})=0 \tag{3-22}$$

Eq. (3-22) eliminates the iterations required by the FDM, where Eq. (3-15) should be satisfied by iterations on boundary conditions at each control volume. It is obvious that instead of the potentials in nodes, the potential differences are used to obtain the currents. Thus, three new variables are introduced:

$$\begin{aligned} \Delta V_s(l) &= \phi_s(l+1)-\phi_s(l) \\ \Delta V_e(l) &= \phi_e(l+1)-\phi_e(l) \\ \Delta V_J(l) &= \phi_s(l)-\phi_e(l) \end{aligned} \tag{3-23}$$

Using these new variables, Eq. (3-22) is rewritten as

$$\Delta V_s(l)-\Delta V_J(l+1)-\Delta V_e(l)+\Delta V_J(l)=0 \tag{3-24}$$

Substituting Eq. (3-24) into Eqs. (3-19) and (3-21) gives

$$i_s(l+\tfrac{1}{2}) = -\frac{\Delta V_s(l)}{R_s(l+\tfrac{1}{2})} \tag{3-25}$$

$$i_e(l+\tfrac{1}{2}) = -\frac{\Delta V_e(l)}{R_e(l+\tfrac{1}{2})} - \frac{\kappa_D^{eff}}{c_e}\frac{\partial c_e}{\partial x}\bigg|_{l+\frac{1}{2}} \tag{3-26}$$

To obtain the values of $\Delta V_s(l)$ and $\Delta V_e(l)$, Eqs. (3-25) and (3-26) should be solved together with Eqs. (3-16) and (3-17). In Eq.(3-24), $\Delta V_J(l)$ is a nonlinear function of J_l according to the Butler-Volmer equation. The linearization of Butler-Volmer equation is used to solve $\Delta V_J(l)$. Once $\Delta V_s(l)$, $\Delta V_e(l)$ and $\Delta V_J(l)$ have been obtained, the values of $\phi_s(l)$ and $\phi_e(l)$ can be computed using Eq.(3-22). Applying KCL and KVL to the electric circuits analogous to the electrochemical process in the battery helps to modify all second type boundary equations into only one first-type boundary condition at the first control volume: $i_s(1) = I_{applied} / A$. Since the current at the other boundary is satisfied ($i_s(l_{\max}) = I_{applied} / A$) automatically, no boundary condition is required at the end of the equivalent circuit. This massive reduction in the boundary conditions eliminates the most time-consuming part of iterations in charge transport equations. It should be noted that the potential is assumed to be zero at x=0, namely $\phi_s(1)=0$.

Step 2- In this step, a control volume method is used to find the surface concentration [130]. This method provides the surface concentration directly. The accurate surface concentration is essential because it is used in the transfer current density as well as in the calculation of the equilibrium potential for the interfacial reaction. Considering M control volumes for a lithium ion in the spatial domain [0, R_s] uniformly with the distance of Δr between two nearby volumes, $r_i + \frac{1}{2}\Delta r$ and $r_i - \frac{1}{2}\Delta r$ are respectively denoted as $r_{i+\frac{1}{2}}$ and $r_{i-\frac{1}{2}}$, integrating the left hand side of Eq. (3-6) over the interval of $\left[r_{i-\frac{1}{2}}, r_{i+\frac{1}{2}} \right]$ gives

$$\int_{r_{i-\frac{1}{2}}}^{r_{i+\frac{1}{2}}} r^2 \frac{\partial c_s}{\partial t} dr = \frac{\partial}{\partial t}\left(\int_{r_{i-\frac{1}{2}}}^{r_i} r^2 c_s dr + \int_{r_i}^{r_{i+\frac{1}{2}}} r^2 c_s dr \right) \tag{3-27}$$

Defining a function $f(r)=r^2c_s(r)$, Taylor expansion is applied to approximate the value of the function in the sub-intervals $\left\lfloor r_{i-\frac{1}{2}}, r_i \right\rfloor$ and $\left\lfloor r_i, r_{i+\frac{1}{2}} \right\rfloor$ by the following equations

$$f(r)=r_i^2c_s(i)+(r-r_i)\frac{r_i^2c_s(i)-r_{i-1}{}^2c_s(i-1)}{\Delta r}+O(\Delta r^2) \tag{3-28}$$

$$f(r)=r_i^2c_s(i)+(r-r_i)\frac{r_{i+1}{}^2c_s(i+1)-r_i^2c_s(i)}{\Delta r}+O(\Delta r^2) \tag{3-29}$$

Substituting Eqs. (3-28)and (3-29) into Eq. (3-27) yields

$$\int_{r_{i-\frac{1}{2}}}^{r_{i+\frac{1}{2}}} r^2\frac{\partial c_s}{\partial t}dr=\Delta r\frac{\partial}{\partial t}\left(\tfrac{1}{8}r_{i+1}^2c_s(i+1)+\tfrac{6}{8}r_i^2c_s(i)+\tfrac{1}{8}r_{i-1}^2c_s(i-1)\right) \tag{3-30}$$

Similarly, integrating the right hand side of the Eq.(3-27) and substituting it into Eq. (3-27)

$$\begin{aligned}&\Delta r\frac{\partial}{\partial t}\left(\tfrac{1}{8}r_{i+1}^2c_s(i+1)+\tfrac{6}{8}r_i^2c_s(i)+\tfrac{1}{8}r_{i-1}^2c_s(i-1)\right)=\\&\left(D_s\left(\frac{c_s(i+1)+c_s(i)}{2}\right)r_{i+\frac{1}{2}}^2\frac{c_s(i+1)-c_s(i)}{\Delta r}-D_s\left(\frac{c_s(i)+c_s(i-1)}{2}\right)r_{i-\frac{1}{2}}^2\frac{c_s(i)-c_s(i-1)}{\Delta r}\right)\end{aligned} \tag{3-31}$$

The volume V_i of the corresponding shell over the interval $\left\lfloor r_{i-\frac{1}{2}}, r_{i+\frac{1}{2}} \right\rfloor$ is defined as

$$V_i=\frac{(r_i+\frac{\Delta r}{2})^3-(r_i-\frac{\Delta r}{2})^3}{3}=r_i^2\Delta r+\frac{1}{12}\Delta r^3 \qquad \text{3-32)}$$

The term $r_i^2\Delta r$ in Eq. (3-32) is replaced by the definition of V_i in Eq. (3-31)

$$\begin{aligned}&\Delta r\frac{\partial}{\partial t}\left(\tfrac{1}{8}V_{i+1}c_s(i+1)+\tfrac{6}{8}V_ic_s(i)+\tfrac{1}{8}V_{i-1}c_s(i-1)\right)=\\&\left(D_s\left(\frac{c_s(i+1)+c_s(i)}{2}\right)r_{i+\frac{1}{2}}^2\frac{c_s(i+1)-c_s(i)}{\Delta r}-D_s\left(\frac{c_s(i)+c_s(i-1)}{2}\right)r_{i-\frac{1}{2}}^2\frac{c_s(i)-c_s(i-1)}{\Delta r}\right)\end{aligned} \tag{3-33}$$

The matrix form of Eq. (3-33) is

$$M\frac{\partial c_s}{\partial t}=h(c_s) \tag{3-34}$$

where $h(c_s)$ is the right hand side of Eq. (3-33) and M is a tri-diagonal matrix as followings

$$M = \begin{bmatrix} \frac{3}{4}V & \frac{1}{8}V_2 & 0 & 0 & \cdots & 0 & 0 & 0 \\ \frac{1}{4}V_1 & \frac{6}{8}V_2 & \frac{1}{8}V_3 & 0 & \cdots & 0 & 0 & 0 \\ 0 & \frac{1}{8}V & \frac{6}{8}V_3 & \frac{1}{8}V_4 & \cdots & 0 & 0 & 0 \\ \vdots & \vdots & \vdots & \vdots & \ddots & \vdots & \vdots & \vdots \\ 0 & 0 & 0 & 0 & \cdots & \frac{1}{8}V_{N-2} & \frac{6}{8}V_{N-1} & \frac{1}{4}V_N \\ 0 & 0 & 0 & 0 & \cdots & 0 & \frac{1}{8}V_{N-1} & \frac{3}{4}V_N \end{bmatrix} \tag{3-35}$$

To obtain the time dependent solution, the combination of the forward and backward Euler's method based on the central difference scheme is used with the second order of accuracy in the time discretization. Given an initial concentration profile, c_s^t, and the time step Δt, the prediction of the concentration profile $c_s^{t+\Delta t}$ at time $t+\Delta t$ satisfies

$$M\frac{c_s^{t+\Delta t} - c_s^t}{\Delta t} = \tfrac{1}{2}(h(c_s^{t+\Delta t}) + h(c_s^t)) \tag{3-36}$$

In the right hand side of the Eq.(3-36), when the diffusion coefficient Ds is a constant, the function h(cs) is linear. Thus, it takes only one step to reach the solution.

Step 3- The control volume method is also used to find the electrolyte concentration. Considering there are O control volumes across the battery with the length of L and the distance of Δx between two nearby volumes. In the following formulation, $x_i + \tfrac{1}{2}\Delta x$ and $x_i - \tfrac{1}{2}\Delta x$ are denoted as $x_{i+\frac{1}{2}}$ and $x_{i-\frac{1}{2}}$, respectively. Integrating both sides of species conservation equation in electrolyte

$$\int_{x_{i-\frac{1}{2}}}^{x_{i+\frac{1}{2}}} \frac{\partial \varepsilon_e c_e}{\partial t} dx = \int_{x_{i-\frac{1}{2}}}^{x_{i+\frac{1}{2}}} \left(\frac{\partial}{\partial x}\left(D_e^{eff}\frac{\partial c_e}{\partial x}\right) + \frac{1-t_+^0}{F} j^{Li}\right) dx \tag{3-37}$$

Defining $\frac{1-t_+^0}{F} j^{Li} = S$, the discretised format of the Eq. (3-37) can be expressed as:

$$\Delta x \frac{\partial \varepsilon_e c_e}{\partial t} = D_e^{eff}\left(\frac{c_e(i-1) - c_e(i)}{\Delta x} - \frac{c_e(i) - c_e(i+1)}{\Delta x}\right) + S(i) \tag{3-38}$$

To march in time, the combination of the forward and backward Euler's method based on the central difference scheme is used again. Assume that an initial electrolyte concentration profile is c_e^t and the time step Δt, the prediction of concentration profile $c_e^{t+\Delta t}$ at time $t+\Delta t$ satisfies:

$$\varepsilon_e \frac{c_e^{t+\Delta t} - c_e^t}{\Delta t} = \tfrac{1}{2}(g(c_e^{t+\Delta t}) + g(c_e^t)) \tag{3-39}$$

where $g(c_e)$ is the right hand side of Eq (3-38).

Step 4- In this step, the control volume method is applied to the conservation of energy equation along the electrode to find the temperature. Considering there are H control volumes across the battery with the length of L and the distance of Δx between two nearby volumes. In the following formulation, $x_i + \tfrac{1}{2}\Delta x$ and $x_i - \tfrac{1}{2}\Delta x$ are denoted as $x_{i+\frac{1}{2}}$ and $x_{i-\frac{1}{2}}$, respectively. Integrating both sides of Eq. (3-11) gives

$$\int_{x_{i-\frac{1}{2}}}^{x_{i+\frac{1}{2}}} \frac{\partial \rho c_p T}{\partial t} dx = \int_{x_{i-\frac{1}{2}}}^{x_{i+\frac{1}{2}}} \left(\frac{\partial}{\partial x}\left(\lambda \frac{\partial T}{\partial x}\right) + Q(i)\right) dx \tag{3-40}$$

It should be noted that at each control volume the value of the heat source (Q(i)) should be calculated using the heat generation equation introduced in Chapter 2.

To march in time, the initial temperature profile is T^t and the time step Δt, the prediction of temperature profile $T^{t+\Delta t}$ at time $t+\Delta t$ satisfies:

$$\rho c_p \frac{T^{t+\Delta t} - T^t}{\Delta t} = \tfrac{1}{2}(p(T^{t+\Delta t}) + p(T^t)) \tag{3-41}$$

where $p(T)$ is the right hand side of Eq (3-39).

3-3 Experimental verification

The proposed method is applied to solve the governing equations of a 26650 lithium ion battery. The parameters required in the equations are shown in Table 3-2.

Table 3-2: Battery parameters

Parameter	Negative electrode	Separator	Positive electrode
Thickness (μm)	34[b]	25 [b]	70 [b]
Particle Radius R_s (μm)	5 [b]	-	0.05 [b]
Active material volume fraction ε_s	0.58 [a]	-	0.374 [a]
Electrolyte phase volume fraction ε_e	0.357 [a]	0.5 [a]	0.444 [a]
Conductivity of solid active material σ (Scm^{-1})	1.0 [c]	-	0.038 [c]
Effective conductivity of solid active material	$\sigma^{eff} = \varepsilon_s \sigma^{1.5}$ [b]	-	$\sigma^{eff} = \varepsilon_s \sigma^{1.5}$ [b]
Transference number t_+^0	0.363 [c]		
Electrolyte phase ionic conductivity κ (Scm^{-1})	$\kappa = 0.0158 c_e \exp(0.85 c_e^{1.4})$ [d]		
Effective electrolyte phase ionic conductivity	$\kappa^{eff} = (\varepsilon_e)^{1.5} \kappa$ [d]		
Effective electrolyte phase diffusion conductivity	$\kappa_D^{eff} = \frac{2RT\kappa^{eff}}{F}(t_+^0 - 1)$ [d]		
Electrolyte phase diffusion coefficient D_e ($cm^2 s^{-1}$)	2.58×10^{-6} [d]		
Effective electrolyte phase diffusion coefficient	$D_e^{eff} = (\varepsilon_e)^{1.5} D_e$ [d]		
Solid phase diffusion coefficient D_s ($cm^2 s^{-1}$)	3.9×10^{-10} [d]	-	1.0×10^{-9} [d]

Maximum solid phase concentration $c_{s,\max}$ ($mol\ m^{-3}$)	30.54[e]	-	22.86[e]
Change transfers coefficients α_a, α_c	0.5,0.5[c]	-	0.5,0.5[c]
Active surface area per electrode unit volume a_s	$a_s = \frac{3\varepsilon_e}{R_s}$[c]	-	$a_s = \frac{3\varepsilon_e}{R_s}$[c]
Electrode plate area A (cm^2)	1800[b]	-	1800[b]
Film resistance on the electrode surface, R_f ($cm^2 s^{-1}$)	20[a]	0	20[a]

Notes: [a] Estimated Values, [b,c,d,e] Values adopted from Ref.[131], [132] , [83] and [133], respectively.

In order to verify the proposed method, the discharge behaviour of the Li-ion battery is simulated and compared with experimental data.

Figure 3-3 shows the battery potentials versus the discharge capacity under various discharge rates of 0.5C, 1C, 2C and 4C at the temperature of 20°C. The results of the proposed method agree very well with experimental data at the average error of 0.096% in 1C discharge rate. It proves that the proposed method can accurately simulate lithium ion battery behaviour.

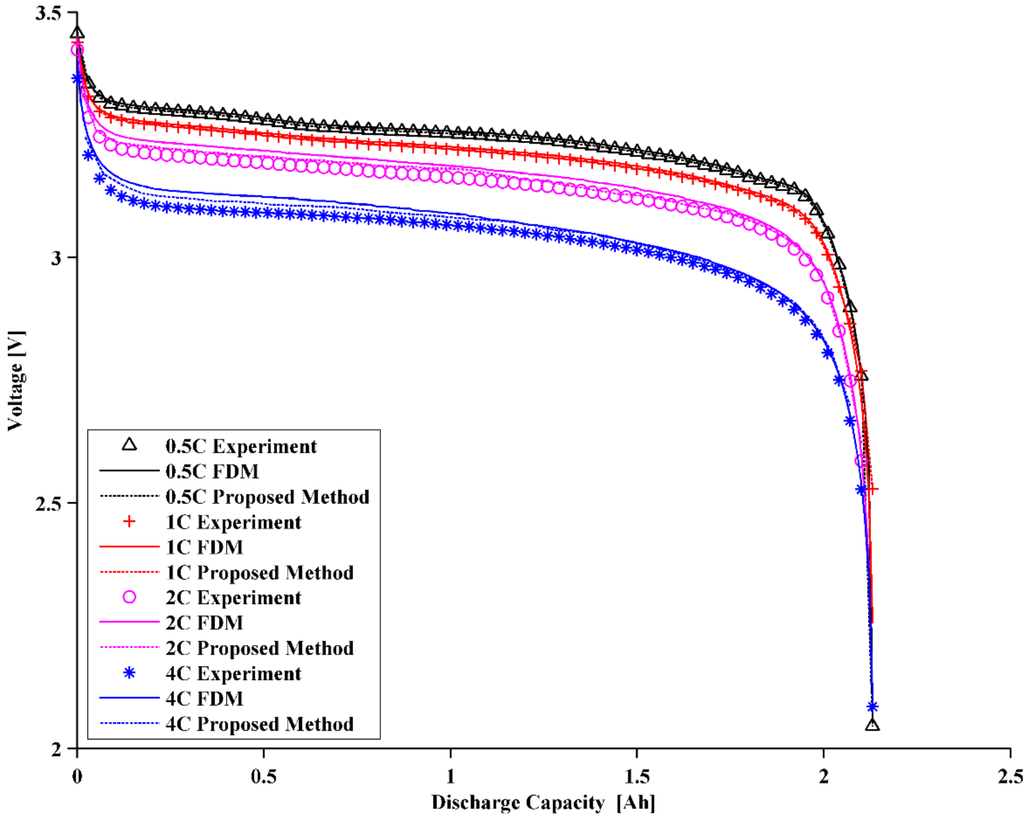

Figure 3-3: Comparison of discharge curves between proposed method, FDM and experimental data at various discharge rates

In order to validate the effectiveness of the proposed method, the predicted and measured temperature of the Li-ion cell are compared under different discharge rates: 0.5C, 1C, 2C and 4C as shown in Figure 3-4, where the single cell is kept in the ambient temperature of $20^o C$ for at least 2 hours at the beginning of each experiment to reach thermal equilibrium as monitored by a thermocouple which has been mounted on the surface of the cell. It can be seen that the simulation results agree well with the experimental results with the average error of 1.24% for all discharge rates. It proves that the proposed method can accurately predict the temperature response of the cell at low, medium and high discharge rates. The temperature rise of the cell is enhanced by the discharge rate as the heat generation is dominated by the joule heat and Ohmic losses of the lithium ion transport.

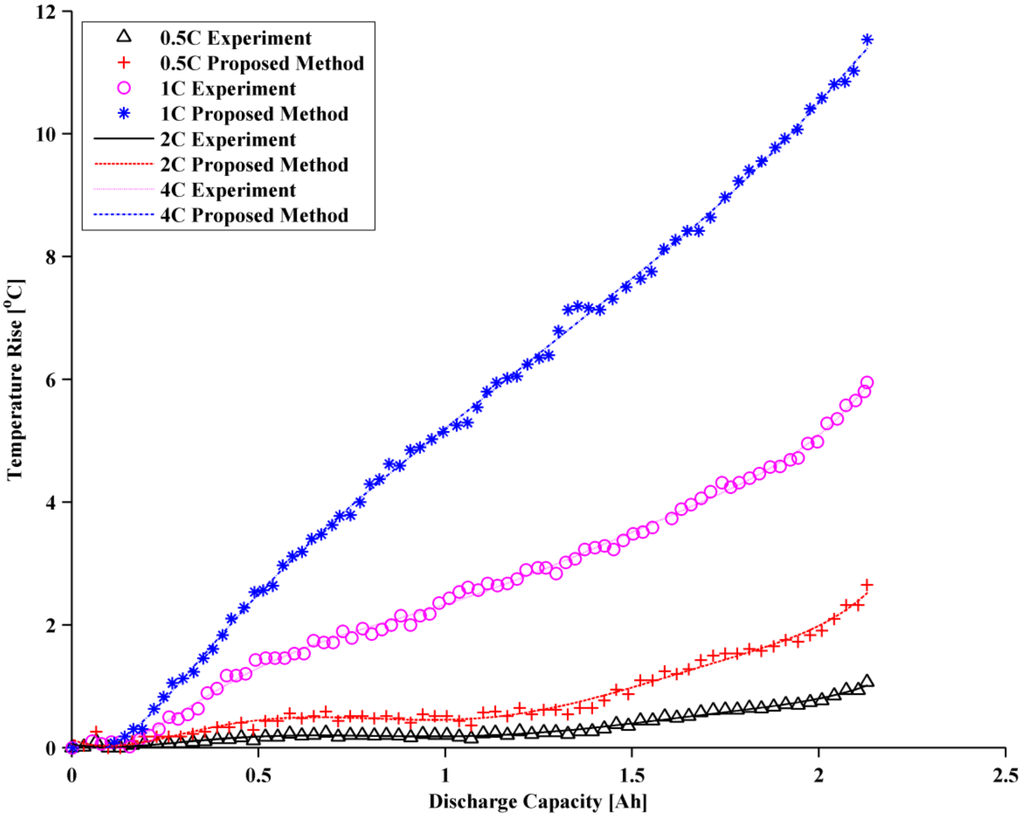

Figure 3-4: Comparison of predicted and measured temperatures at various discharge rates

3-3 Effectiveness of the proposed method

The proposed method is implemented in a C++ program language in Microsoft Visual Studio 2010 on Windows 7 platform running on a PC with Intel W3550 CPU. The total required computational time is 62s for FDM while the time is 28s for the proposed method when the 1C discharge rate, ambient temperature of 20°C and the initial electrolyte concentration of 1 $molm^{-3}$ are applied. It shows the proposed method faster than the FDM by 2.2 times. The high speed of the proposed method is because of (1) reducing the iteration in the steps 1 and 2, (2) changing the boundary conditions from the second type to the first type in the step 1, and (3) adopting fast control volume method in the steps 2, 3 and 4, which provides the opportunity to allow bigger step size in both time and space domains.

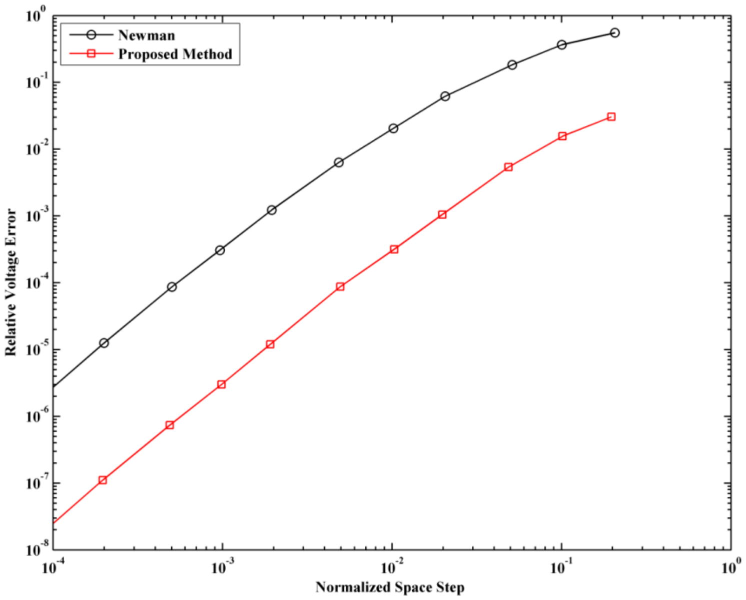

(a)

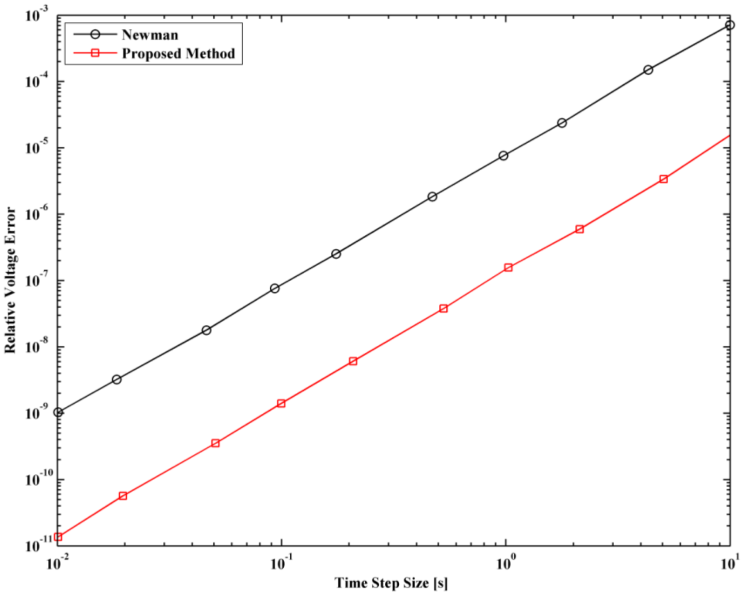

(b)

Figure 3-5: Relative error convergence of proposed method and FDM in various step sizes in (a) space, (b) time

Different grid sizes in terms of space steps in the battery thickness are studied for the first step in the proposed and FDM methods. Figure 3-5(a) shows the relative error of the voltage prediction in 1C discharge rate. The solution from a very fine grid mesh (12900 control volumes) is used as a reference solution in the error convergence test. As can be seen from Figure 3-5(a), for a fixed number of points, the proposed method is more accurate than the FDM by a factor of about 100. The normalized space step of 0.02 is selected for the rest of the simulations. By choosing this value, the real space step in the negative electrode, separator and positive electrodes are $0.68\,\mu m$, $0.5\,\mu m$ and $1.4\,\mu m$, respectively, corresponding to their own thicknesses.

The same study has been done for the second and third steps. Finally, the values of the normalized space step in the steps 2 and 3 are 0.005 and 0.01, respectively, for the rest of the simulation. Consequently, the real space step for the lithium ion in the negative and positive electrodes are $0.025\,\mu m$ and $0.00025\,\mu m$ with respect to their own radii in the step 2; whereas, the real space step in the negative electrode, separator and positive electrode are $0.34\,\mu m$, $0.25\,\mu m$, and $0.7\,\mu m$, respectively, corresponding to their own thicknesses. The bigger step size cannot be applied to EV driving cycles as it may cause large errors and high discrepancies between the calculated results from the model and those from the experiments.

For the time dimension in step 1, the number of the control volumes is fixed to 150 and the time step sizes are varied. The solution with very small time step sizes ($0.001s$ per step) is chosen as the reference solution. Figure 3-5(b) illustrates the time step study for the proposed method and FDM. At a certain time step, the proposed method is more accurate than FDM by the average factor of 10. In this paper, the time step of 10s is used for the proposed method while the time step has to be decreased to 2s for the FDM, to achieve the required relative error. The same study has been done for steps 2, 3 and 4. Based on the results, Δt in steps 2, 3, and 4 is selected to be 3s for the rest of the simulations in the proposed method. Figure 3-5(b) demonstrates the constant time steps only. The adaptive time stepping may be used in the constant rates, as it reduces the computational time. However, at the various discharge rates, adaptive time stepping does not reduce the total computational time as the required time step should be recalled at each step. The main purpose of this thesis is for EV applications with varying discharge rates (EV driving cycles), the adaptive time steps haven't been applied.

Assume the initial concentration of 1 $moldm^{-3}$, Figure 3-6 shows the electrolyte concentration profile comparison across the battery thickness in the 1C discharge rate at the beginning, 30 minutes later and at the end of the discharge. It can be observed that the electrolyte concentration profiles for both the proposed method and the FDM are in good agreement. Moreover, the concentration with non-zero value shows that, in this discharge current rate, the effect of concentration polarization is not so high to utilize all of electrode material.

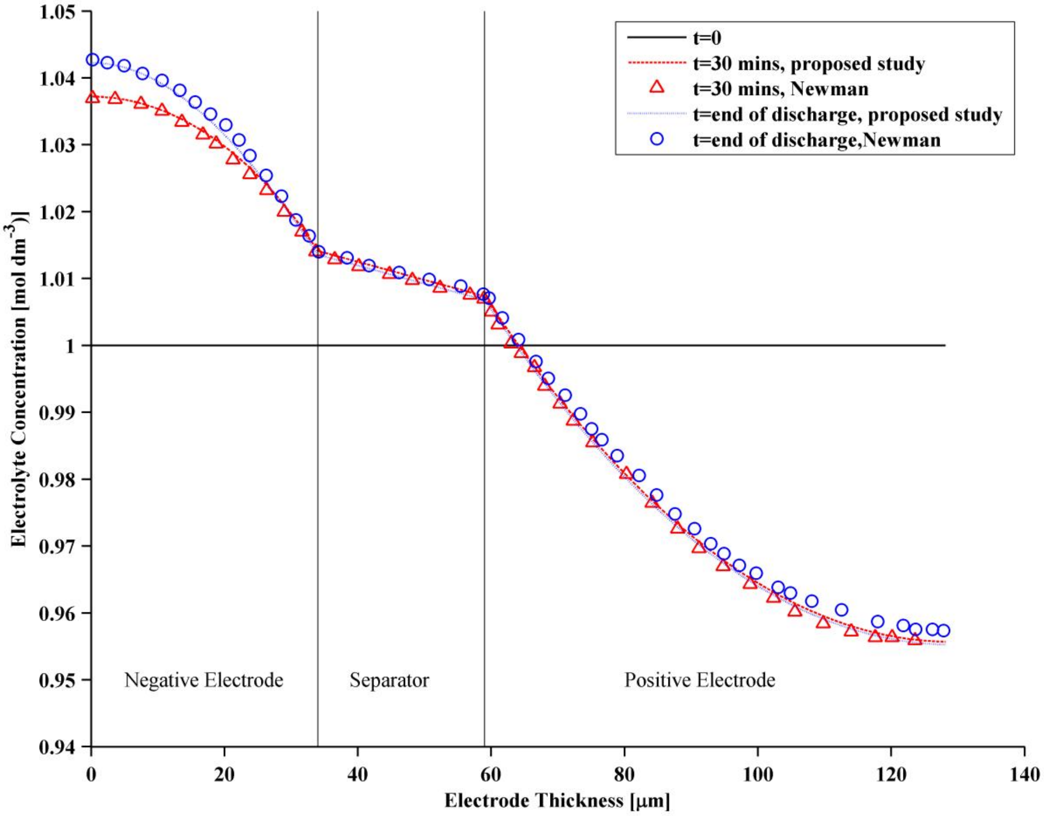

Figure 3-6: Electrolyte concentration profile along battery thickness at 1C discharge rate

In Figure 3-7, the electrolyte potential along the battery thickness is compared between the proposed method and the FDM. Both results match very well, which indicates the ability of the proposed method to accurately predict the internal properties of the lithium ion battery.

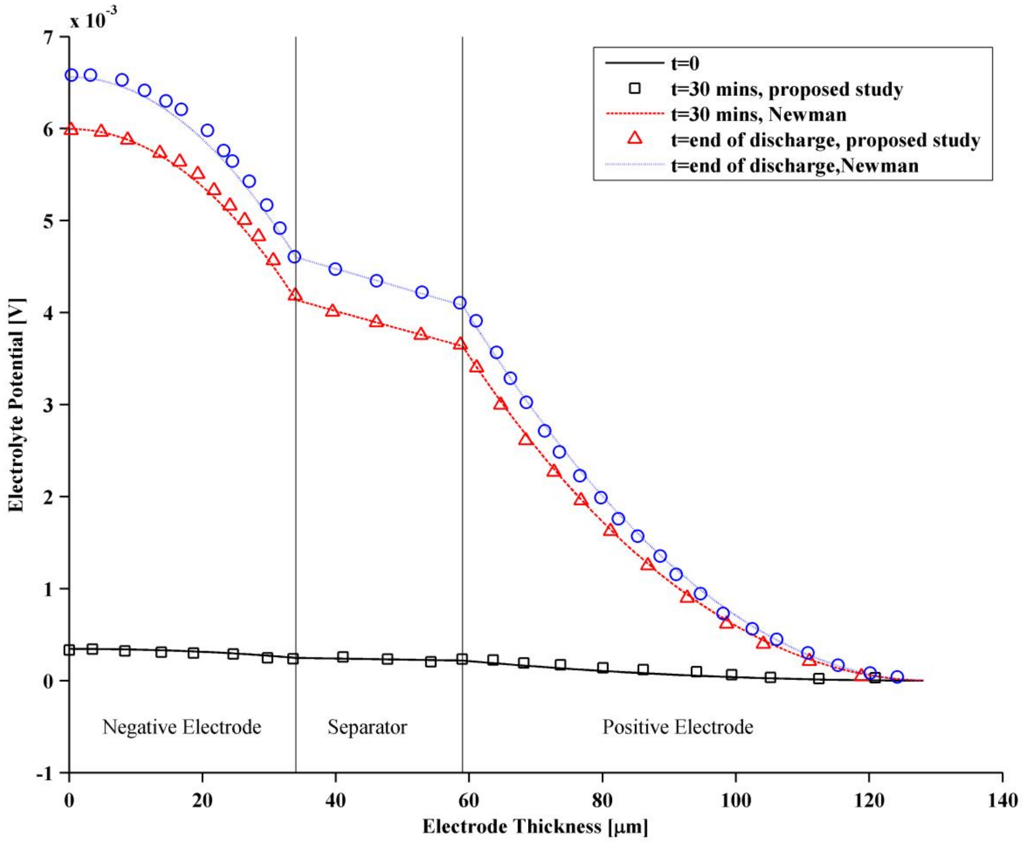

Figure 3-7: Electrolyte potential profile along battery thickness at 1C discharge rate

3-4 Summery

In this chapter, a new numerical method to solve an electrochemical-thermal model for a Li-ion battery is proposed. This method is based on the integration of Kirchhoff's laws and the control volume method by using the analogy of electrochemical processes to electric circuits. The comparison between the proposed method and the finite difference method shows that the proposed method significantly shortens simulation time. The simulation results have compared with experimental data to validate the high accuracy of the proposed method.

Chapter 4 Electrochemical-thermal model for Li-ion battery pack

4-1 Introduction

Li-ion battery cells are considered as the most ideal energy storage equipment for EVs due to their high power, high density, long cycle life and low self-discharge rate. However, the temperature behaviour of Li-ion battery cell during charging and discharging processes under EV driving cycles needs more investigations in terms of thermal managements. The Li-ion battery pack consists of multiple cells in series and parallel configuration to achieve the required current, voltage, power and energy in EVs. Under charge and discharge processes the temperature of the battery cells in the battery pack are increased gradually which needs to be observed accurately to prevent them from gradually rising to the maximum allowable value, leading to the acceleration of the degradation rate and thermal runaway [134, 135]. Thus, a thermal management which can protect the battery cells from high temperature rise is required to be designed for the Li-ion battery packs in EV applications. In this regard, the characteristics of heat generation and heat dissipation in the battery packs should be studied comprehensively to ensure that the battery cell temperature can be effectively controlled below the limiting values under EV driving cycles.

To examine the Li-ion battery pack behaviour at different operating conditions under various driving cycles, numerical simulation is a more cost effective method than the costly and time-consuming experimental tests. Also numerical simulations give the crucial details of heat generation, heat dissipation and battery cell temperature changes inside the battery which cannot be observed by using experiments. Hence, developing a theoretical electrochemical-thermal to predict the heat generation and heat dissipation rates of each battery cell within the battery pack is significant and crucial for thermal management's designs in EVs.

In the previous chapters, an electrochemical-thermal model for Li-ion cell is developed and the novel numerical method to solve the governing equations are proposed and validated against experiments. In this chapter, the improved theoretical electrochemical-thermal model coupled with the thermal resistive network is proposed to accurately predict the heat generation rates, heat dissipation rates and temperature rise of lithium ion cells within a battery pack. The experimental data verifies the accuracy of the proposed model under constant discharge current and variable discharge current based on EV driving cycles.

4-2. Model development

Figure 4-1 shows the components and arrangement of a typical lithium ion battery pack for electric vehicle application [21, 136]. The battery cells within the battery packs could be cylindrical (Figure 4-1(a)) or pouch designs (Figure 4-1(b)). As can be seen in Figure 4-1, the Li-ion battery pack consists of a number of Li-ion cells arranged in series and parallel.

The battery packs initial temperature changes because of internal heat. In order to observe the Li-ion battery pack thermal behaviour, the electrochemical-thermal model for the Li-ion battery pack is developed. In this section, the governing equations of electrochemical-thermal model are discussed in terms of electrochemical equations and thermal equations.

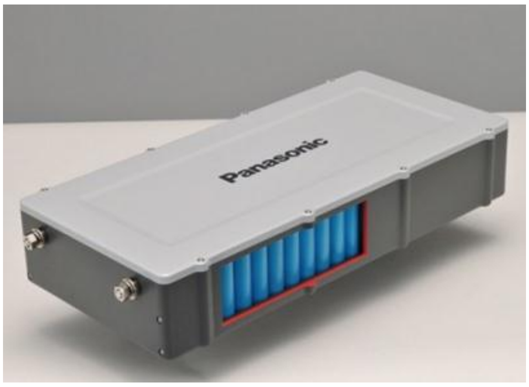

(a)

(b)

Figure 4-1: Schematic view of Li-ion battery pack consisting of (a) cylindrical battery cells, (b) pouch battery cells

4-1-1 Electrochemical model

In the developed thermal-electrochemical model for battery packs, the governing equations of electrochemical model stay the same as the numerical model for Li-ion battery cell which have been explained in details in Section 2-2-1 and 2-2-2 in Chapter 2. In the following, only thermal model will be introduced.

4-1-2 Thermal model

The temperature of a single cell in the battery pack can be calculated by the general conservation energy equation

$$\frac{\partial}{\partial t}(\rho c_p T) = \nabla.(\lambda \nabla T) + Q \tag{4-1}$$

The energy source term, Q in Eq. (4-1) is considered as generation heat and dissipation heat. The heat generation equations are introduced in Chapter 2 and briefly noted in Table 4-1. In developing the heat generation equations it is assumed that the temperature of the battery cell is distributed uniformly and also the thermal capacity and mass of the battery cell are even with no differences.

Table 4-1: Heat generation equations

Heat generation term	Equation
Reversible	$Q_{rev} = -A\int_0^L j^{Li} T \frac{\Delta S}{nF} dx$ (4-2)
Irreversible Joule	$Q_j = A\int_0^L (\sigma^{eff} (\frac{\partial \varphi_s}{\partial x})^2 + \kappa^{eff} (\frac{\partial \varphi_e}{\partial x})^2 + \kappa_D^{eff} (\frac{\partial \ln c_e}{\partial x})(\frac{\partial \varphi_e}{\partial x}))dx + I^2 R_c$ (4-3)
Irreversible polarization	$Q_p = A\int_0^L j^{Li} \eta dx$ (4-4)

In addition to heat generation in a battery pack, heat dissipation plays an important role in its thermal behaviour. There are different heat dissipation mechanisms in a battery cell (Figure 4-2 [137]); namely:

1. Heat conduction: which is an exchange of thermal energy, in the presence of temperature gradient, from more energetic to the adjacent less energetic particles of a substance due to interactions between particles;

2. Heat convection: which is the transfer of the thermal energy between a surface and a moving fluid by the bulk motion of the fluid (*i.e.* cooling air in the Li-ion battery packs)

As the cell is an opaque system, the radiation heat transfer inside the battery pack is insignificant. Also it is assumed that the inlet air temperature to the battery pack is equal to the surrounding temperature.

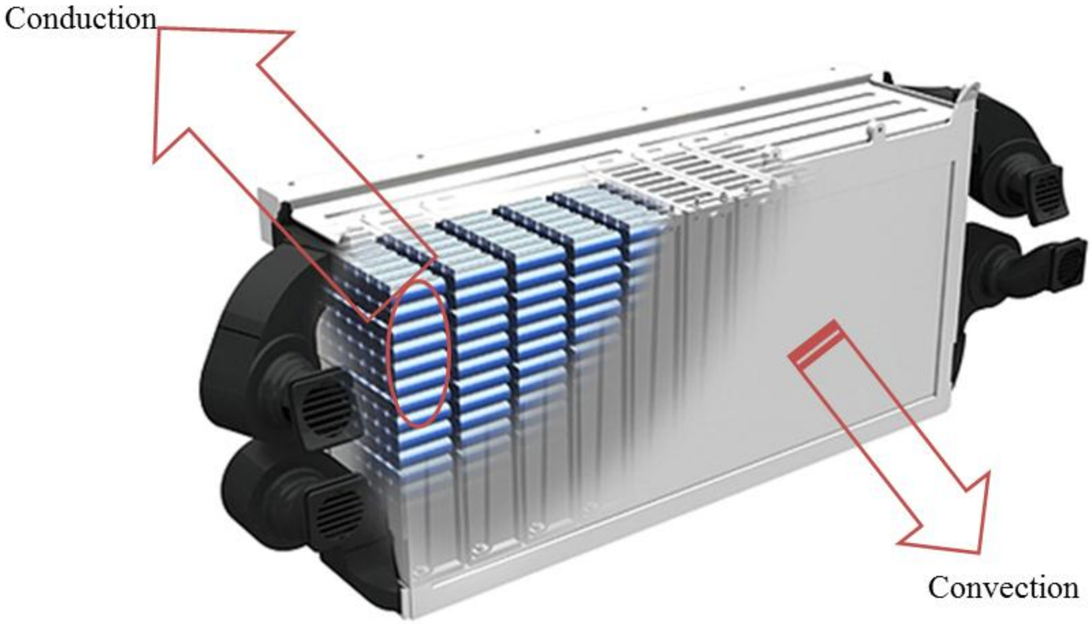

Figure 4-2: Schematic illustration of different systems of heat dissipation in a Li-ion battery pack

Convection is one of the most important mechanisms of heat dissipation. When the battery case temperature exceeds the ambient temperature, the convection starts to dissipate the thermal energy. The inside heat convection can be determined by

$$Q_{conv} = hA(T - T_{\infty}) \tag{4-5}$$

Eq.(4-5) shows that the convective heat dissipation is proportional to the temperature difference between the battery case and the ambient. The convective heat transfer can be either natural (free) convection or forced convection. In the natural (free) convection, the fluid (air in the Li-ion battery packs) moves naturally by differences in the fluid densities occurring because of temperature gradients. In the forced convection, by contrast, the fluid moves by an external source, such as cooling fan. The heat transfer coefficient in natural convection and forced convection is defined as [138]

$$h = \begin{cases} h_{forced} = 30\left(\dfrac{\dot{m}}{5\rho_{air} A_c}\right)^{0.8} \\ h_{natural} = 4 \end{cases} \tag{4-6}$$

The battery pack used in this study is arranged in 4S4P which consists of 4 strings in parallel with each string having 4 cells in series. As a result, this pack has a total of 16 cells. To show this arrangement clearly, the pack without casing can be seen in Figure 4-3(a). A resistive network is proposed to describe conductive heat transfer as shown in Figure 4-3(b).

(a)

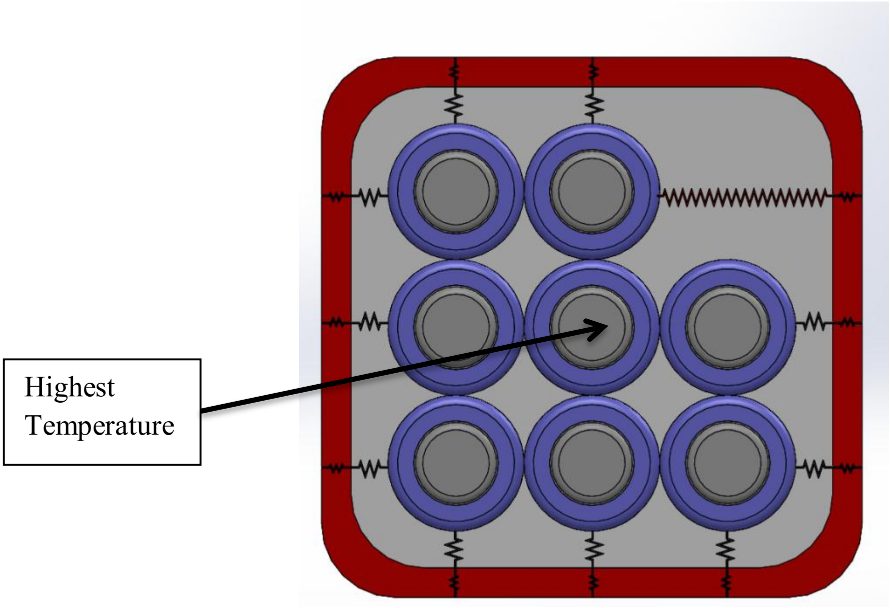

(b)

Figure 4-3: Battery pack (a) 3D view, (b) front view

The heat conduction mechanism inside the battery pack occurs to dissipate the heat from cells to the air and casing. By using the thermal and electrical analogy, the thermal resistances are considered between the cell to the casing and from the casing to the environment, where the casing has its equivalent thermal resistances and so does each cell in its four sides: left, right, up and down. The heat is transferred from the side with the smallest thermal resistance. The cell with less neighbouring cells has less heat resistance which means a better heat conductivity and lower cell temperature.

The value of the heat conduction resistances can be determined by:

$$R = \frac{d}{\lambda} \tag{4- 7}$$

where d and λ are the thickness (or distance) and the thermal conductivity of air or casing, respectively. The thermal conductivity of the air is $0.0257\ Wm^{-1}K^{-1}$ and the distance between battery cells and casing is $0.5cm$ in the battery pack in this paper. The casing of the battery pack is made of Acrylonitrile Butadiene Styrene (ABS) with the thickness of $0.20cm$ and the thermal conductivity of $0.25\ Wm^{-1}K^{-1}$.”

The total amount of the heat conduction from the cell to the neighbouring cells or environment is proportional to the temperature difference between the cell and the surroundings:

$$Q_{cond.} = \sum \frac{T_{ambient} - T}{R} \tag{4-8}$$

where $T_{ambient}$ is the temperature of the surroundings.

From the above analysis, the heat source term for the battery pack is:

$$Q = Q_{gen} + Q_{diss} \tag{4-9}$$

4-2 Numerical procedure

To find the solution of the governing equations, the same numerical method proposed in Chapter 3 for Li-ion cells is used. For every single cell located in the battery pack, the numerical procedure shown in Figure 4-4 is followed. First, all the parameters are initialized and the boundary conditions for the governing equations are set up. Then, the proposed numerical method for the Li-ion cell is applied to find the electrochemical properties. With the calculation results of the electrochemical properties, the reversible heat generation is calculated by Eq.(4-2), and the irreversible heat generation is obtained by Eqs. (4-3) and (4-4). Thus, the total heat generation rate at battery cell at time t can be computed by $Q_{gen} = Q_{rev} + Q_{irr}$. On the other hand, the heat dissipation is determined by Eqs. (4-5) and (4-8). By combining Q_{gen} and Q_{diss}, the total net heat generation can be calculated to determine the temperature change of the battery cell from Eq.(4-1).

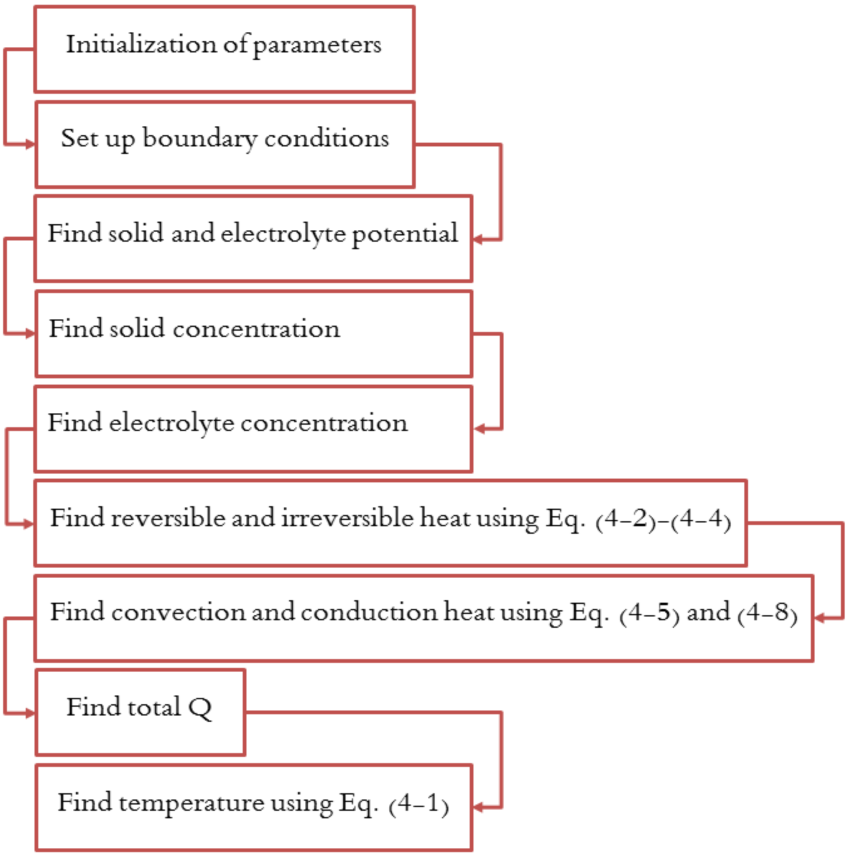

Figure 4-4: Flowchart of numerical procedure

4-4 Experimental verification

4-4-1 Battery pack

The battery pack with 4S4P configuration has been selected for the experimental verification. This battery pack has 9.2Ah with the normal voltage of 14.2V as shown in Figure 4-5, which consists of 16 A123 26650 cells with each cell having 2.3Ah. In experiments, thermocouples are attached on the cell surfaces to measure their temperatures in real time. All experiments are carried out under constant ambient temperature in a temperature chamber. Before each test, lithium ion battery cell or pack are restored for at least 2 hours in order to reach thermal equilibrium, as monitored by thermocouples. All charging and discharging experiments in this chapter are conducted by using Arbin Instruments.

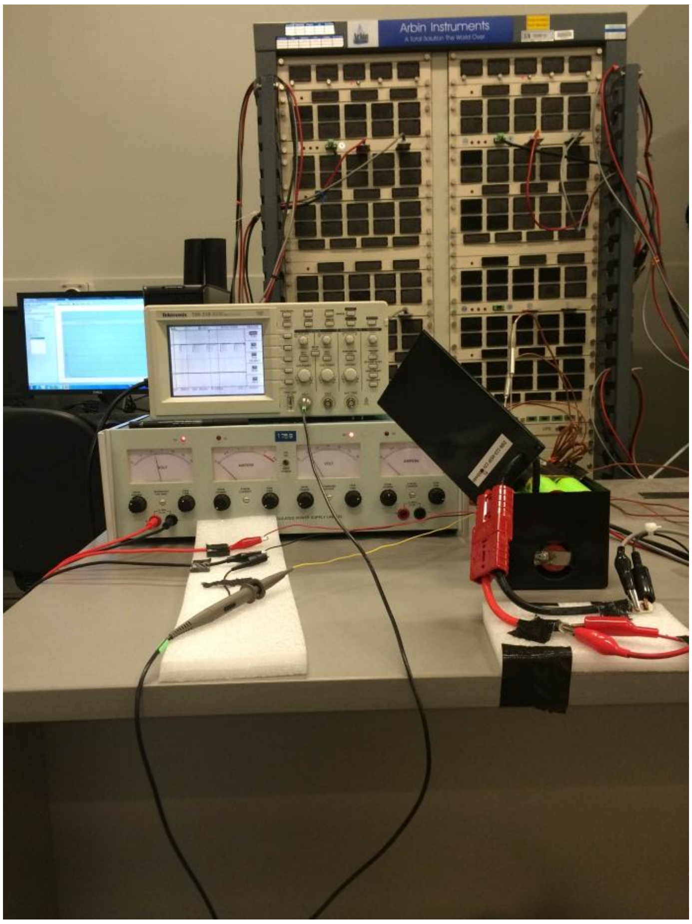

Figure 4-5: Experimental setup for 14.4V lithium ion battery pack

Since the cell with the highest temperature is obviously in the centre of the battery pack, the calculation of the battery pack temperature will actually focus on this cell which is indicated by an arrow in Figure 4-3(b) because if this cell temperature can be kept within the maximum allowable temperature all the cells in the pack should work safely. Therefore, the temperature of the centre cell will represent the battery pack temperature in the following section. To measure the temperature of the centre cell, the battery pack is kept in the ambient temperature of $20^o C$ for at least 2 hours to reach thermal equilibrium at the beginning of each experiment as monitored by a thermocouple which has been mounted on the surface of the centre cell.

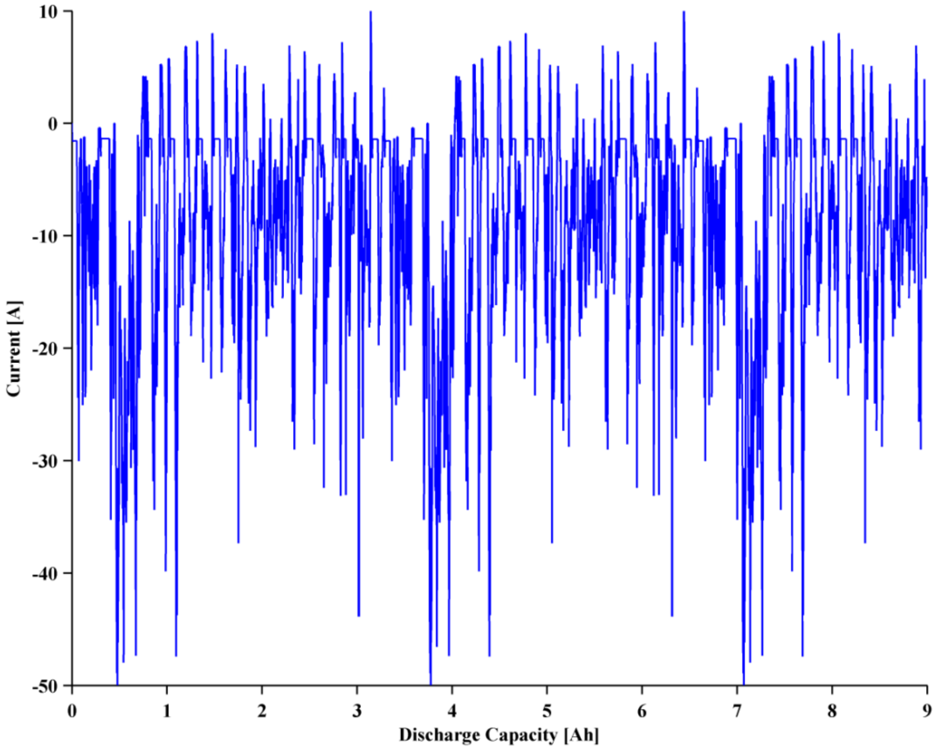
Current [A]
Discharge Capacity [Ah]
10
0
-10
-20
-30
-40
-50
0
1
2
3
4
5
6
7
8
9

(a)

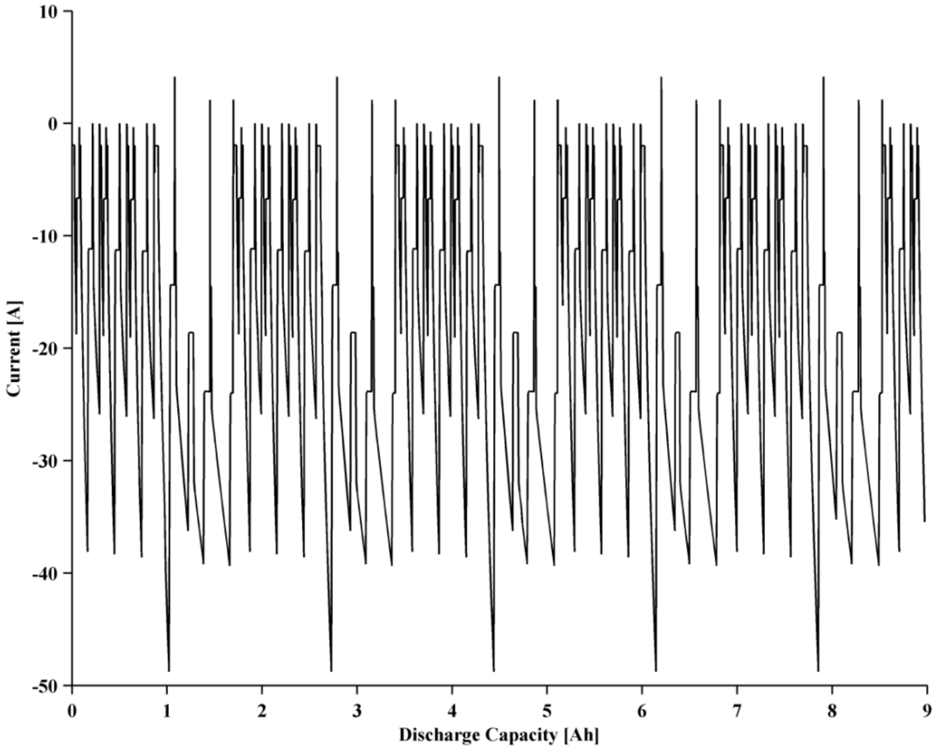
Current [A]
Discharge Capacity [Ah]
10
0
-10
-20
-30
-40
-50
0
1
2
3
4
5
6
7
8
9

(b)

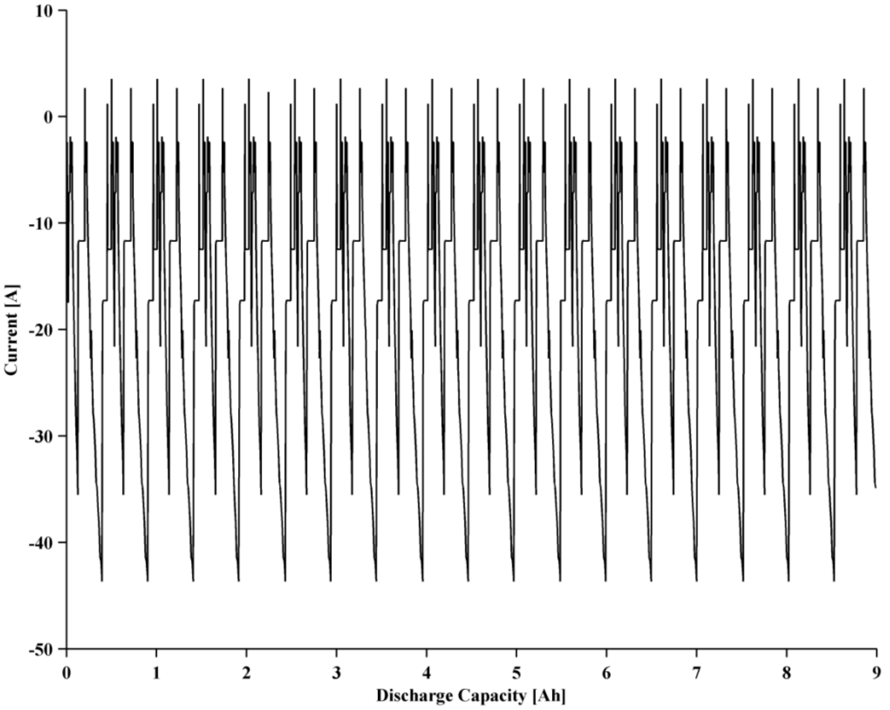

Current [A]
10
0
-10
-20
-30
-40
-50
0
1
2
3
4
5
6
7
8
9
Discharge Capacity [Ah]

(c)

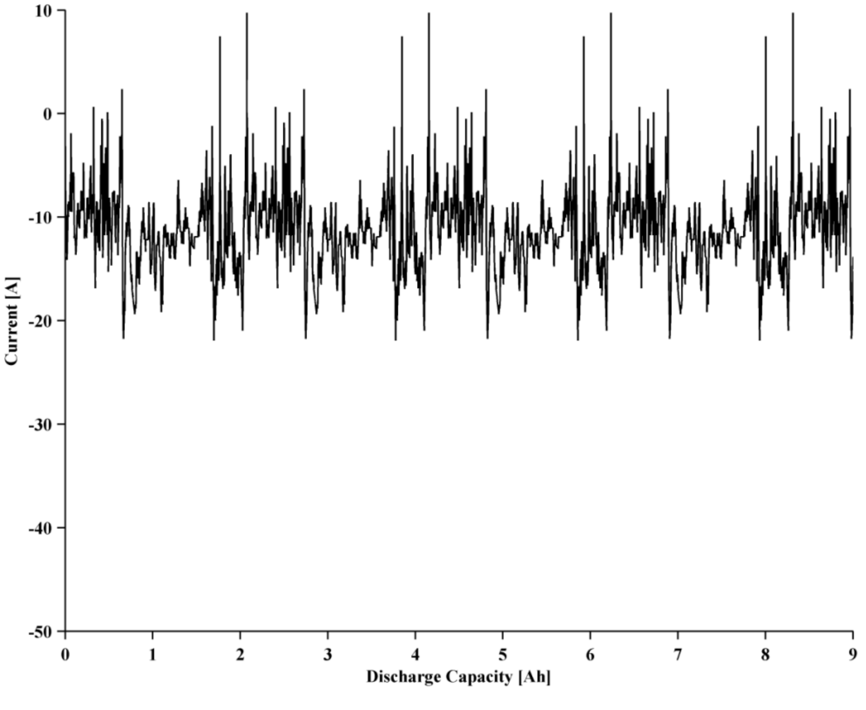

Current [A]
10
0
-10
-20
-30
-40
-50
0
1
2
3
4
5
6
7
8
9
Discharge Capacity [Ah]

(d)

Figure 4-6: Current profiles based on EV driving cycles: (a) UDDS, (b) J1015 Mode, (c) ECE and (d) FHDS

The main purpose of this study is to investigate the thermal behaviour under EV applications, so EV driving cycles from Europe, USA and Japan have been chosen to conduct the test on the battery pack. They are the European driving cycles to account for urban driving (ECE15), US driving cycles to examine the urban and highway driving cycles (UDDS and FHDS) and Japanese driving cycles to study a combination of urban and extra urban route (J1015 Mode). Their corresponding current profiles and battery pack temperature are shown in Figure 4-6 and Figure 4-7, respectively, where the battery pack is operated under repeated driving cycles until it reaches the cut-off voltage.

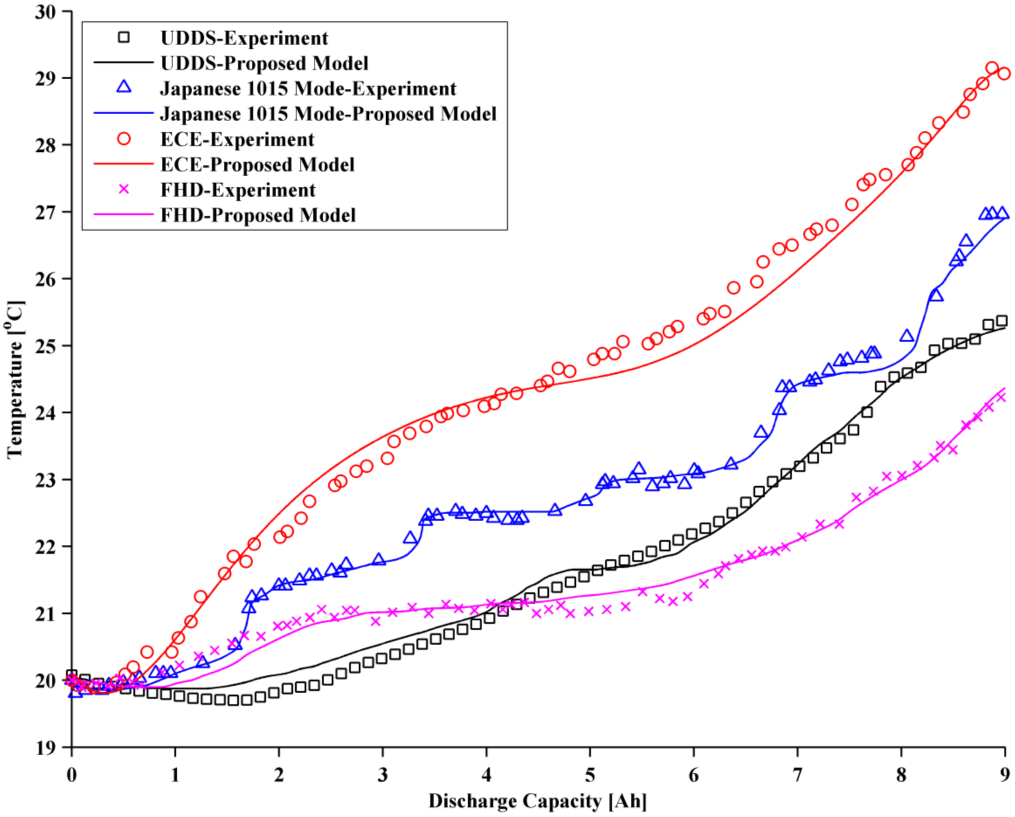

Figure 4-7: Temperature comparison for UDDS, Japanese 1015 Mode, ECE and FHD

The comparison of the battery pack temperature calculated from the thermal model with those measured from the experimental data indicates that they agree very well with the average errors of 1.34%, 1.74%, 2.13% and 1.36% in UDDS, J1015 Mode, ECE and FHD, respectively. Such low average errors prove that the proposed thermal model can accurately predict the battery pack temperature under EV driving cycles.

The maximum temperature achieved at the end of the cycle for UDDS, J1015 Mode, ECE and FHD are 25.26ºC, 26.90ºC, 29.15ºC and 24.36ºC, respectively. It is observed that the driving cycle with high charge rate (or discharge rate) more power is delivered to (or drawn from) the battery pack and consequently more heat is generated. The ECE cycle is the most aggressive driving cycle, leading to the highest temperature among the studied EV driving cycles. It is also observed that at the beginning of the transient EV driving cycles the chemical reactions are endothermic which causes a slight temperature drop, as the dynamic cycle proceeds further, the heat generated from the source terms contributes to the rise of the temperature. Figure 4-8 demonstrates the temperature changes and voltage changes at UDDS cycle for all the Li-ion battery cells in the 4P4S battery pack.

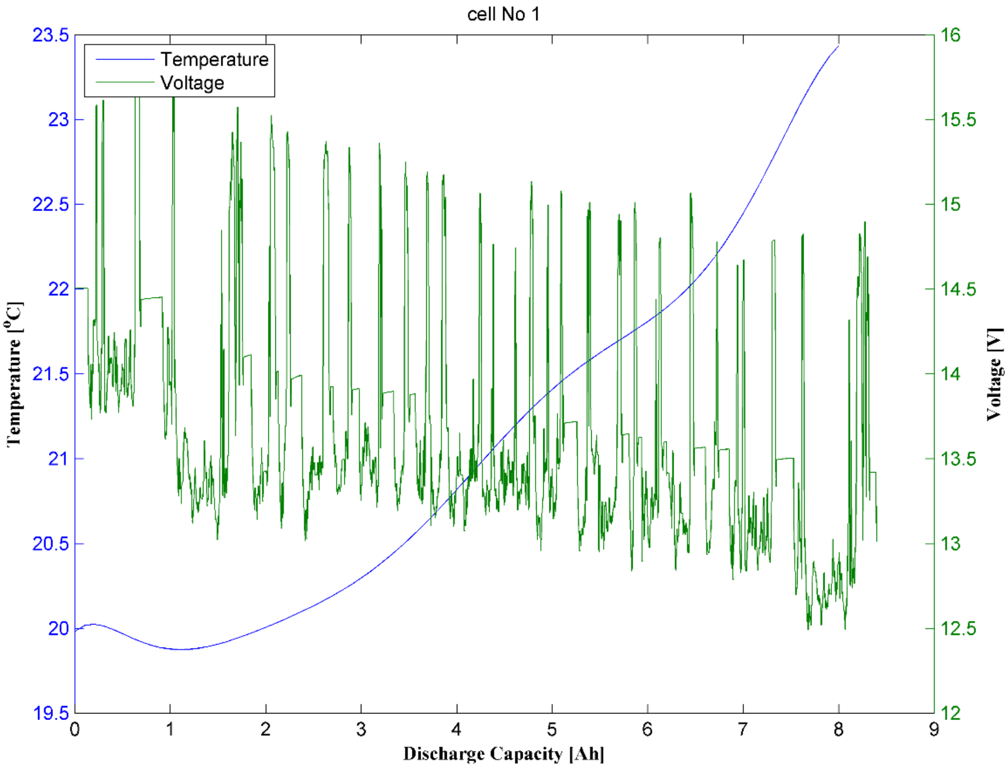

(a) Cell 1

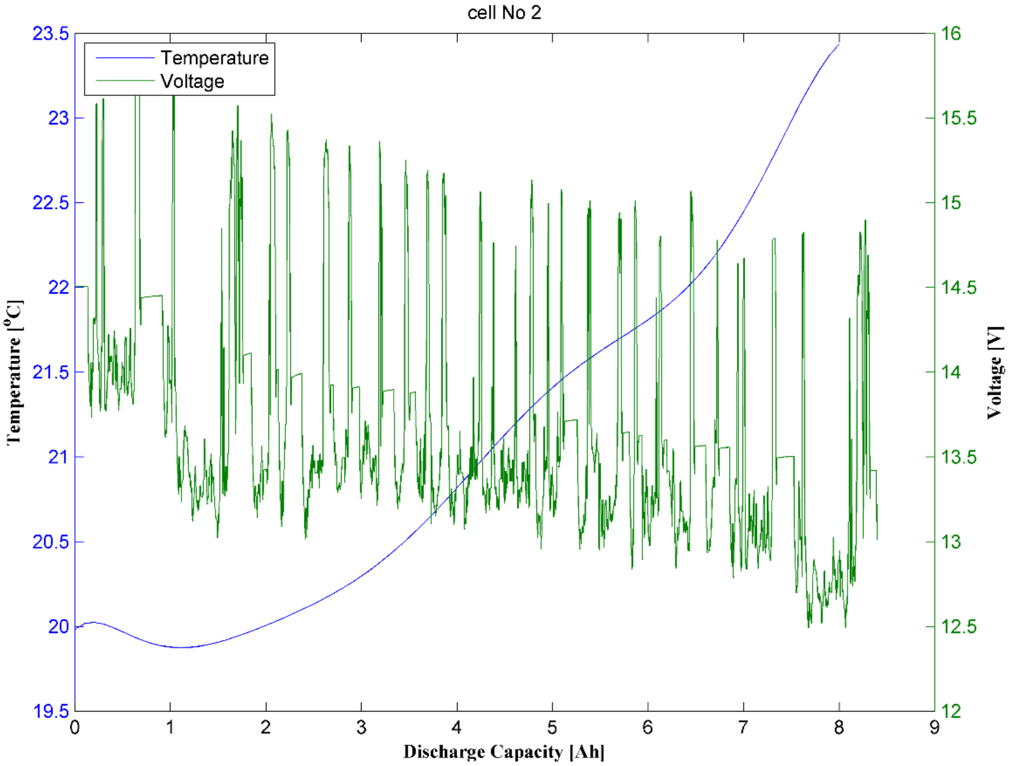

(b) Cell 2

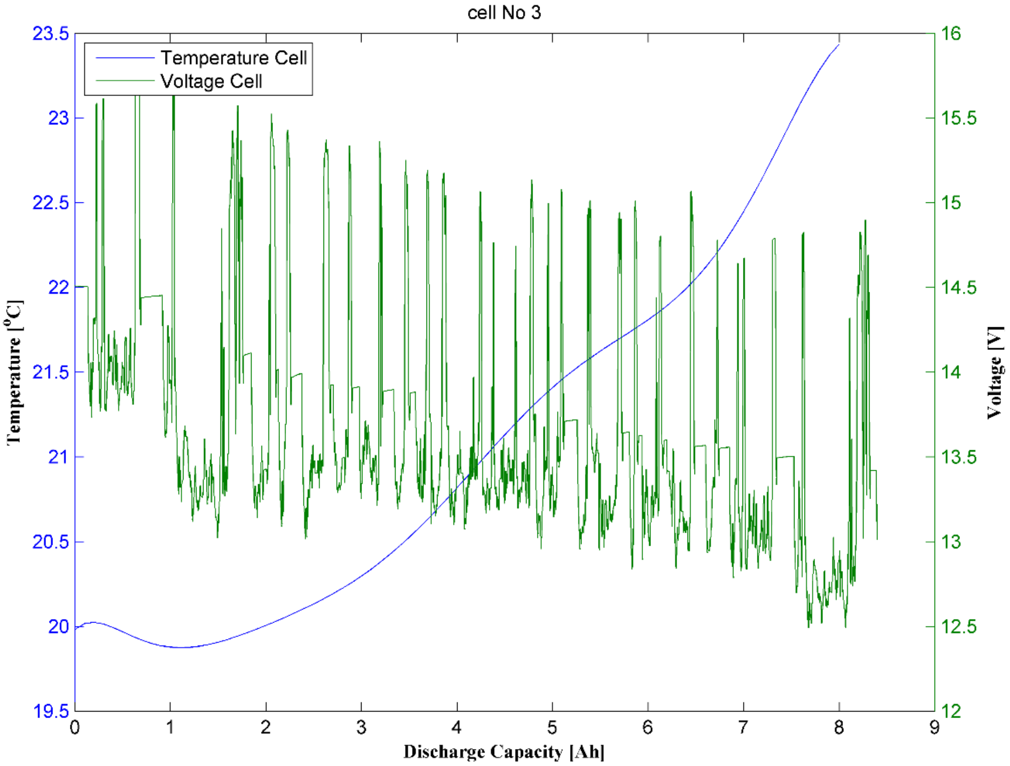

(c) Cell 3

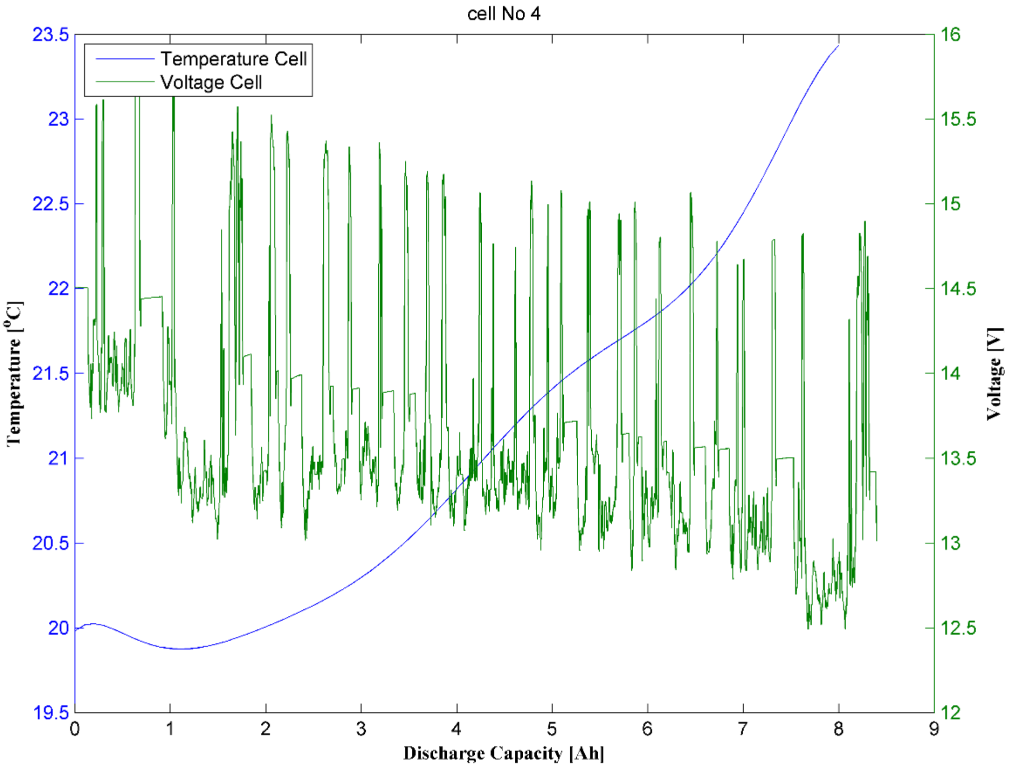

(d) Cell 4

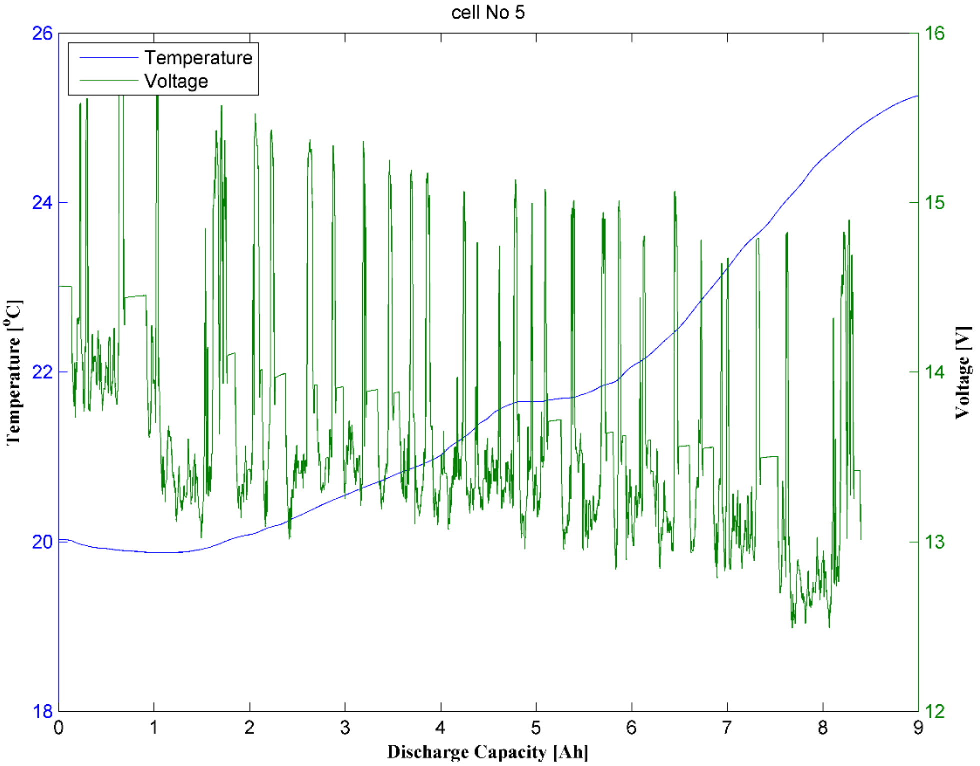

(e) Cell 5

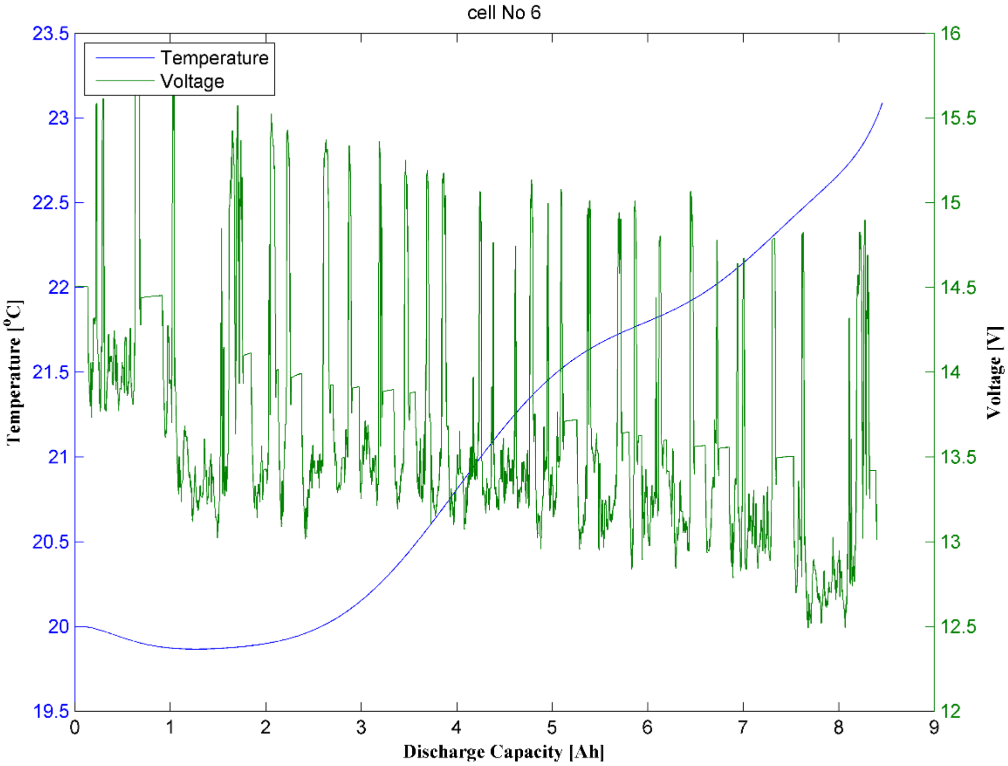

(e) Cell 6

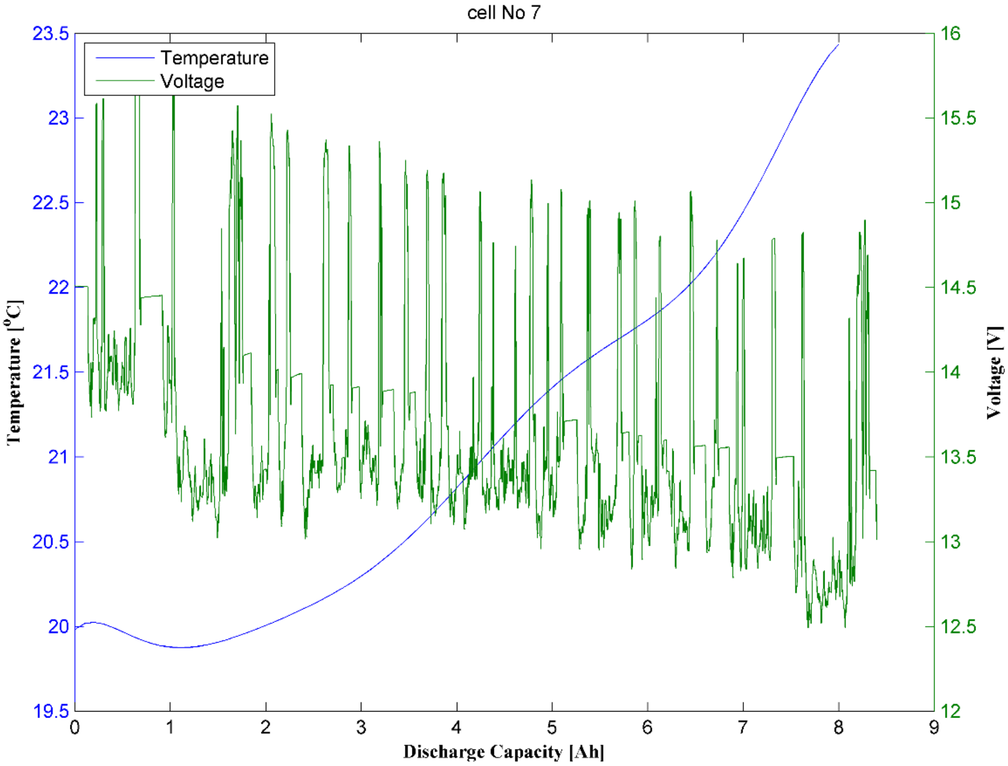

(f) Cell 7

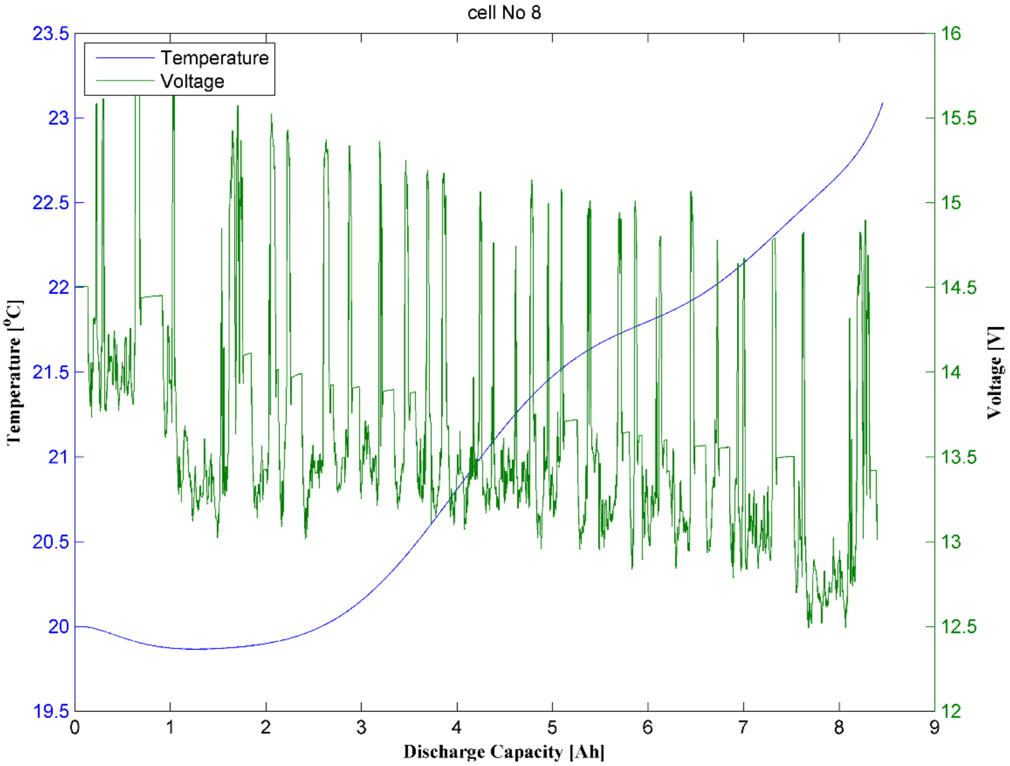

(g) Cell 8

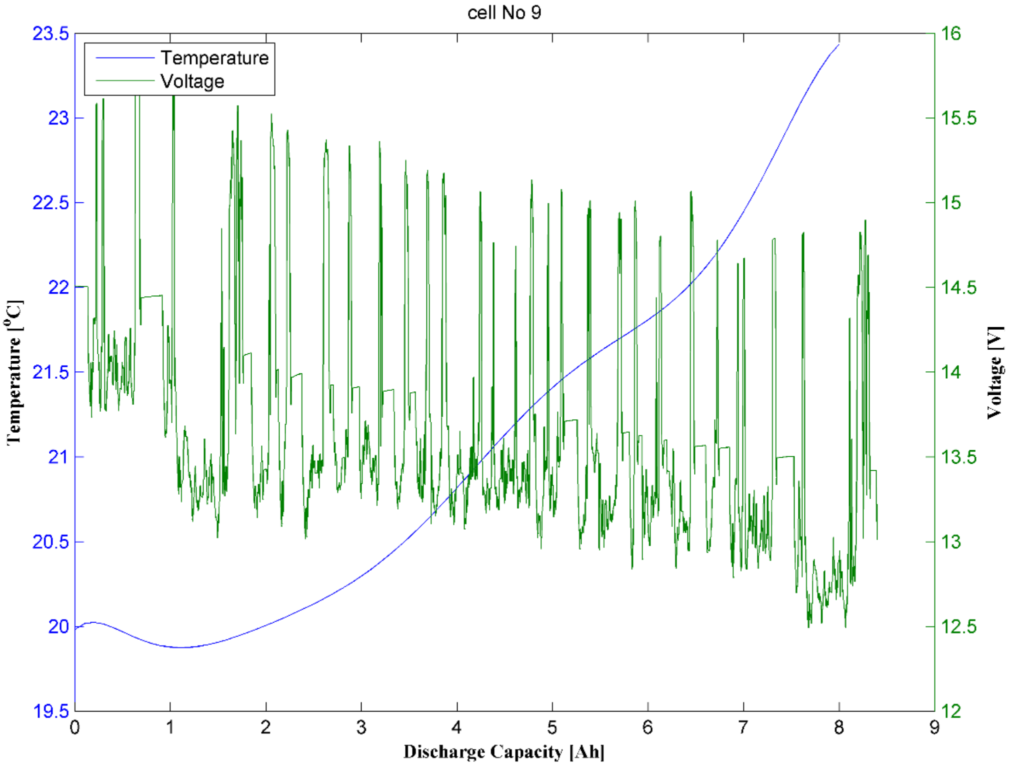

(h) Cell 9

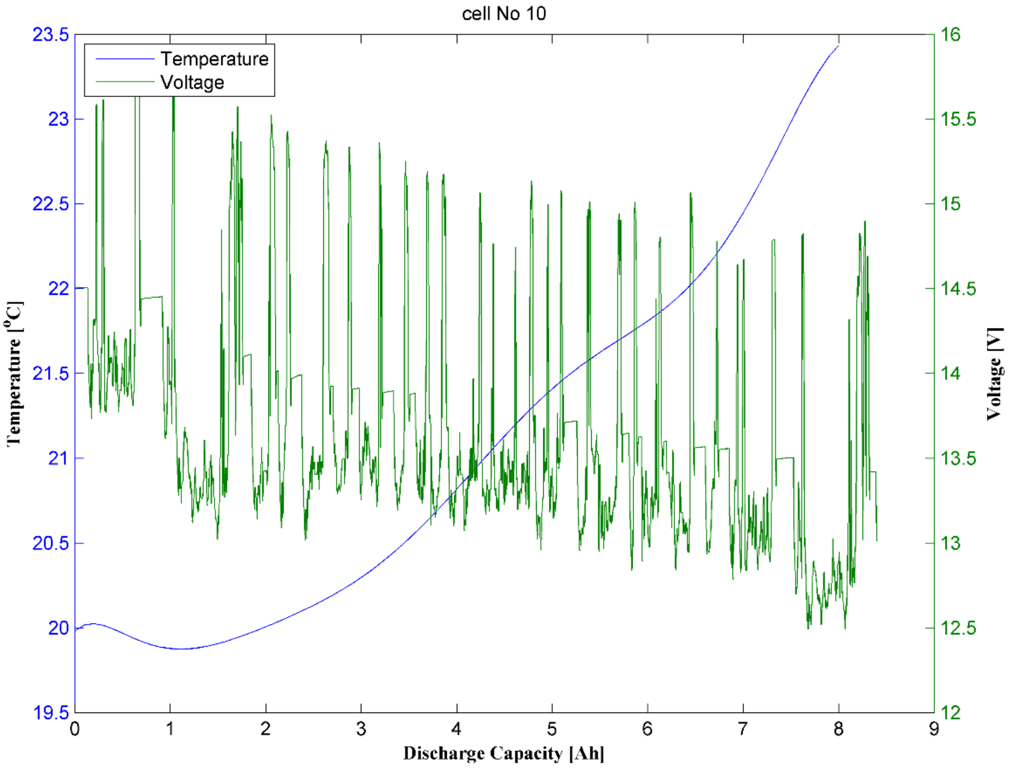

(i) Cell 10

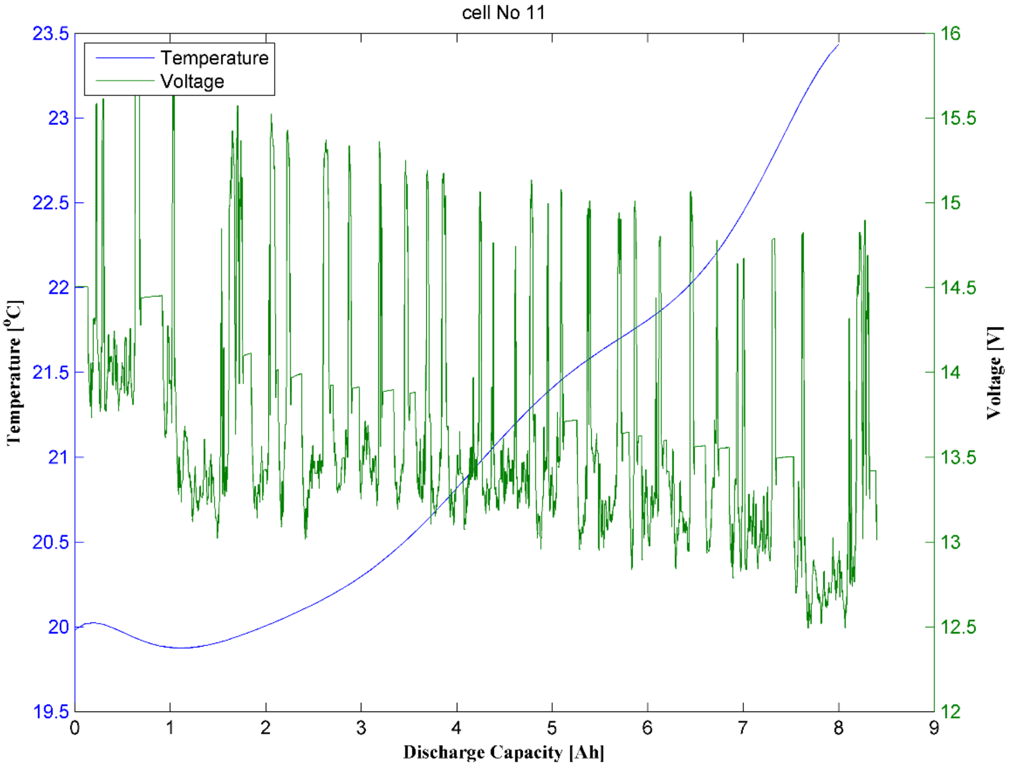

(j) Cell 11

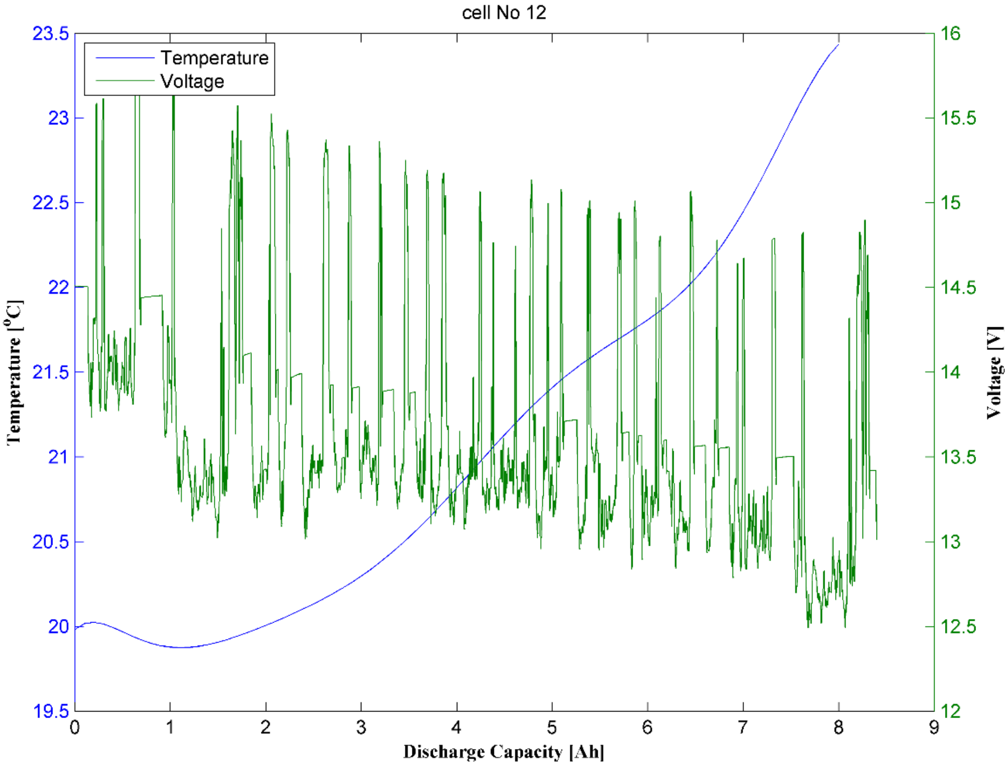

(k) Cell 12

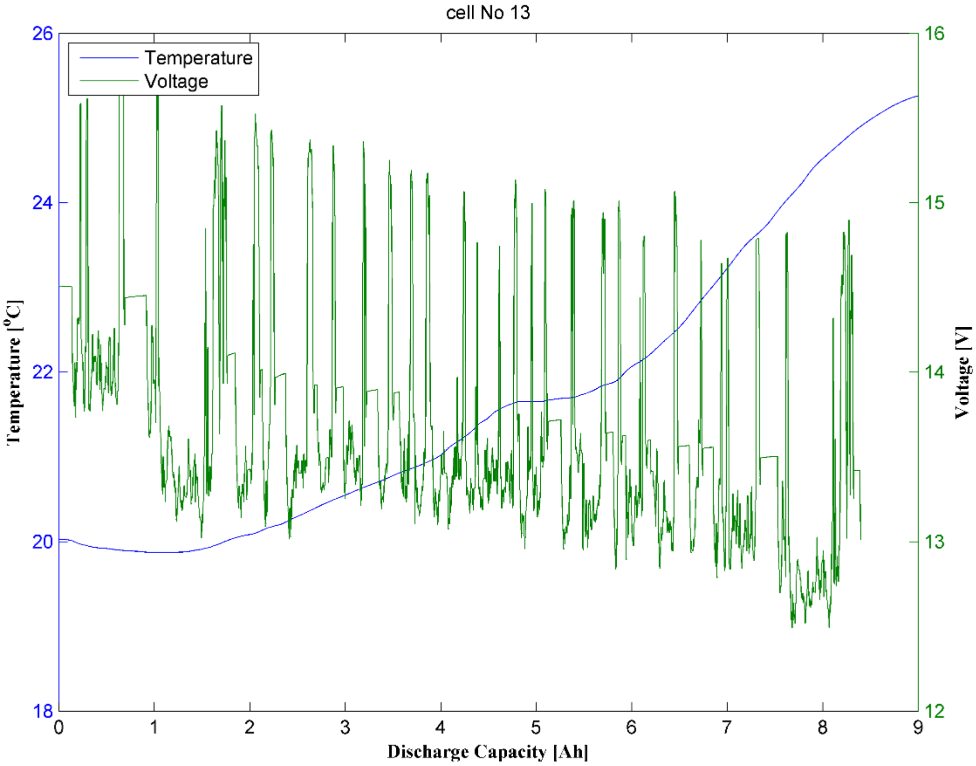

(l) Cell 13

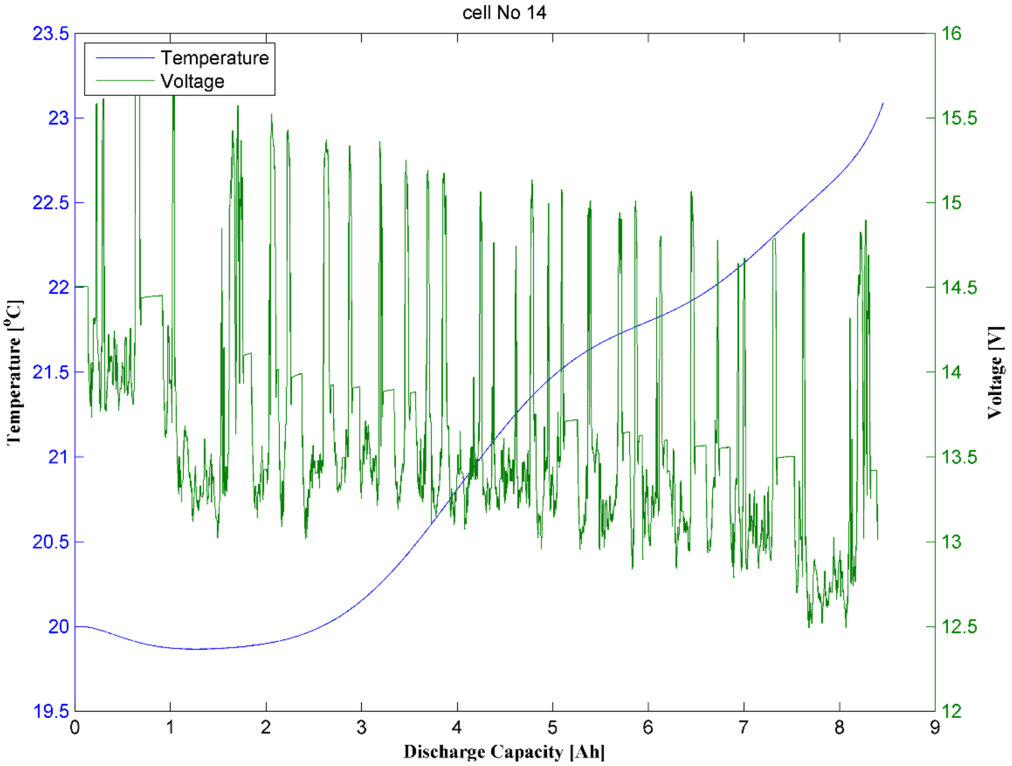

(m)Cell 14

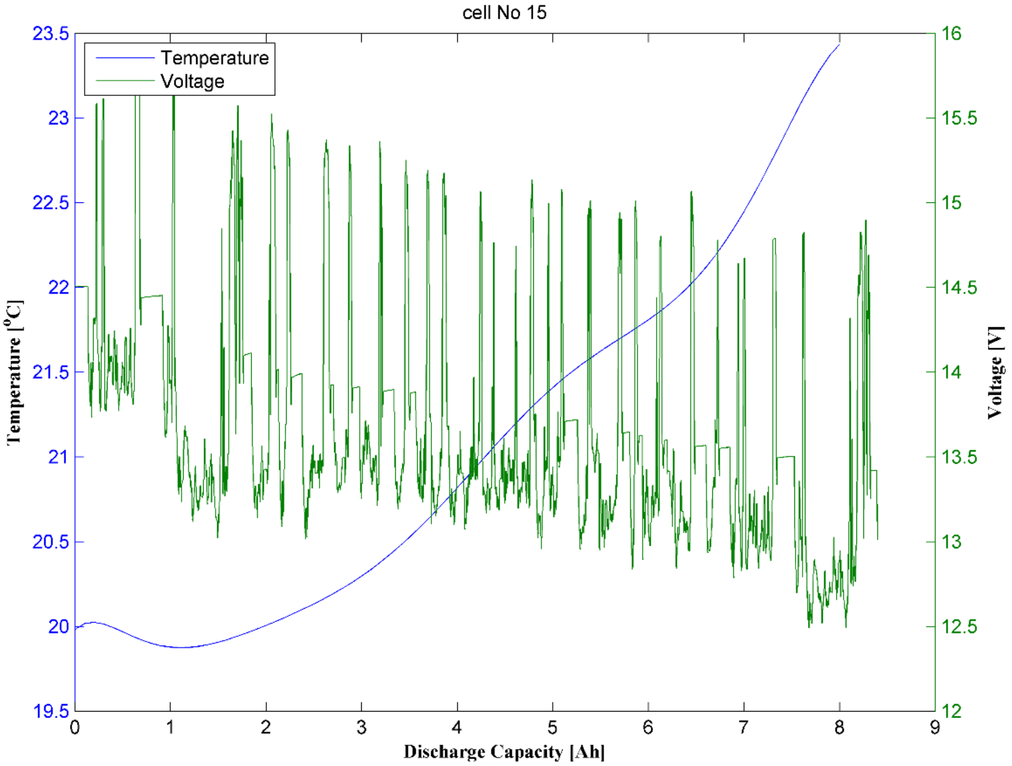

(n) Cell 15

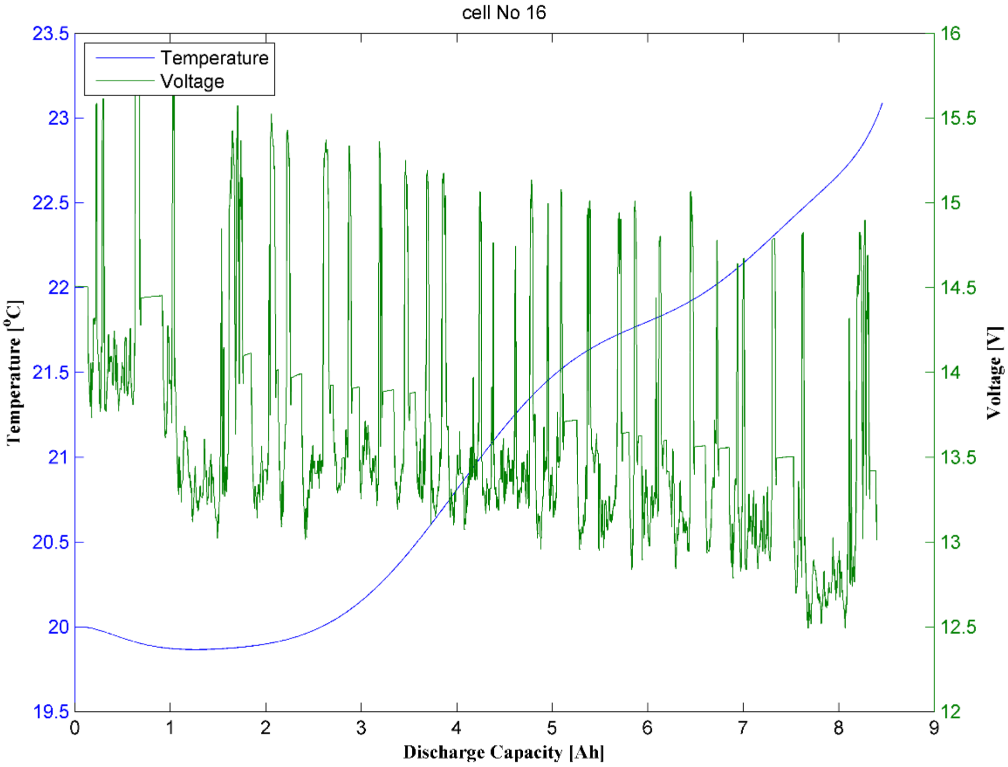

(o) Cell 16

Figure 4-8: Temperature changes and voltage changes at UDDS cycle for all the Li-ion battery cells in the 4P4S battery pack.

4-4-2 Battery pack with fan

To study the effect of fan on the temperature response of the battery pack, a 12V DC fan with the maximum air flow of 5.4 cubic feet per minute (CFM) is used in the experiments, where three air flow rates are considered: the maximum flow rate (5.4 CFM), the medium flow rate (2.1 CFM) and zero flow rate which are obtained by using variable power supply and measured by an oscilloscope as shown in Figure 4-9.

The thermal responses of the battery pack under the UDDS for three above-mentioned flow rates are provided in Figure 4-9, respectively. It can be observed that by using the maximum and medium fan flow rates, the battery pack temperature at the end of the cycle is increased by only 2.15°C and 3.40°C, respectively, while with the zero flow rate, namely the fan is not running, the temperature goes as high as 5.26°C.

It should be noted that the higher the air flow rate, the higher the power consumption and the slower the temperature rise. The power consumption for the high flow rate is 0.96W while it for the medium flow rate is 0.36W. In our case, from high flow rate to medium flow rate there is the power reduction by 0.6W which causes the temperature rise by 1.25°C. Therefore, a careful consideration is required to select the proper fan air flow rate since the power consumption of the fan will draw from the battery pack in EVs.

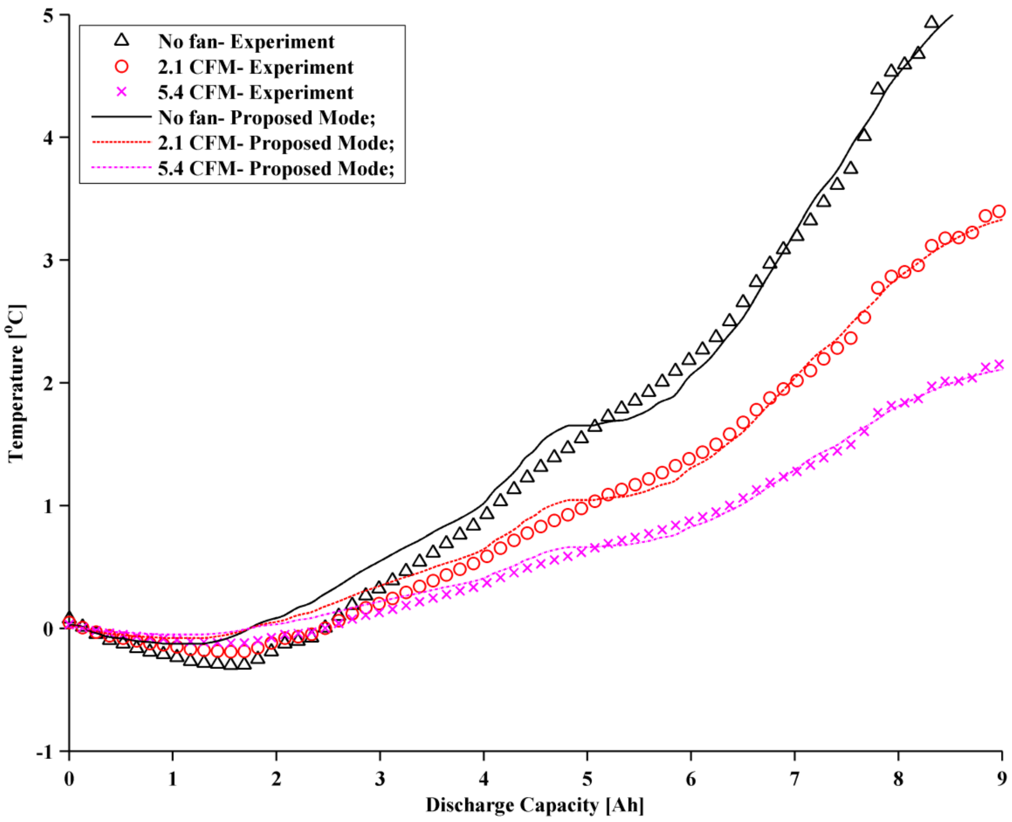

Figure 4-9: Comparison of change in temperature under UDDS at different flow rates of fan

4-4 Results and discussions

4-4-1 Heat analysis of UDDS

The detailed heat analysis of the battery pack under UDDS has been carried out and the results are shown in Figure 4-10. It can be observed from the Figure 4-10 that as the temperature of the battery pack decreases at the beginning of the cycle no heat dissipation occurs because the heat dissipation by conduction is proportional to the temperature difference between the casing and the cell as expressed by Eq. (4-8). As UDDS proceeds further, when the battery pack discharges by 1.3Ah the temperature difference between the casing and the cell starts to increases, this difference becomes almost constant at a certain temperature. As a result, the heat conduction initially increases and then becomes almost constant.

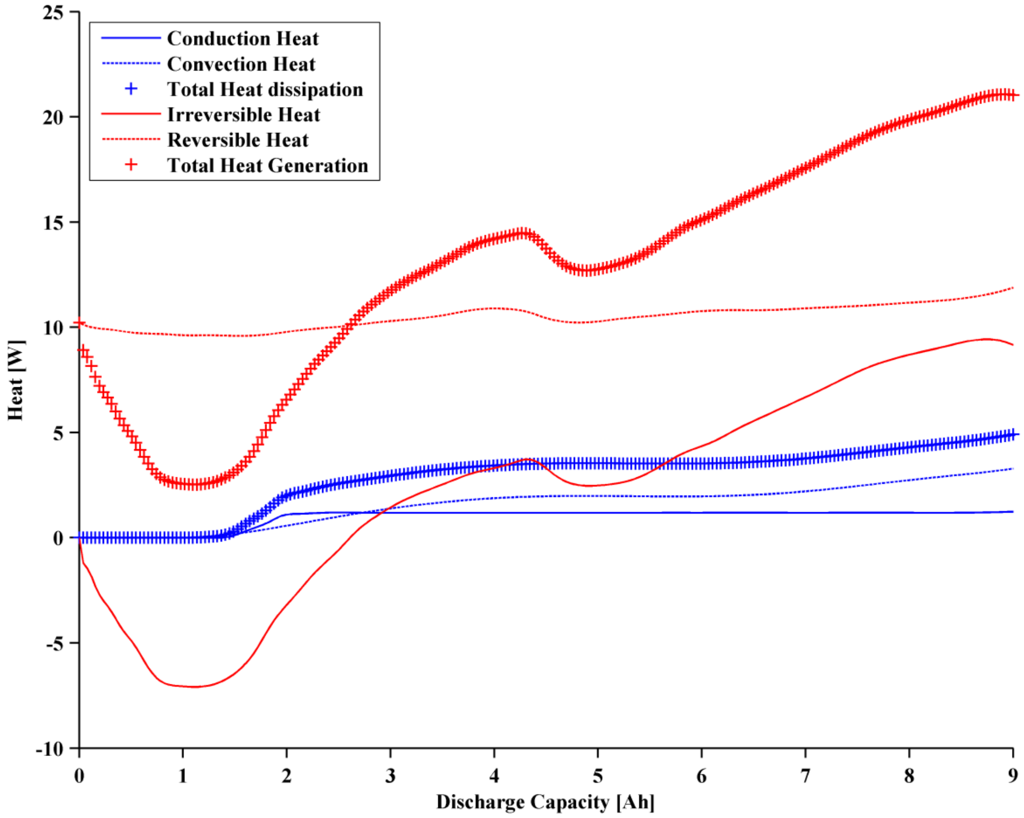

Figure 4-10: Heat analysis of lithium ion battery pack under UDDS

The heat dissipation through convection is proportional to the temperature difference between the surroundings and the battery pack as expected in Eq.(4-5). Hence, the heat dissipation rate increases towards the end of the cycle. According to Eq. (4-2), reversible heat is affected by the distribution of reaction current density as well as the variation of the entropy term (dU/dT). The reaction current density in the UDDS varies with the charge and discharge current density along the time while the entropy fluctuates with the state of the battery pack.

The almost constant reversible heat proves that the effects of current density and the entropy may cancel each other. The irreversible heat drops at the beginning of the cycle due to the endothermic chemical reaction and after a while starts to increase when the Joule heat becomes dominant. The total heat generation of the battery pack decreases at the beginning of the cycle and then increases towards the end of the UDDS, resulting in the rise of battery pack temperature.

4-4-2 Effect of thermal resistive network on accuracy of temperature prediction

In the proposed model, the theoretical electrochemical thermal model coupled with the thermal resistive network model to improve the accuracy of the temperature prediction. Again, the UDDS is selected as an example. Figure 4-11 shows the comparison of the temperature prediction between the experimental data and the proposed model with and without the thermal resistive network model.

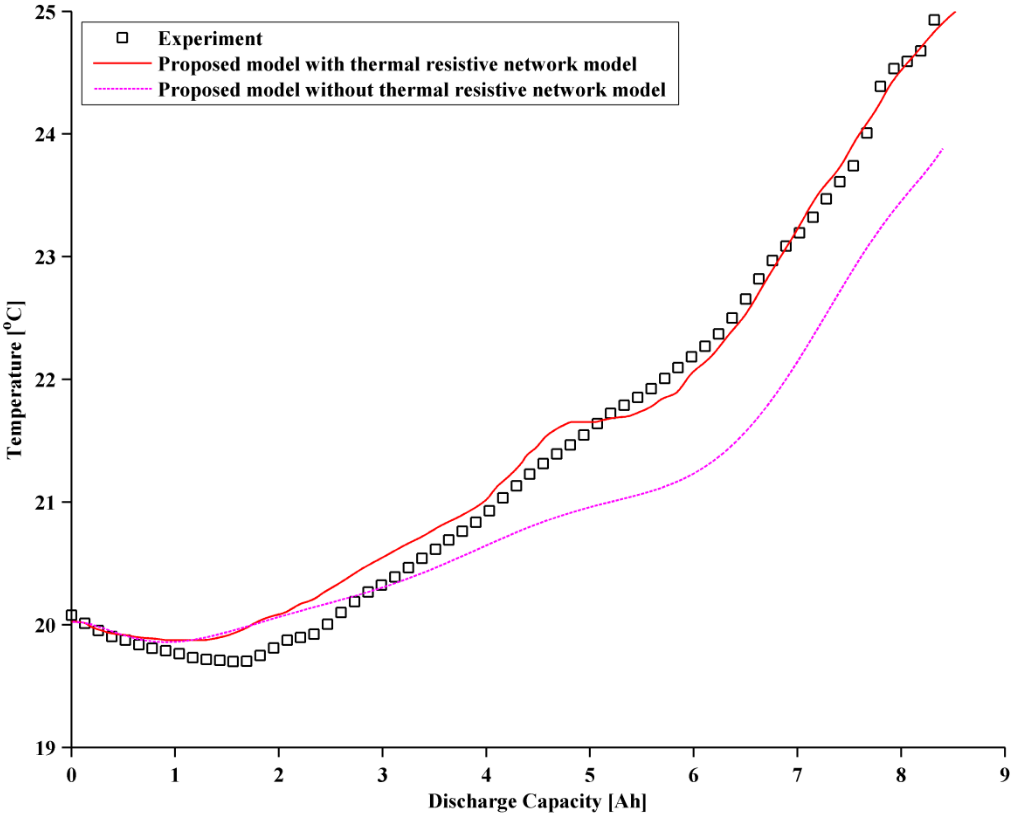

Figure 4-11: Comparison of temperature predicted from proposed model with and without thermal resistive network under UDDS with temperature obtained from experimental data

It can be seen that the temperature profiles for the proposed model with and without the thermal resistive network match the temperature profile from the experimental data very well at the beginning of the cycle since there is no heat conduction. After the battery pack discharges by 2Ah, the discrepancies between two profiles begin. Comparing with the temperature profile from the experimental data, the proposed model with and without the thermal resistive network model has the average errors of 1.34% and 3.45%, respectively. This improves the accuracy of temperature prediction by 2.6, which is important for EV applications.

4-4-3 Battery pack at different ambient temperatures

In the previous experiments, the battery pack is placed under the controlled ambient temperature of 20 ºC. To be more realistic for EV applications, a large battery pack which consists of four above-mentioned battery packs is built with all of them connected in series (shown in Figure 4-12). It has the total voltage of 56.8V. This large battery pack is simulated under the UDDS in the presence of the ambient temperature of 30ºC and 40ºC.

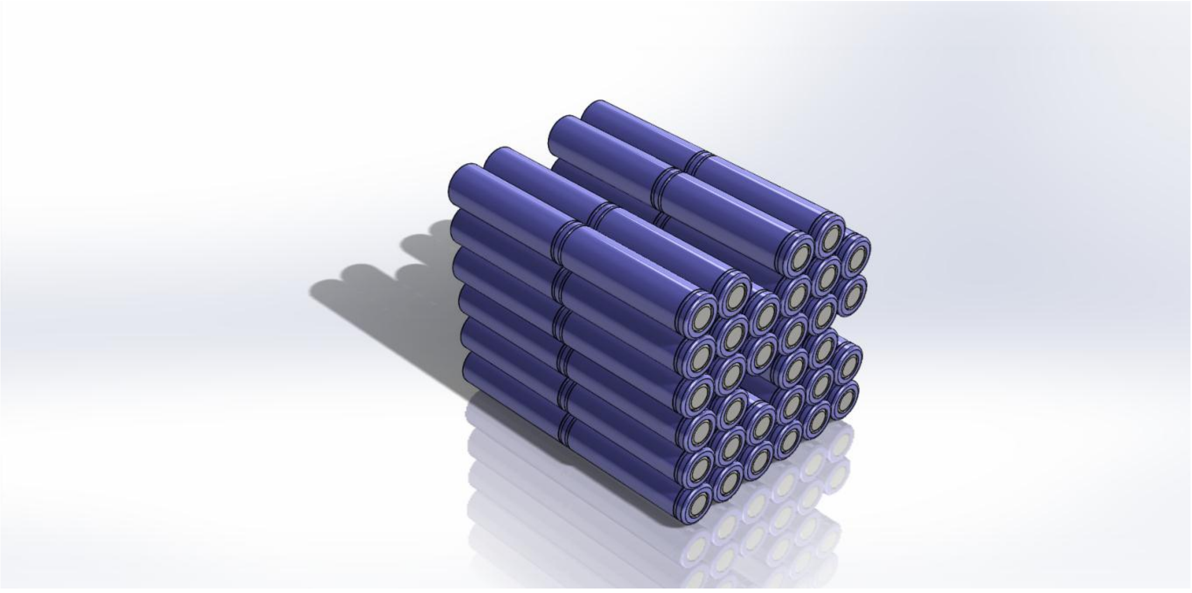

Figure 4-12: Illustration of four of battery pack connected in series

The results of the highest cell temperature are shown in Figure 4-13. It can be seen that at the ambient temperature of 20ºC, 30ºC and 40ºC, the temperatures of the large battery pack can finally increase to 38.47ºC, 49.58ºC and 60.34ºC, respectively. It shows that the battery pack will not be in the safe thermal range for the ambient temperature of 30ºC and 40ºC. The temperature behaviour of the large battery pack under the forced convection is also simulated in the presence of the ambient temperatures of 20ºC, 30ºC and 40ºC, where the fans are the same as that in Section 4-3 with the high flow rate of 5.4CFM. The temperatures of the large battery packs are 27.69ºC, 38.93ºC and 49.01ºC, respectively.

In the developed thermal model proposed in this thesis, all the temperature dependent parameters have been considered. Some parameters like diffusivity coefficient are highly thermal dependent and have significant changes as temperature changes to more than 30ºC and below than 10°C. Considering all the thermal dependent parameters, the temperature will rise at the ambient temperature more than 30°C and below than 10°C.”

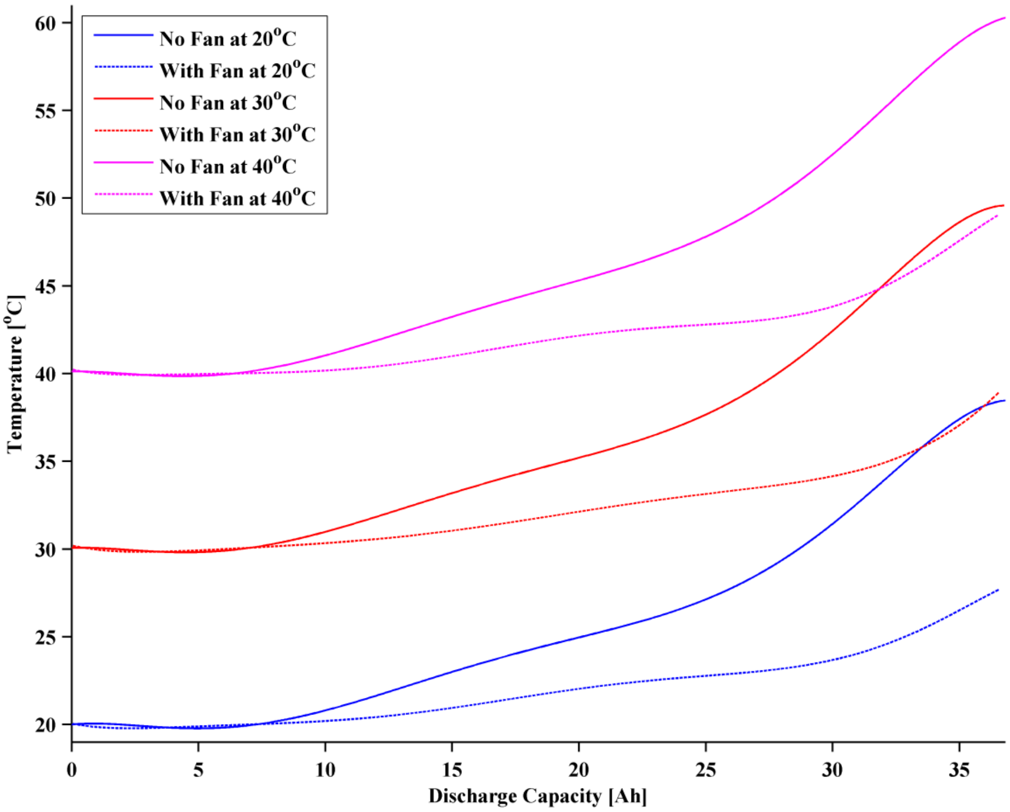

Figure 4-13: Temperature profiles for large battery pack at different ambient temperatures

4-5 Summary

An improved theoretical electrochemical-thermal model combined with the thermal resistive network is used to predict the thermal performance of the Li-ion battery packs in EVs. The combined model is used to study heat generation and heat dissipation as well as their influences on the temperatures of the battery pack with and without a fan under constant current discharge and variable current discharge based on EV driving cycles. The temperatures simulated from the proposed model are compared with the temperatures obtained from the experimental data to verify the accuracy of the proposed model.

Furthermore, the proposed model with and without the fan has also been investigated. It shows that the use of the fan can decrease the temperature of the battery pack but consume the power from the battery pack. Therefore, for battery pack design in EVs the power consumption of the fan together with the temperature rise should be considered.

The simulation of the large battery pack at high ambient temperatures (e.g. 30°C or 40°C) shows the final temperature of the large battery pack can exceed the safe thermal range. Therefore, the thermal management system is important for EVs to ensure that all cells in the battery pack are operating within the safe temperature range.

Chapter 5 Performances of Li-ion batteries at low temperatures

5-1 Introduction

Rechargeable lithium-ion (Li-ion) batteries have been chosen as the leading candidate in commercial electric vehicles (EVs) due to their high energy and power density compared to other battery chemistries. However, successful adoption of EVs must overcome the technical limitations of Li-ion batteries. One limitation is the significant reduction in energy and power densities at low temperatures, particularly below $0\,^{o}C$ [86, 98, 139]. It has been reported that typical commercial Li-ion batteries only retain 5% of energy density and 1.25% of power density at $-40^{o}C$ compared to the respective values at $20\,^{o}C$ [86]. Thus, it is necessary to understand the limiting factors of Li-ion cells and battery packs at low temperatures to ensure EV performance is adequate [87, 92, 101, 140-142].

In this chapter, the behaviour of a laboratory-made cell and pack at low temperatures under wide range of discharge conditions is investigated. These include constant discharge currents and discharge profiles based on EV driving cycles. The thermal dependent parameters are constructed in electrochemical-thermal models. The results obtained from the models and those from the experiments are compared to show that the models developed can reliably predict Li-ion cell and pack performance at low temperatures. A simulation was also conducted in the validated model to provide an insight into the Li-ion cell and pack and identify the limiting factors of the poor performance at low temperatures.

5-2 Overpotentials

When a battery is discharged, it needs to overcome overpotentials caused by physical and chemical changes in the properties of the material that make up the electrodes and electrolytes inside a battery for delivering energy to a load. Overpotentials are divided into three parts [23, 24]: the Ohmic overpotential η_{ohm}, the kinetic overpotential η_k and the concentration overpotential η_c. At low temperatures, overpotentials may become dominant factors influencing battery performances.

The Ohmic overpotential can be expressed as an integral from the cathode to the anode:

$$\eta_{ohm} = \frac{iA(0)}{\kappa}\int_0^L \frac{dx}{A(x)} \tag{5-1}$$

Here, $A(x)$ is the area of the cross section at distance x from the negative electrode.

The kinetic overpotentials to describe oxidation reaction in the anode and reduction reaction in the cathode are respectively shown as follows:

$$\eta_{k,a} = \frac{RT}{\alpha_a F} ln \frac{i}{i_{0,a}} \tag{5-2}$$

$$\eta_{k,c} = -\frac{RT}{\alpha_c F} ln \frac{i}{-i_{0,c}} \tag{5-3}$$

The concentration overpotential is caused by the concentration variations near the surface of the electrode particles and electrolyte. In solutions with an excess of supporting electrolytes, it can be approximated as:

$$\eta_c = \frac{RT}{nF} ln \frac{c_e}{c_s} \tag{5-4}$$

5-3 Model validation

The battery cell used in this study was a laboratory-made Li-ion pouch cell with the normal capacity of 3.6Ah. The cells consist of NCM ($LiNi_{1/3}Mn_{1/3}Co_{1/3}O_2$) cathode and graphite (Li_xC_6) anode. The electrolyte of the cell is a solution of $LiPF_6$ salt with propylene carbonate (10%), ethylene carbonate (27%) and dimethyl carbonate (63%) in volume.

It should be mentioned that the coating length is 50*cm* and the weight is 44*g* per cell. The cell structure squeezes the electrode into a small cell volume in which temperature difference is small. These features of pouch cells allow a reasonable assumption of uniform reaction rate and temperature distribution.

The anode consists of 95.5% graphite, 1.5% Super P carbon black and 3% PVDF (by weight), with anode thickness of 80μm. The cathode compositions are generally 94% NCM, 3% Super P carbon black and 3% PVDF. Thickness of this cathode is 78μm. The cell has an N/P (negative to positive electrode) ratio of 1.15 and electrode coating area of 640 cm^2. Active material loading in the cathode is 3.9mAh/cm^2. Using material balance, the porosities of anode and cathode are calculated as 0.26 and 0.28 respectively. Separator of 20μm thickness and 0.46 porosity is used. The electrolyte is 1.2 *M* $LiPF_6$ in a mixture of PC, EC and DMC (10:27:63 by volume).

To minimize the cell differences induced during fabrication process and formation cycles, two cells are selected to operate at the same condition. A consistency check of the cell data is performed and only one cell data will be presented.

Model validation of a single cell and battery pack was conducted under different ambient temperatures and a wide range of constant discharge currents and variable discharge profiles based on EV driving cycles. The Li-ion cell and pack used in the validation are shown in Figure 5-1, where the pack was constructed from four Li-ion cells in series.

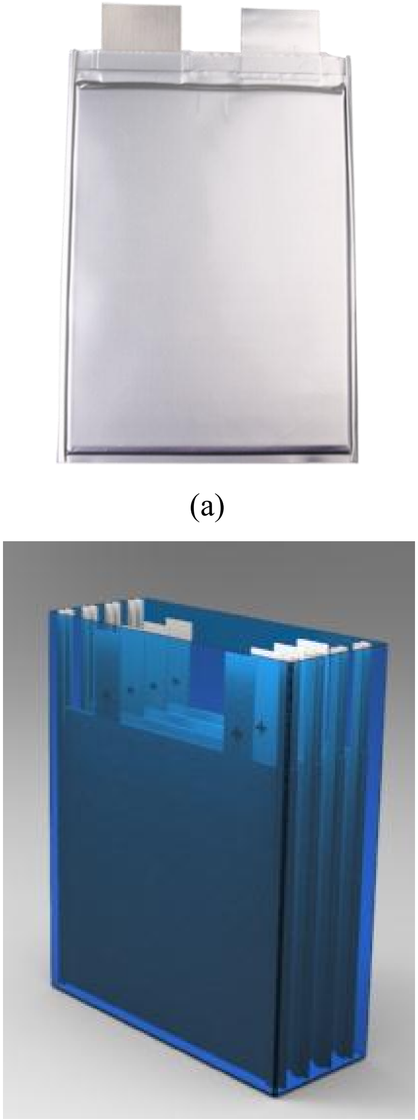

(a)

(b)

Figure 5-1: Li-ion (a) cell, (b) battery pack

For the experiments, the cell and the pack were charged at room temperature by constant current constant voltage (CCCV) with the CC of 0.5C followed by the CV of 4.2V. At the CV stage, when the charging current was decreased to 0.05C, both the cell and the pack were considered to be fully charged and the charging process was terminated. A temperature chamber was used to provide different ambient temperatures for all discharging tests. A thermocouple was used to measure the cell surface temperature located midway along the length of the Li-ion cell. In order for the cells to reach thermal equilibrium before each charge and discharge operation, the cells were kept at four-hour rest at each ambient thermal point set by the temperature chamber, except room temperature, where only a one-hour rest was applied.

5-3-1 Single cell

Experimental results of voltages and temperatures for the single Li-ion cell were compared with the simulation results predicted from the model at the constant discharge rates of 0.2C, 0.5C, 1C and 2C at room temperature (around 20°C). These are shown in Figure 5-2. The cell voltages and temperatures which increased as a function of the discharge capacity were very consistent with an average error of 0.025% and 0.046%,

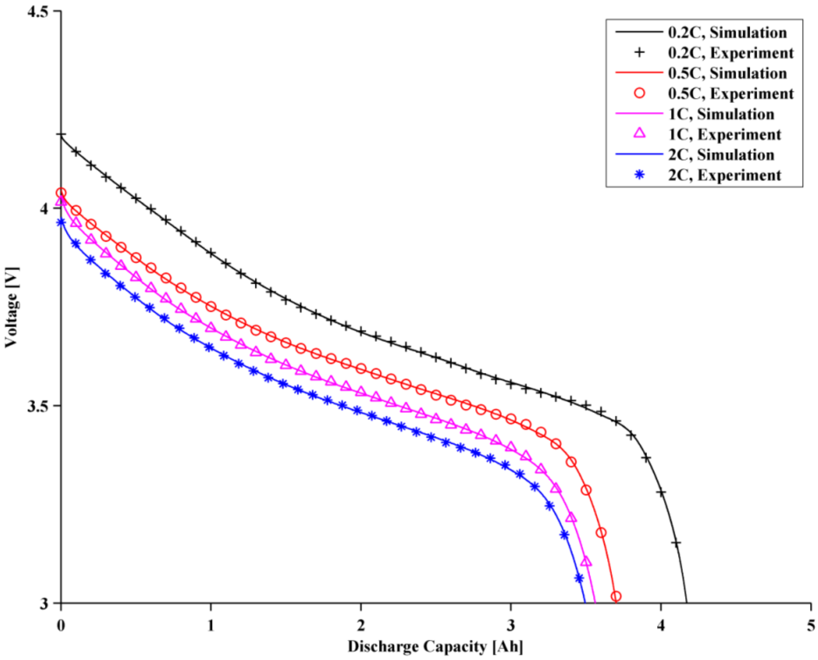

(a)

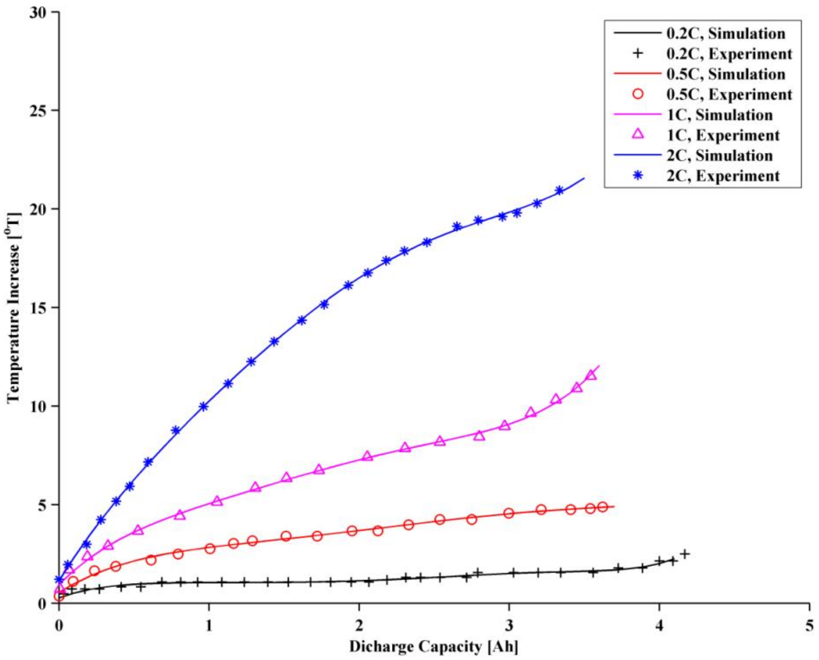

(b)

Figure 5-2: Comparison between simulation results and experimental data at different discharge rates with room temperature for a single Li-ion cell (a) voltage, (b) temperature

respectively. At the high discharge rates of 0.5C, 1C and 2C, the temperature increased significantly at the end of discharge (e.g., 12°C for 1C and 21°C for 2C) owing to the large amount of heat generated from high voltage loss.

Moreover, the Li-ion cell was validated by experiments to determine temperature and discharge rate effects on the cell, shown in Figure 5-3. To examine the temperature effect, the Li-ion cell was discharged at 1C at different temperatures of 20°C, 0°C and -10°C. The results are shown in Figure 5-3(a). The voltages of the cell calculated from the model and those obtained from the experiments showed agreement with the overall average voltage error of 4.31%, except the large voltage discrepancies near the cut-off at the subzero temperature of -10°C. Both cell voltage and capacity decreased with temperature reduction due to high-cell resistance and a large voltage drop at lower temperatures.

Affects on discharge rates at the subzero temperatures were specifically examined. A temperature of -10°C was selected since the cell at this temperature is still capable of delivering reasonable performance at high discharge rates usually occurring in EV applications. The Li-ion cell was discharged at currents of 2C, 1C, 0.5C and 0.2C at -10°C. As shown in Figure 5-3(b), the model prediction matches well with the experimental data at 0.2C and 0.5C discharge rates except that the voltages are slightly over-predicted bythe model near the cut-off point. At the high discharge rates of 1C and 2C, a large voltage over-prediction by the model developed after 0.5Ah and 0.25Ah, respectively. The overall average voltage errors at 0.2C, 0.5C, 1C and 2C were 8.12%, 9.55%, 15.65% and 19.81%, respectively. Overall, the model predicted higher capacity than the experiment at -10°C.

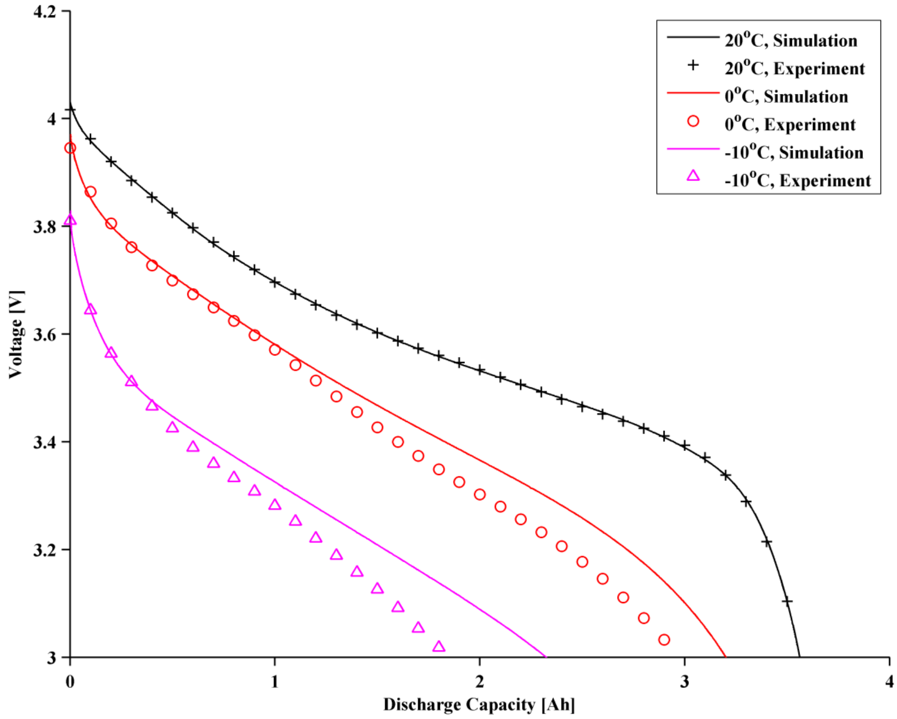

(a)

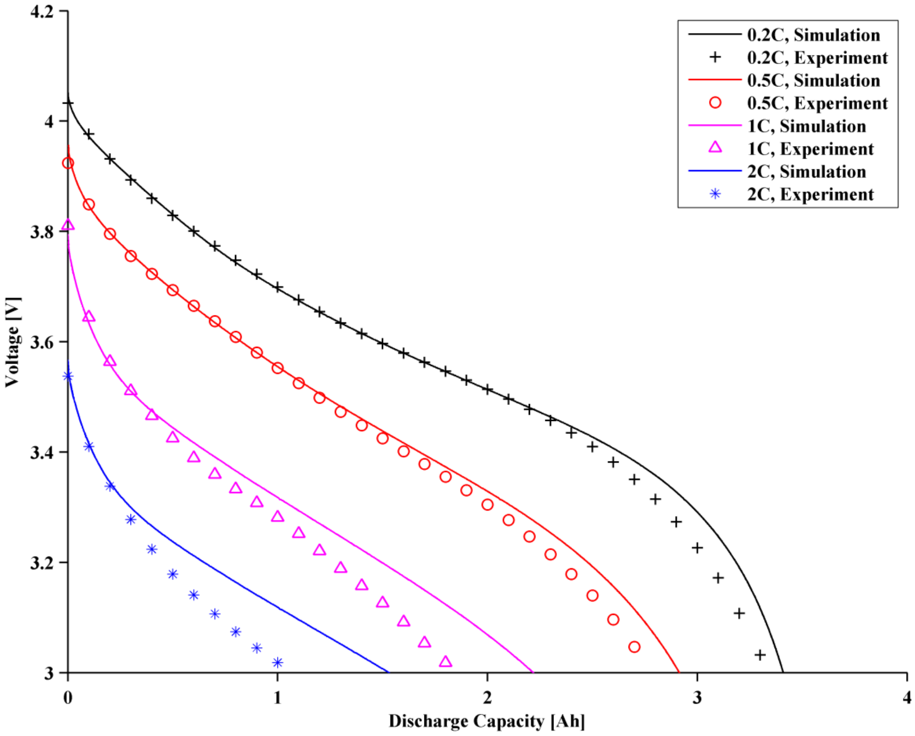

(b)

Figure 5-3: Cell voltage profile comparison between simulation results and experimental data at (a) different temperatures, (b) different discharge rates

5-3-2 Battery pack

Four of the same cells used in the previous section were connected in series to build a battery pack. The model validation of the battery pack at the constant discharge rates of 0.2C, 0.5C, 1C and 2C was carried out at room temperature (20ºC). The cut-off voltage for the battery pack was set to 12.5V. Figure 5-4 shows voltage from the model simulation compared with the experiments; they are very consistent with an overall discrepancy error of 0.09%.

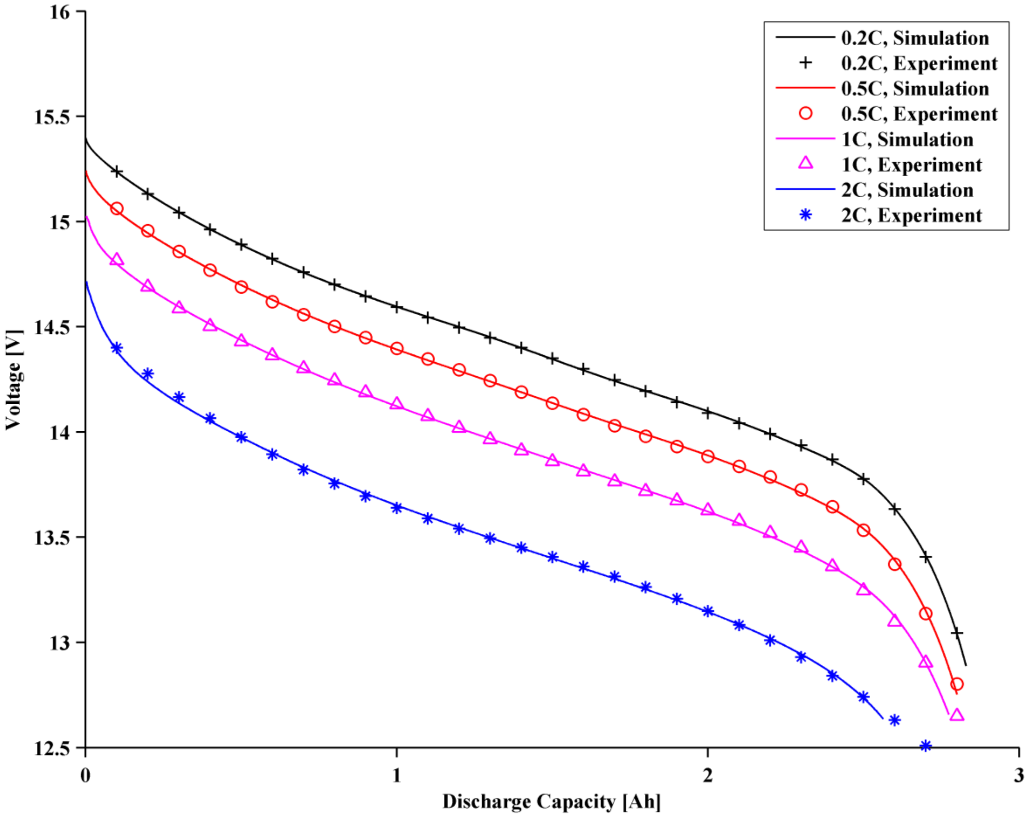

Figure 5-4: Battery pack voltage profile comparison between simulation results and experimental data at different discharge rates and room temperature

Since the main purpose of this study was to investigate behaviours of the battery pack at low temperatures for EV applications, discharge current profiles based on EV driving cycles from Europe, USA and Japan were chosen to test the battery pack under temperature variations. These are European driving cycles for typical urban driving (ECE15), US driving cycles for typical urban (UDDS) and federal highway driving cycles (FHDS) and Japanese driving cycles (J1015 Mode) for typical urban and high speed routes.

Table 5-1: Overall voltage error comparison of battery pack for EV driving cycles between simulation and experimental results

	20ºC	**0ºC**	**-10ºC**
ECE15	5.10% (0.1C) 6.43% (0.3C)	6.14% (0.1C) 9.35% (0.3C)	7.23% (0.1C) 10.48% (0.3C)
UDDS	6.88% (0.1C) 8.43% (0.3C)	8.24% (0.1C) 11.76%(0.3C)	9.32% (0.1C) 13.43% (0.3C)
FHDS	6.03% (0.1C) 7.17% (0.3C)	7.53% (0.1C) 11.21% (0.3C)	8.26% (0.1C) 12.54% (0.3C)
J1015 Mode	4.76% (0.1C) 5.34% (0.3C)	5.87% (0.1C) 8.64% (0.3C)	6.14% (0.1C) 9.76% (0.3C)

To examine the effect of the EV driving cycles on behaviours of the battery pack behaviour, the current profiles with average discharge rates of 0.1C and 0.3C were generated using an EV simulation program with EV driving cycles of ECE15, UDDS, FHDS and the J1015 Mode. These profiles were used to discharge the battery pack at the ambient temperatures of 20ºC, 0ºC and -10ºC. Table 5-1 shows the summary of the overall voltage errors between simulation and experimental results of the battery pack for all EV driving cycles. Generally, it shows that the model had a very good accuracy for the voltage prediction in a wide range of operational temperatures from -10ºC to 20ºC. The battery pack capacities at 0ºC and -10ºC were compared with those of 20ºC as shown in Table 5-2. This shows that the ECE15 had the lowest discharge capacity in all driving cycles.

Table 5-2: Comparison of battery pack capacities at 0°C and -10°C with the capacity at 20°C for EV driving cycles between simulation and experimental results

	0°C	**-10°C**
ECE15	42%(0.1C)	21% (0.1C)
	32% (0.3C)	13% (0.3C)
UDDS	54% (0.1C)	35% (0.1C)
	43% (0.3C)	25% (0.3C)
FHDS	65% (0.1C)	56% (0.1C)
	52% (0.3C)	48%% (0.3C)
J1015 Mode	45% (0.1C)	22% (0.1C)
	35% (0.3C)	15% (0.3C)

To demonstrate EV current profiles for testing the battery pack, the UDDS at 0.3C discharge rate at 20°C and -10°C were chosen as examples. Their current profiles and the corresponding voltage responses from the model simulation and experiments are shown in **Figure 5-5**. The voltage profiles near the end of the discharge are enlarged in both cases to indicate the close voltage variation between simulated and experimental results.

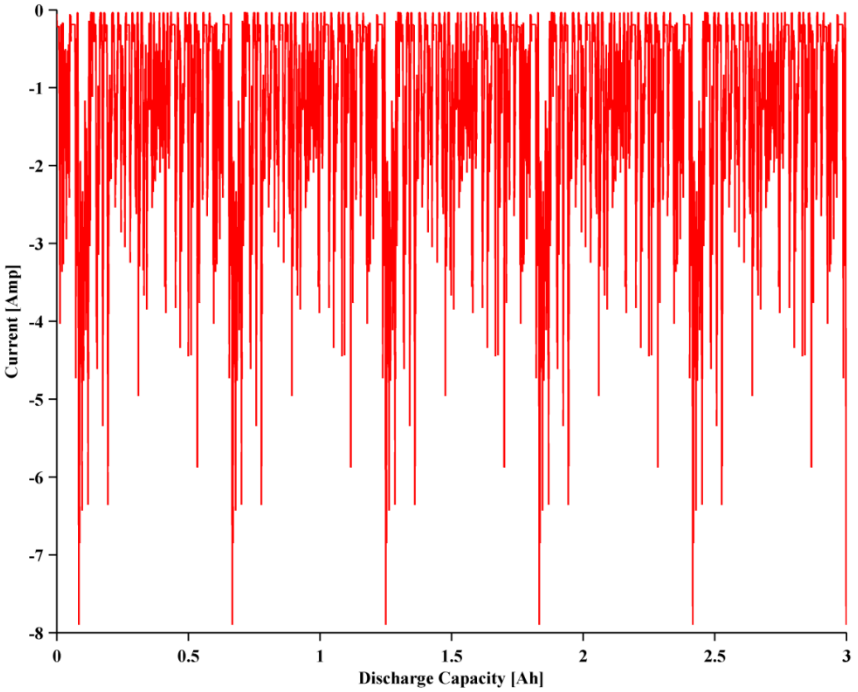
0
-1
-2
-3
-4
-5
-6
-7
-8
Current [Amp]
0
0.5
1
1.5
2
2.5
3
Discharge Capacity [Ah]

(a)

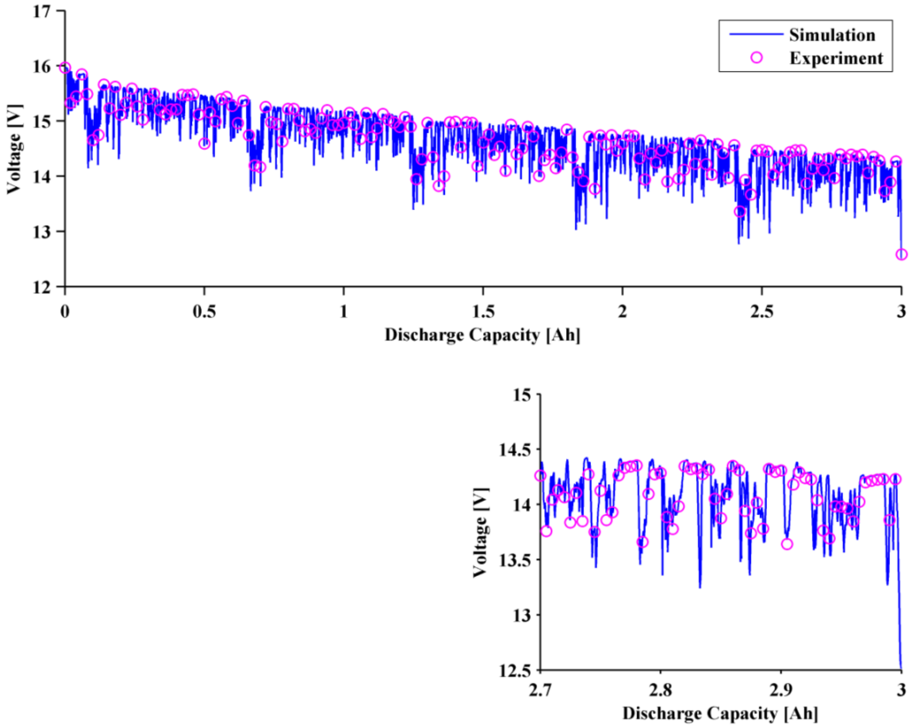
17
16
15
14
13
12
Voltage [V]
Simulation
Experiment
0
0.5
1
1.5
2
2.5
3
Discharge Capacity [Ah]
15
14.5
14
13.5
13
12.5
Voltage [V]
2.7
2.8
2.9
3
Discharge Capacity [Ah]

(b)

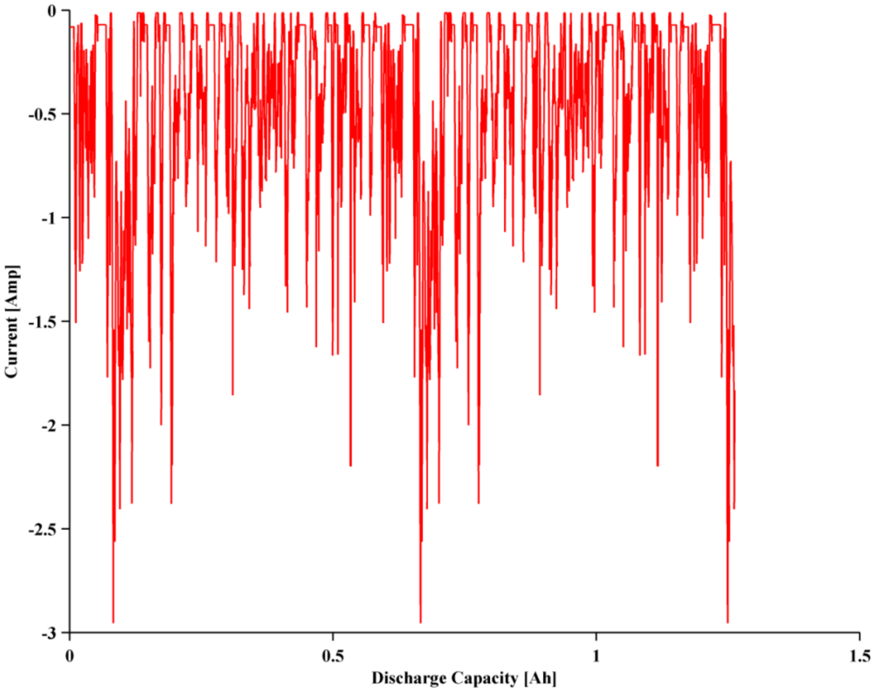
0
-0.5
-1
-1.5
-2
-2.5
-3
Current [Amp]
0
0.5
1
1.5
Discharge Capacity [Ah]

(c)

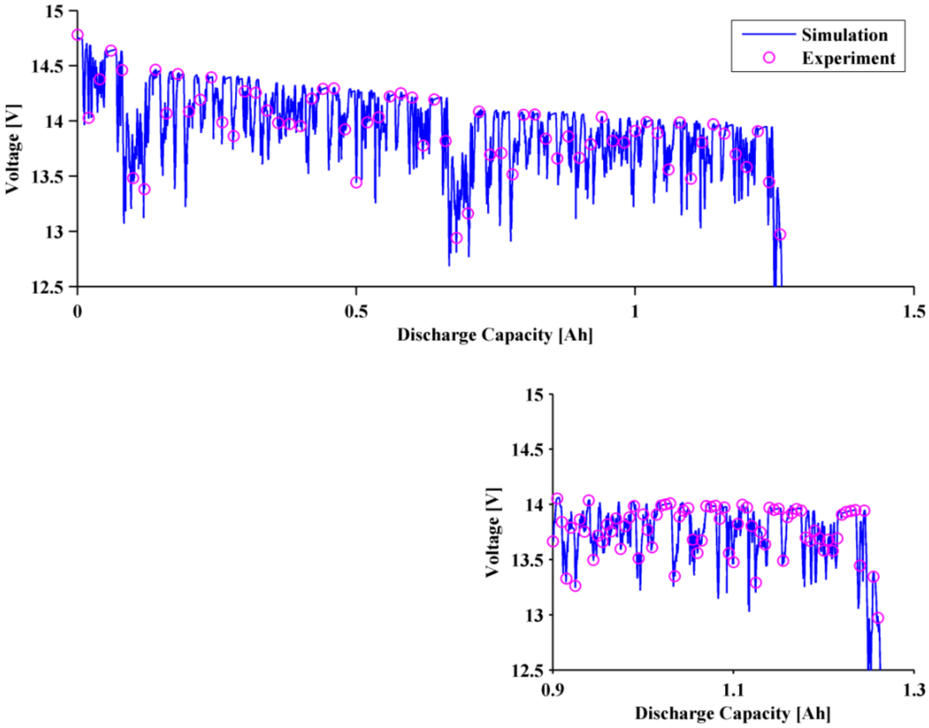
15
14.5
14
13.5
13
12.5
Voltage [V]
0
0.5
1
1.5
Discharge Capacity [Ah]
Simulation
Experiment
15
14.5
14
13.5
13
12.5
Voltage [V]
0.9
1.1
1.3
Discharge Capacity [Ah]

(d)

Figure 5-5: UDDS (a) current profile at 20°C, (b) voltage responses at 20°C from model simulation and experimental data, (c) current profile at -10°C, (d) voltage responses at -10°C from model simulation and experimental data

5-4 Analysis of cell and pack behaviour at low temperatures

In this section, the validated coupled electrochemical-thermal model is used to explore the behaviours of both the cell and pack at low temperatures, specifically in terms of voltage loss. In accordance with voltage loss, resistances were defined as the overpotential divided by the volumetric current density, leading to the Ohmic, kinetic and concentration resistances which are respectively expressed as follows:

$$R_o = \frac{A(0)}{\kappa}\int_0^L \frac{dx}{A(x)} \tag{5-5}$$

Here, the Ohmic resistance R_o reflects electronic and also ionic resistances of both electrodes and electrolyte/separator region.

The kinetic resistance is defined as the ration of kinetic overpotential to volumetric current density. Considering Eq. (5-2) in the anode, we obtain kinetic resistance as

$$R_{k,a} = \frac{\frac{RT}{\alpha_a F}\ln(\frac{i}{i_{0,a}})}{i} \tag{5- 6}$$

The volumetric current density, i in Eq. (5- 6) can be replaced by using the Tafel equation [143]

$$R_{k,a} = \frac{\frac{RT}{\alpha_a F}\ln(\frac{i}{i_{0,a}})}{\frac{\alpha_a+\alpha_c}{\alpha_a} i_0 \ln(\frac{i}{i_{0,a}})} = \frac{RT}{i_0 F}(\frac{1}{\alpha_a+\alpha_c}) \tag{5- 7}$$

Similarly, in the cathode side

$$R_{k,c} = \frac{-\frac{RT}{\alpha_c F}\ln(\frac{i}{-i_{0,c}})}{-\frac{\alpha_a+\alpha_c}{\alpha_c} i_0 \ln(\frac{i}{-i_{0,c}})} = \frac{RT}{i_0 F}(\frac{1}{\alpha_a+\alpha_c}) \tag{5- 8}$$

Therefore, the kinetic concentration resistance can be expressed as

$$R_k = \frac{RT}{i_0 F}\left(\frac{1}{\alpha_a + \alpha_c}\right) \tag{5- 9}$$

Here, the kinetic resistance R_k exhibits the charge-transfer kinetics on the active material-electrolyte interface.

The concentration resistance is defined as the division of concentration overpotential (see Eq.(5-3)) by volumetric current density

$$R_c = \frac{\frac{RT}{nF}\ln(\frac{c_e}{c_s})}{i} \tag{5- 10}$$

Substituting the volumetric current density using the Nernst equation [143]

$$R_c = \frac{\frac{RT}{nF}\ln(\frac{c_e}{c_s})}{\frac{1}{n}\frac{\ln(\frac{c_e}{c_s})}{-\frac{\ln i_{0,a}}{\alpha_a}+\frac{\ln - i_{0,c}}{\alpha_c}}} = \frac{RT}{F}\left(-\frac{\ln i_{0,a}}{\alpha_a}+\frac{\ln - i_{0,c}}{\alpha_c}\right) \tag{5- 11}$$

In this formula, the concentrations resistance R_c expresses the concentration polarization in the electrode and inside the active particles.

5-4-1 Single cell

The influences of temperature and C-rate on the resistances for the single Li-ion cell were analysed (Figure 5-6). The temperature (thermal) effect was examined by comparing the cell resistances at different temperatures and the C-rate effect was reviewed by comparing the resistances at different discharge rates.

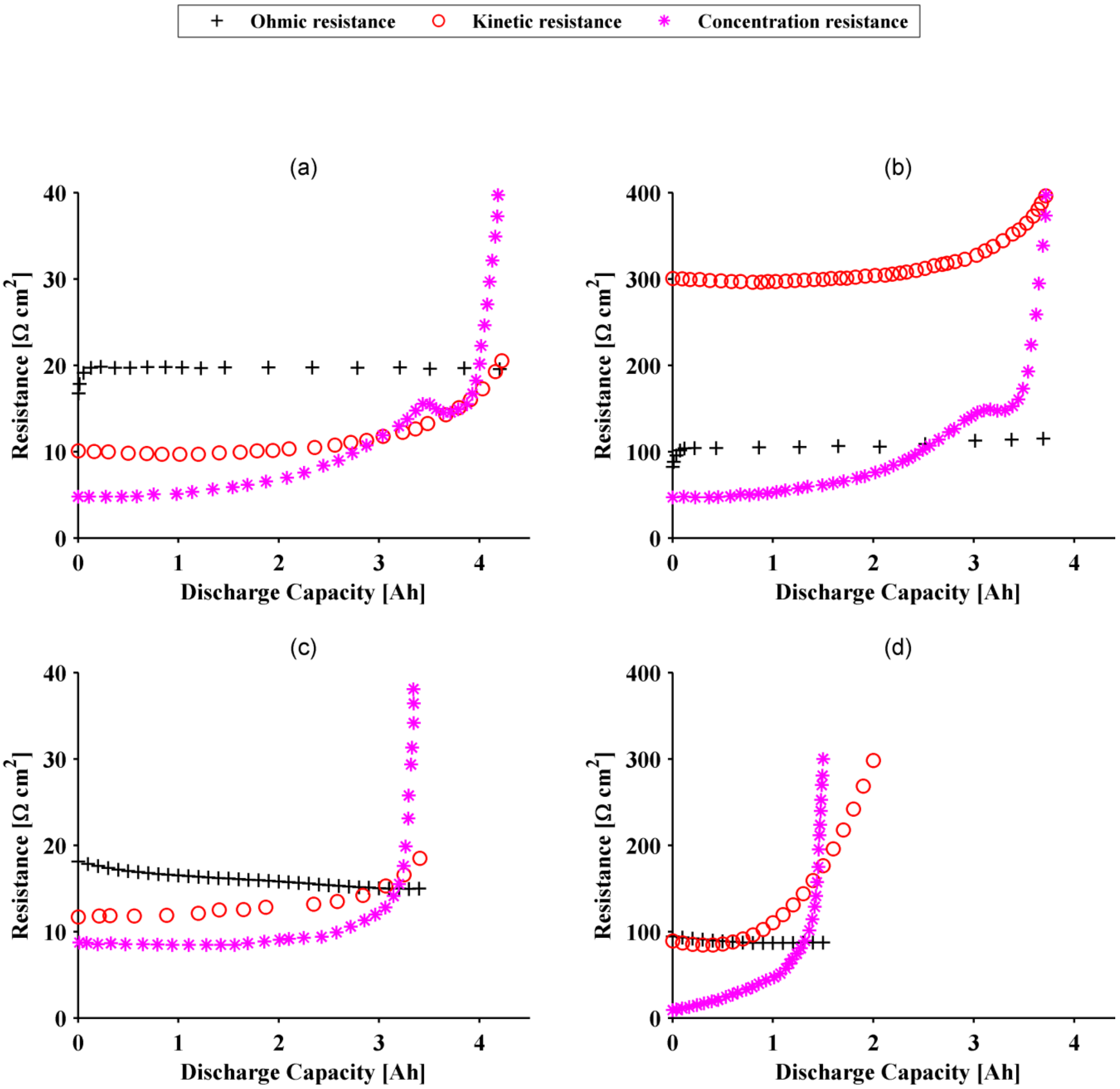

Figure 5-6: Cell resistances at (a) low discharge rate at 20°C, (b) low discharge at -10°C, (c) high discharge rate at 20°C, and (d) high discharge rate at -10°C

Influence of temperature- For the low discharge rate of 0.2C, the cell resistances at 20°C and -10°C are shown in Figure 5-6(a) and (b), respectively. Since the electrolyte acts as a resistor at this low discharge rate, the Ohmic resistance was almost constant during the discharge process and independent of discharge capacity at both temperatures. At the temperature of 20°C, the Ohmic resistance dominated and accounted for approximately half the total cell resistance, indicating that reducing Ohmic resistance improvees Li-ion battery performance. At the temperature of -10°C, although the Ohmic resistance increased five times more than at 20ºC, namely from $20\,\Omega cm^2$ to $115\,\Omega cm^2$, its dominance was superseded by kinetic resistance as a proportion of the total (Figure 5-6 (b)).

Kinetic resistance was initially low and increased gradually due to the reduction of the exchange current density with discharge capacity at both temperatures. These analytical results match well with those from the EIS study [108] and simulation [115] of 18650 Li-ion cell at room temperature. At the temperature of -10ºC, the kinetic resistance was 30 times higher than 20ºC and was dominant in overall resistance. The high kinetic resistance at the temperature of -10ºC was caused by the large kinetic activation energy at both negative (68 kJ/mol) [144] and positive electrodes (49 kJ/mol) [144]. At room temperature of 20ºC the anode kinetic was much faster than the cathode; whereas at the low temperature of -10ºC both anode and cathode kinetics reached a similar level because of the high activation energy of the anode. Hence, at low temperatures the activation energy of anode was high and became more rate limiting. These analytical results of the charge-transfer resistances are consistent with Tafel polarization measures [93] and results from the EIS study [108] and simulation [115].

At room and low temperatures, the concentration resistances also increased and reached maximum values at the end of the discharge. The concentration resistance at the temperature of -10ºC was ten times higher than those at 20ºC due to the lower solid state diffusivity at low rather than high temperatures. Moreover, the kinetic and concentration resistances in the discharged state were much higher than those in charged state.

For the high discharge rate of 2C, the cell resistance at room (20ºC) and low temperature -10ºC), are shown in Figure 5-6(c) and Figure 5-6(d), respectively. At the high discharge rate of 2C, the electrolyte does not act as a constant resistance at the low discharge rate of 0.2C. This is because during the discharge process the thermal effect of high discharge rate increases the ionic conductivity in the electrolyte and the separator where the most of the reaction current is initially generated at both room and low temperatures, which leads to a decreasing trend of the Ohmic resistance. (Figure 5-6 (d)).

Kinetic resistances increased and displayed maximum values at the end of the discharge due to the slow kinetics and high activation energy at both room and low temperatures.

The concentration resistances at room and low temperatures increased toward the end of the discharge. The concentration resistances at room and low temperatures increase towards the end of discharge. The concentration resistances at the low temperature are around 35 times higher than those at the room temperature, high cathode exchange current density causes high concentration resistance at low temperature of -10°C.

At the low temperature of -10°C, kinetic and concentration resistances increased quickly, particularly after the discharge capacity of 1.0Ah, equivalent to about 30% of the normal capacity, as shown in Figure 5-6(d). These resistances caused cell voltage to drop rapidly which reached cut-off voltage earlier at -10°C than 20°C. The corresponding capacity was only 1.5Ah, 40% of normal capacity.

Influence of C-rate- Cell resistances at room temperature (20°C) for the high discharge rate of 2C and low discharge rate of 0.2C are shown in Figure 5-6(a) and Figure 5-6(c), respectively. These show that Ohmic resistance is almost constant at a low discharge rate and decreased at a high rate. Moreover, the Ohmic resistance at the room temperature dominated the overall resistance and accounted for almost half the total cell resistances at low rates.

Kinetic resistances at both low and high rates of discharge at room temperature (20°C) were initially low, but increased gradually as discharge continued. Kinetic resistances at the high discharge rate were marginally higher than those at the low rate. As mentioned, Kinetic resistance reflected the charge-transfer kinetics of electrolyte and active particles. The charge-transfer kinetic was strongly temperature dependent [145] and its values were almost constant at different discharge rates.

Concentration resistances increased at both low and high discharge rates. The solid phase diffusivity at the high discharge rate of 2C became a dominant effect that caused the disappearance of peaks and troughs evident at low discharge.

Based on the simulation results, the electrolyte ionic conductivity was lowered significantly over the threshold concentration (3mol/L) which made a significant potential drop in the electrolyte [103] and eventually a sharp increase in kinetic resistance. Both kinetic and concentration resistances increased quickly as discharge continued. They increased sharply at high discharge rates and were important limiting factors.

5-4-2 Battery pack

The battery pack resistances under UDDS with the average discharge rate of 0.3C are shown in Figure 5-7(a) at room temperature (20oC) and low temperature (-10C) in Figure 5-7(b). Figure 5-7(a), shows that Ohmic resistance at 20oC was almost constant which indicates the same trend as that shown in Figure 5-6(a) at the low discharge rate. Kinetic and concentration resistances started to increase at approximately 50% of the discharge capacity due to the high values of the exchange current density and solid concentration.

At the low temperature of -10oC, ionic conductivity of electrolyte at the electrode/electrolyte region was low. The low value of ionic conductivity caused an immobilization of Li+ ions in the anode electrolyte which needed to be consumed by the cathode electrolyte. The sharp increase in concentration resistance was due to the various amounts of exchange current density as the applied current at the EV driving cycle varied with continued discharge (Figure 5-5 (a) and Figure 5-5(c)). Hence, concentration resistances became limiting factors for EV driving cycles at low temperature (-10^{o}C). This indicates a higher value of ionic conductivity of electrolytes may help to improve the EV performance at low temperatures.

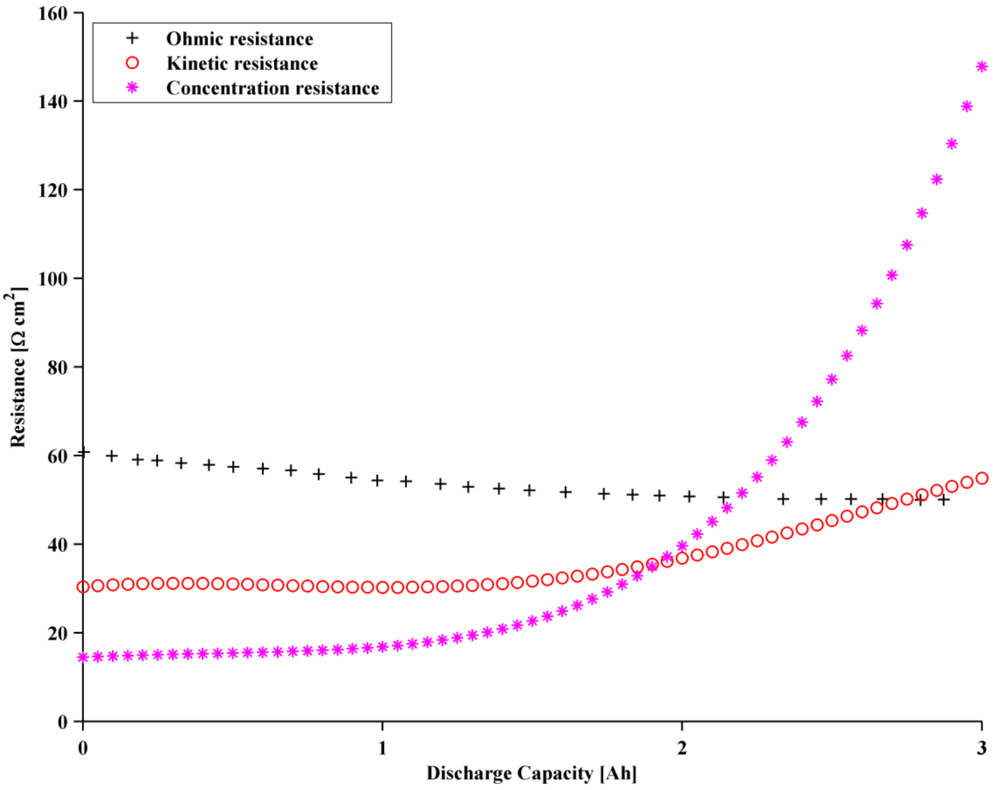

(a)

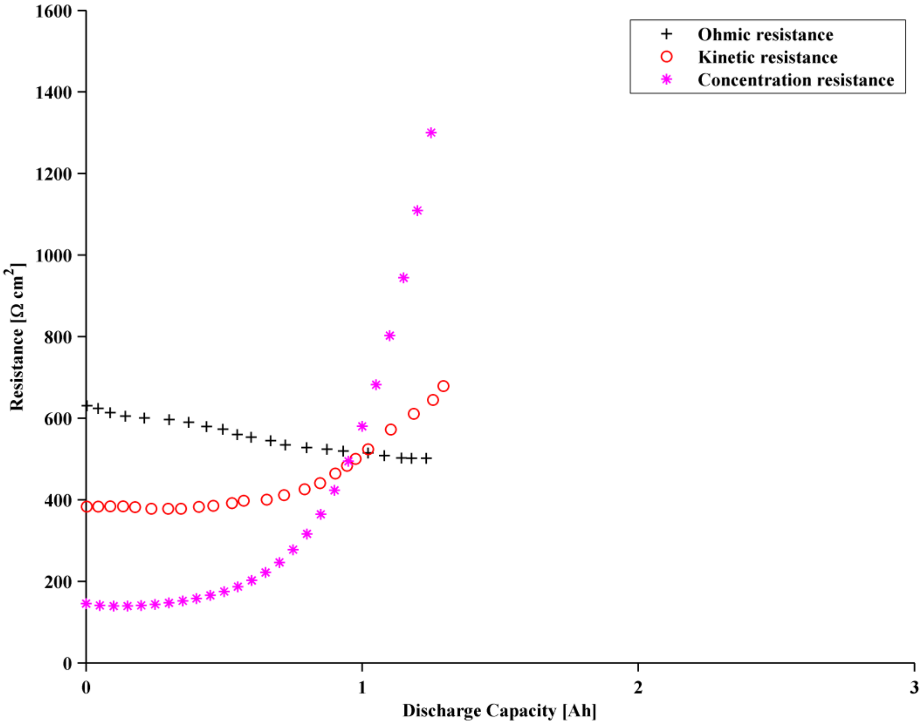

(b)

Figure 5-7: Cell resistances under UDDS at (a) 20°C, (b) -10°C

Figure 5-7(b) shows that concentration resistances at -10oC increased sharply, leading to a capacity loss of 50% compared to nominal capacity.

As mentioned in the previous section, the battery pack under ECE15 have the lowest discharge capacity among all EV driving cycles at the low temperature (-10oC). Correspondingly, the overall resistances of the battery pack have the highest values during discharging under ECE15. Therefore, battery pack resistances under ECE15 was chosen to show trends in changing resistances. Figure 5-8 shows concentration resistance significantly increased at the end of the discharge due to the sharp fall of ionic conductivity of electrolyte especially in the anode affected by exchange current density.

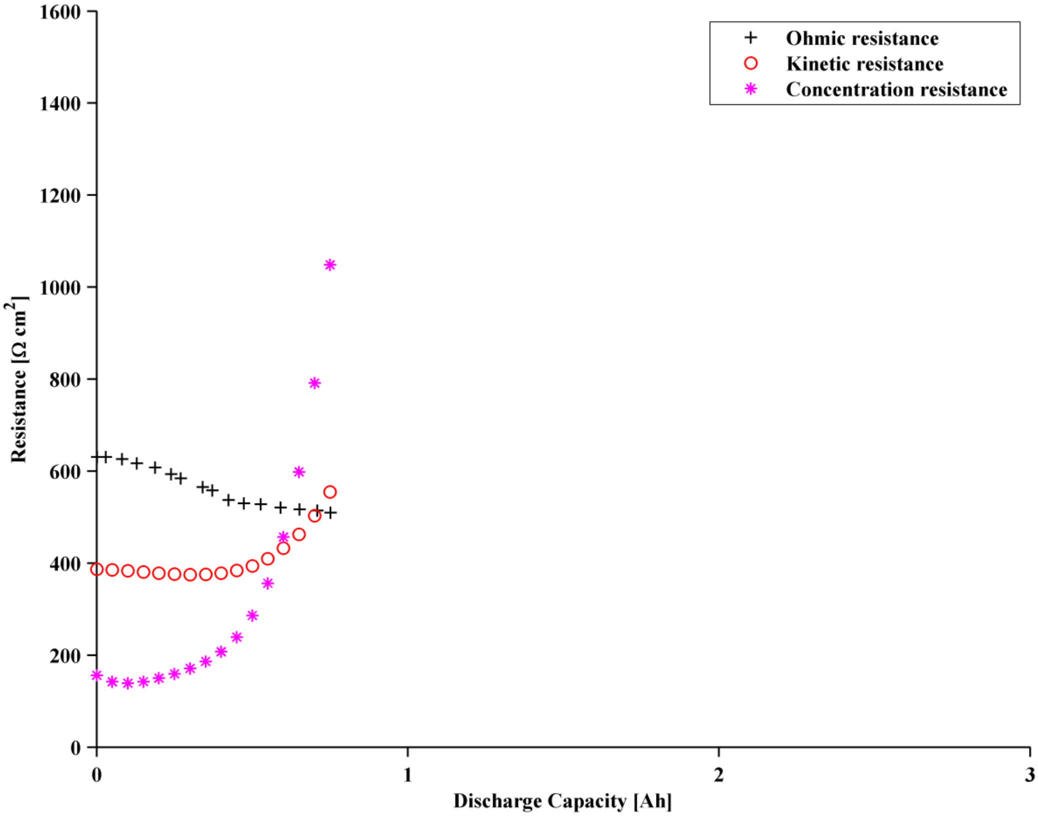

Figure 5-8: Cell resistances under ECE15 at -10°C

5-5 Summary

An electrochemical-thermal coupled model is proposed to evaluate the performance of a single Li-ion cell and a pack. The proposed model is validated against the experimental data obtained from the single Li-ion cell and the pack over a wide range of constant current discharge rates, the current profiles based on EV driving cycles and various temperatures, particularly at subzero temperature. They generally have good agreement in term of the prediction of voltage and temperature. The simulation has been conducted in the validated model to gain insights of the Li-ion cell and the pack at low temperatures. The conclusions can be drawn as follows:

1. Cell performance depends not only on ambient temperatures, but also on discharge rates and thermal conditions. At room temperatures, the Ohmic resistance dominates the total resistances of the single cell. The electrolyte resistances are responsible for low battery performance at low and high discharge rates. At the temperature of -10^{o}C, charge-transfer kinetics is the limiting factor in low discharge rate operation while the high thermal-related solid phase diffusivity causes high concentration resistance; this becomes the limiting factor at high discharge rates. Therefore, an effective way to enhance cell performance at low temperatures is to increase the electrolyte concentration, but within critical levels.

2. The performance of Li-ion battery packs under EV driving cycles is generally poor at low temperatures, as EV driving cycles with high power demand cause large increase of exchange current densities which reduces the achievable maximum discharge capacity of the Li-ion battery packs. In addition, the concentration resistance is high at low temperatures, thus the increasing ionic conductivity in electrolyte is most beneficial to improve pack discharge capacity.

Chapter 6 Conclusions and future work

6-1 Conclusions

EVs can be considered an ideal solution for transportation because they are pollutant free and independent of petroleum. Of all cell chemistries, Li-ion battery cells are the best candidate as energy storage systems in EVs due to their high-specific energy, high power and high- discharge capacity. Despite rapid growth of Li-ion applications in the EV market, its market share in the automotive industry remains limited. In addition to high battery cost, Li-ion batteries suffer from poor performance at low temperatures. Li-ion batteries are highly temperature dependent and temperature affects several aspects of the batteries in the operation of EVs: charge acceptance, power and energy capability, reliability, safety issues (e.g. thermal runaway) and life. Hence, in this dissertation, the market barrier of poor performance of Li-ion battery cells and battery packs in EV applications was studied using numerical modelling and a simulation approach. Modelling simulations provide a cost-effective way to reveal the fundamental mechanisms that dictate battery behaviour.

An electrochemical-thermal coupled model was developed for Li-ion battery cells. This model consists of a set of non-linear partial differential equations that contains non-linear source terms. Existing numerical approaches to solve this set of equations are time-consuming and computationally expensive. In this study, a novel numerical method was introduced to determine the solution of the electrochemical-thermal model for a Li-ion battery cell quickly. This method was implemented in four steps: (1) a physical analogy of an electrochemical process to an electric circuit was used to solve charge conservation equations; (2, 3) a control volume method was used to solve species conservation equations; and (4) the thermal equations were solved and the temperature distribution in the battery cell was found using control volume methods. The model was then validated against 26650 Li-ion cells across a wide range of discharge rates and the effectiveness of the developed numerical method was studied.

In EV applications, the Li-ion battery pack consisting of multiple cells in series and parallel is required to meet the high demands of current, voltage, power and energy. The temperatures of each cell in the pack are monitored and controlled to prevent them from gradually rising to the maximum allowable value that would accelerate the degradation rate and lead to thermal runaway. Hence, it is necessary to fully understand the thermal characteristics of Li-ion battery packs under EV driving cycles and ensure that the cell temperature in the pack is effectively controlled below the maximum allowable value. In this study, a comprehensive electrochemical-thermal model coupled with a resistive-network model was developed for Li-ion battery packs to study the rate-limiting factors under EV applications. The proposed model was validated against a battery pack consisting of 16 Li-ion battery cells (26650 Li-ion battery cells) in a 4S4P arrangement in different discharge rates, ambient temperatures, and EV driving cycles. It should be noted that the proposed model was validated in both the presence and absence of a cooling fan (that is, both forced and natural convection). Although the cooling fan reduces battery pack temperature, it consumes power, and this factor requires careful consideration in thermal management. In addition, the effectiveness of the resistive network was studied to predict the temperature rise. Based on the simulation results, the accuracy of the temperature prediction was improved by a factor of 2.6. The simulation results of large battery packs at high ambient temperatures revealed the temperature of the Li-ion battery cells can exceed the safe thermal range. It was concluded that the design of a proper thermal management system for battery packs in EV applications is essential to ensure all battery cells operate within the safe thermal range.

The poor performance of Li-ion batteries at low temperatures poses a technical barrier for EV applications. A theoretical electrochemical-thermal model was proposed to evaluate the performance of a Li-ion cell and a Li-ion battery pack at low temperatures. The specifically designed Li-ion pouch cells were made in the laboratory with known internal parameters and a battery pack was built comprising four pouch cells connected in series. The proposed model was validated on both the cell and pack over a wide range of temperatures from -10C to 20C at various constant-discharge currents and discharge-current profiles based on EV driving cycles. It was found that the terminal voltages of the cell and pack calculated from the proposed model were consistent with those obtained from the experiments. A simulation was then implemented in the validated model to provide insights into the behaviour of both the cell and pack. This revealed that at the low temperature of -10C degrees, a high-discharge rate can cause low diffusivity of the salt in the electrolyte and the lithium-ion in the graphite particles. This results in high Ohmic surface and concentration resistances that lead to poor performance (low available capacity) of the Li-ion cell and battery pack, particularly under current profiles based on EV driving cycles with high power demand.

6-2 Future work

The following topics are proposed for future work relevant to the research carried out by the thesis:

- A location dependent value for convective heat coefficient (*h*) is preferred. In large battery pack designs for EVs, a cooling channel is planned to cool battery cells by the suction effect of the fan. When the air flows past cooling channel, a thermal boundary layer is formed. In the thermal boundary layer, the convective heat transfer coefficient is not constant and should be calculated based on the velocity of the air, the location of the battery cell and the air-pressure gradient.
- The experimental validation of large battery packs in current EV use at high temperatures is required to examine the accuracy of the proposed electrochemical-thermal model. This validation would comprise the validation of the increased surface area, high-heat generation and heat dissipations, higher values of internal resistances, and the high final temperature of the battery cells.

- An experimental setting for temperatures lower than $-10^{o}C$ is preferred. At these lower temperatures, the performance of the Li-ion battery pack is even less and the thermal dependency of their electrochemical characteristics become more significant.
- The ageing mechanisms evident at low temperatures are a significant barrier in battery packs under EV applications. Therefore, considering different ageing mechanisms and degradation models would be beneficial to understanding and implementing EV applications.
- Based on the poor performance of the Li-ion battery cells at low temperatures, heating the battery cell is one way to improve performance. Heating strategies in terms of energy, time and cost should be investigated. Furthermore, the effect of heating on the Li-ion battery cell's life should be addressed, which cannot be predicted using the current model.

List of Authors' Publications

- Conference papers:
    - Amiribavandpour, P., W. X. Shen, and A. Kapoor, *The mathematical model of 18650 lithium-ion battery in electric vehicles*. in *Proceedings of the 2013 IEEE 8th Conference on Industrial Electronics and Applications, ICIEA 2013,* 2013.
    - Amiribavandpour, P., W. X. Shen, and A. Kapoor. *Development of thermal electrochemical model for lithium ion 18650 battery packs in electric vehicles*. in *2013 9th IEEE Vehicle Power and Propulsion Conference, IEEE VPPC 2013,* 2013.

- Journal Papers
    - Amiribavandpour, P., W. X. Shen, and A. Kapoor, *A novel efficient numerical method to simulate electrochemical process for a lithium ion battery.* Russian Journal of Electrochemistry, 2015: p. 1-11.
    - Amiribavandpour, P, W. X. Shen, D. Mu, and A. Kapoor, *An improved theoretical electrochemical-thermal modelling of lithium-ion battery packs in electric vehicles.* Journal of Power Sources, 2015. **284**: p. 328-338.
    - Amiribavandpour, P, W. X. Shen, D. Mu, and A. Kapoor, *Performance evaluation of lithium ion batteries at low temperatures for electric vehicles*, Sumitted to Journal of Electrochemical Society.

References

1. HUSAIN, I., *Electric and Hybrid Vehicles Design Fundamentals, Second Edition*. 2010, : CRC Press.
2. CHAN, C.C. 2001. *Modern electric vehicle technology*.
3. EHSANI, M., *Modern Electric, Hybrid Electric, and Fuel Cell Vehicles Fundamentals, Theory, and Design, Second Edition*, in *Modern Electric, Hybrid Electric, and Fuel Cell Vehicles: Fundamentals, Theory, and Design, Second Edition*, GAO, Y.&EMADI, A., Editors. 2009, Hoboken : Taylor and Francis: Hoboken.
4. CHAN, C. 2002. The state of the art of electric and hybrid vehicles. *Proc. IEEE,* 90**,** 247-275.
5. LEVINE, S. 2015. *The powerhouse : inside the invention of a battery to save the world,* New York, New York : VIKING.
6. NAZRI, G.&PISTOIA, G. 2009. *Lithium batteries : science and technology,* New York, N.Y., New York, N.Y. : Springer.
7. WU, Y., *Lithium-Ion Batteries Fundamentals and Applications*, in *Electrochemical Energy Storage and Conversion, Volume 4*. 2015, Hoboken : CRC Press: Hoboken.
8. DOYLE, M., NEWMAN, J., GOZDZ, A.S., SCHMUTZ, C.N.&TARASCON, J.M. 1996. Comparison of modeling predictions with experimental data from plastic lithium ion cells. *Journal of the Electrochemical Society,* 143**,** 1890-1903.
9. SIKHA, G., POPOV, B.N.&WHITE, R.E. 2004. Effect of porosity on the capacity fade of a lithium-ion battery theory. *Journal of the Electrochemical Society,* 151**,** A1104-A1114.
10. WANG, C.Y., GU, W.B.&LIAW, B.Y. 1998. Micro-macroscopic coupled modeling of batteries and fuel cells: I. Model development. *Journal of the Electrochemical Society,* 145**,** 3407-3417.
11. DOYLE, M., FULLER, T.&NEWMAN, J. 1993. Modeling of galvanostatic charge and discharge of the lithium/ polymer/insertion cell. *Journal of the Electrochemical Society,* 140**,** 1526-1533.
12. FULLER, T.F., DOYLE, M.&NEWMAN, J. 1994. Simulation and Optimization of the Dual Lithium Ion Insertion Cell. *Journal of the Electrochemical Society,* 141**,** 1-10.
13. GU, W.B., WANG, C.Y.&LIAW, B.Y. 1998. Micro-macroscopic coupled modeling of batteries and fuel cells: II. Application to nickel-cadmium and nickel-metal hydride cells. *Journal of the Electrochemical Society,* 145**,** 3418-3427.
14. GAGNON, F., ZIEGLER, D.&FAFARD, M. 2014. Electrochemical modelling using electroneutrality equation as a constraint. *Journal of Applied Electrochemistry,* 44**,** 361-381.
15. DARCOVICH, K., GUPTA, N., DAVIDSON, I.J.&CARONI, T. 2010. Residential electrical power storage scenario simulations with a large-scale lithium ion battery. *Journal of Applied Electrochemistry,* 40**,** 749-755.
16. BOGRACHEV, D.A., VOL'FKOVICH, Y.M., DUBASOVA, V.S., NIKOLENKO, A.F., PONOMAREVA, T.A.&SOSENKIN, V.E. 2013. Development and experimental verification of a mathematical model of lithium ion battery. *Russian Journal of Electrochemistry,* 49**,** 115-123.
17. TESLAMOTORS, Model S Tesla Motors Australia, accessed in 20 Jan 2016, https://www.teslamotors.com/en_AU/models.
18. NISSAN, Nissan LEAF | 100% Electric Car, Zero Petrol, accessed in 20 Jan 2016, http://www.nissan.com.au/Cars-Vehicles/LEAF/Overview.
19. BMW, BMW i3 2014 Overview, accessed in 20 Jan 2016 2016,http://www.bmw.com.au/com/en/newvehicles/i/i3/2013/showroom/introduction.html.
20. RENAULT, ZOE Electric Renault, accessed in 20 Jan 2016, https://www.renault.co.uk/vehicles/new-vehicles/zoe.html.
21. PANASONIC, Li-ion Batteries, accessed in 20 Feb 2016,https://industrial.panasonic.com.
22. EGOLF, The e-Golf is all Golf. No gas tank. VW does electric., accessed in 20 Jan 2016,https://www.vw.com/models/e-golf/.

23. KIA, Kia Soul EV Electric Car, accessed in 20 Jan 2016, http://www.kia.com/us/en/vehicle/soul-ev/2016.
24. FORD, Focus Electric | View Focus Electric Highlights, accessed in 20 Jan 2016, http://www.ford.com/cars/focus/trim/electric/
25. PLUGINCARS, Fiat 500e, accessed in 20 Jan 2016, http://www.plugincars.com/fiat-500e
26. WINTER, M., BESENHARD, J.O., SPAHR, M.E.&NOVÁK, P. 1998. Insertion Electrode Materials for Rechargeable Lithium Batteries. *Advanced Materials,* 10, 725-763.
27. ANDERSSON, A. 2001. *Surface Phenomena in Li-Ion Batteries [Elektronisk resurs],* Uppsala, Acta Universitatis Upsaliensis.
28. GUYOMARD, D.&TARASCON, J.M. 1995. High voltage stable liquid electrolytes for Li.sub.1+x Mn.sub.2O.sub.4/carbon rocking-chair lithium batteries. *Journal of Power Sources,* 54, 92.
29. GUYOMARD, D.&TARASCON, J. 1993. RECHARGEABLE LI1+XMN2O4/CARBON CELLS WITH A NEW ELECTROLYTE-COMPOSITION - POTENTIOSTATIC STUDIES AND APPLICATION TO PRACTICAL CELLS. *J. Electrochem. Soc.,* 140, 3071-3081.
30. TARASCON, J.M.&GUYOMARD, D. 1994. New electrolyte compositions stable over the 0 to 5 V voltage range and compatible with the Li 1+xMn 2O 4/carbon Li-ion cells. *Solid State Ionics,* 69, 293-305.
31. EINELI, Y., THOMAS, SR., KOCH, V., AURBACH, D., MARKOVSKY, B.&SCHECHTER, A. 1996. Ethylmethylcarbonate, a promising solvent for Li-ion rechargeable batteries. *J. Electrochem. Soc.,* 143, L273-L277.
32. EINELI, Y., MCDEVITT, S., AURBACH, D., MARKOVSKY, B.&SCHECHTER, A. 1997. Methyl propyl carbonate: A promising single solvent for Li-ion battery electrolytes. *J. Electrochem. Soc.,* 144, L180-L184.
33. HEIDER, U., OESTEN, R.&JUNGNITZ, M. 1999. Challenge in manufacturing electrolyte solutions for lithium and lithium ion batteries quality control and minimizing contamination level. *J. Power Sources,* 81, 119-122.
34. CHEN, X., SHEN, W., CAO, Z.&KAPOOR, A. 2014. A novel approach for state of charge estimation based on adaptive switching gain sliding mode observer in electric vehicles. *Journal of Power Sources,* 246, 667-678.
35. CHAN, C.C., LO, E.W.C.&SHEN, W. 2000. Available capacity computation model based on artificial neural network for lead-acid batteries in electric vehicles. *Journal of Power Sources,* 87, 201-204.
36. SHEN, W.X., CHAN, C.C., LO, E.W.C.&CHAU, K.T. 2002. A new battery available capacity indicator for electric vehicles using neural network. *Energy Conversion and Management,* 43, 817-826.
37. VERBRUGGE, M. 2007. Adaptive, multi-parameter battery state estimator with optimized time-weighting factors. *Journal of Applied Electrochemistry,* 37, 605-616.
38. ARORA, P., DOYLE, M., GOZDZ, A.S., WHITE, R.E.&NEWMAN, J. 2000. Comparison between computer simulations and experimental data for high-rate discharges of plastic lithium-ion batteries. *Journal of Power Sources,* 88, 219-231.
39. GU, W.B.&WANG, C.Y. 2000. Thermal-electrochemical modeling of battery systems. *Journal of the Electrochemical Society,* 147, 2910-2922.
40. SONG, L.&EVANS, J.W. 2000. Electrochemical-thermal model of lithium polymer batteries. *J. Electrochem. Soc.,* 147, 2086-2095.
41. SRINIVASAN, V.&WANG, C.Y. 2003. Analysis of electrochemical and thermal behavior of Li-ion cells. *Journal of the Electrochemical Society,* 150, A98-A106.
42. KUMARESAN, K., SIKHA, G.&WHITE, R.E. 2008. Thermal model for a Li-ion cell. *Journal of the Electrochemical Society,* 155, A164-A171.
43. GU, W.&WANG, C. 2000. Thermal-electrochemical modeling of battery systems. *J. Electrochem. Soc.,* 147, 2910-2922.

44. WANG, C.Y.&SRINIVASAN, V. 2002. Computational battery dynamics (CBD)—electrochemical/thermal coupled modeling and multi-scale modeling. *Journal of Power Sources,* 110**,** 364-376.
45. PALS, C.R.&NEWMAN, J. 1995. Thermal modeling of the lithium/polymer battery. I. Discharge behavior of a single cell. *Journal of the Electrochemical Society,* 142**,** 3274-3281.
46. FANG, W., KWON, O.J.&WANG, C.Y. 2010. Electrochemical-thermal modeling of automotive Li-ion batteries and experimental validation using a three-electrode cell. *International Journal of Energy Research,* 34**,** 107-115.
47. GERVER, R.E.&MEYERS, J.P. 2011. Three-Dimensional Modeling of Electrochemical Performance and Heat Generation of Lithium-Ion Batteries in Tabbed Planar Configurations. *Journal of The Electrochemical Society,* 158**,** A835-A843.
48. KIM, G.-H., SMITH, K., LEE, K.-J., SANTHANAGOPALAN, S.&PESARAN, A. 2011. Multi-Domain Modeling of Lithium-Ion Batteries Encompassing Multi-Physics in Varied Length Scales. *Journal of The Electrochemical Society,* 158**,** A955-A969.
49. CHO, Y.I.&HALPERT, G. 1986. *J. Power Sources,* 18**,** 2-3.
50. ZHANG, X. 2011. Thermal analysis of a cylindrical lithium-ion battery. *Electrochimica Acta,* 56**,** 1246-1255.
51. HATCHARD, T.D., MACNEIL, D.D., BASU, A.&DAHN, J.R. 2001. Thermal Model of Cylindrical and Prismatic Li-ion Cells. *J. Electrochem. Soc.,* 148.
52. EVANS, T.I.&WHITE, R.E. 1989. *J. Electrochem. Soc.,* 136.
53. AL HALLAJ, S., MALEKI, H., HONG, J.S.&SELMAN, J.R. 1999. Thermal modeling and design considerations of lithium-ion batteries. *Journal of Power Sources,* 83**,** 1-8.
54. GOMADAM, P.M., WEIDNER, J.W., DOUGAL, R.A.&WHITE, R.E. 2002. Mathematical modeling of lithium-ion and nickel battery systems. *Journal of Power Sources,* 110**,** 267-284.
55. REIMERS, J.N. 2006. Predicting current flow in spiral wound cell geometries. *Journal of Power Sources,* 158**,** 663-672.
56. MA, Y., TENG, H.&THELLIEZ, M. 2011. *SAE Int. J. Engines,* 3.
57. CHEN, S.C., WAN, C.C.&WANG, Y.Y. 2005. Thermal analysis of lithium-ion batteries. *Journal of Power Sources,* 140**,** 111-124.
58. CHEN, Y.B., LI, J., QI, Y., MIAO, X., ZHOU, Y., REN, D.&GUO, G.Z. 2010. The effects of electromagnetic pulses (EMP) on the bioactivity of insulin and a preliminary study of mechanism. *International Journal of Radiation Biology,* 86**,** 22-26.
59. PINSONA, M.B.&BAZANT, M.Z. 2013. Theory of SEI formation in rechargeable batteries: Capacity fade, accelerated aging and lifetime prediction. *Journal of the Electrochemical Society,* 160**,** A243-A250.
60. GUO, M., SIKHA, G.&WHITE, R.E. 2011. Single-particle model for a lithium-ion cell: Thermal behavior. *Journal of the Electrochemical Society,* 158**,** A122-A132.
61. SANTHANAGOPALAN, S., GUO, Q., RAMADASS, P.&WHITE, R.E. 2006. Review of models for predicting the cycling performance of lithium ion batteries. *Journal of Power Sources,* 156**,** 620-628.
62. ZHANG, D., POPOV, B.N.&WHITE, R.E. 2000. Modeling lithium intercalation of a single spinel particle under potentiodynamic control. *Journal of the Electrochemical Society,* 147**,** 831-838.
63. SUBRAMANIAN, V.R., DIWAKAR, V.D.&TAPRIYAL, D. 2005. Efficient macro-micro scale coupled modeling of batteries. *Journal of the Electrochemical Society,* 152**,** A2002-A2008.
64. SUBRAMANIAN, V.R., BOOVARAGAVAN, V., RAMADESIGAN, V.&ARABANDI, M. 2009. Mathematical model reformulation for lithium-ion battery simulations: Galvanostatic boundary conditions. *Journal of the Electrochemical Society,* 156**,** A260-A271.
65. METHEKAR, R.N., RAMADESIGAN, V., PIRKLE JR, J.C.&SUBRAMANIAN, V.R. 2011. A perturbation approach for consistent initialization of index-1 explicit differential-algebraic

equations arising from battery model simulations. *Computers and Chemical Engineering,* 35**,** 2227-2234.

66. NORTHROP, P.W.C., RAMADESIGAN, V., DE, S.&SUBRAMANIAN, V.R. 2011. Coordinate transformation, orthogonal collocation, model reformulation and simulation of electrochemical-thermal behavior of lithium-ion battery stacks. *Journal of the Electrochemical Society,* 158**,** A1461-A1477.
67. PLICHTA, E.J.&SALOMON, M. 1984. Low temperature studies on rechargeable lithium cells. *Journal of Power Sources,* 13**,** 319-326.
68. SUBRAMAMAN, V.R., TAPRIYAL, D.&WHITE, R.E. 2004. A boundary condition for porous electrodes. *Electrochemical and Solid-State Letters,* 7**,** A259-A263.
69. RAMADASS, P., HARAN, B., GOMADAM, P.M., WHITE, R.&POPOV, B.N. 2004. Development of First Principles Capacity Fade Model for Li-Ion Cells. *Journal of the Electrochemical Society,* 151**,** A196-A203.
70. BOTTE, G.G., SUBRAMANIAN, V.R.&WHITE, R.E. 2000. Mathematical modeling of secondary lithium batteries. *Electrochimica Acta,* 45**,** 2595-2609.
71. NING, G., WHITE, R.E.&POPOV, B.N. 2006. A generalized cycle life model of rechargeable Li-ion batteries. *Electrochimica Acta,* 51**,** 2012-2022.
72. THOMAS, K.E.&NEWMAN, J. 2003. Thermal modeling of porous insertion electrodes. *Journal of the Electrochemical Society,* 150**,** A176-A192.
73. CAI, L.&WHITE, R.E. 2009. Reduction of model order based on proper orthogonal decomposition for lithium-ion battery simulations. *Journal of the Electrochemical Society,* 156**,** A154-A161.
74. FORMAN, J.C., BASHASH, S., STEIN, J.L.&FATHY, H.K. 2011. Reduction of an electrochemistry-based li-ion battery model via quasi-linearization and Pad́ approximation. *Journal of the Electrochemical Society,* 158**,** A93-A101.
75. SELMAN, J.R., AL HALLAJ, S., UCHIDA, I.&HIRANO, Y. 2001. Cooperative research on safety fundamentals of lithium batteries. *Journal of Power Sources,* 97-98**,** 726-732.
76. PARK, C.&JAURA, A. 2003. *SAE Transactions,* 112**,** 1835-1842.
77. MI, C., LI, B., BUCK, D.&OTA, N., in *Vehicle Power and Propulsion Conference*. 2007, IEEE. p. 107-111.
78. YE, Y., SHI, Y., CAI, N., LEE, J.&HE, X. 2012. Electro-thermal modeling and experimental validation for lithium ion battery. *Journal of Power Sources,* 199**,** 227-238.
79. BERNARDI, D., PAWLIKOWSKI, E.&NEWMAN, J. 1985. GENERAL ENERGY BALANCE FOR BATTERY SYSTEMS. *Journal of the Electrochemical Society,* 132**,** 5-12.
80. ZHANG, Z., JIA, L., ZHAO, N.&YANG, L. 2011. Thermal modeling and cooling analysis of high-power lithium ion cells. *Journal of Thermal Science,* 20**,** 570-575.
81. ELLISON, G.N., *Thermal Computations for Electronic Equipment*. 1989, Van Nostrand Reinhold: New York.
82. RAO, L.&NEWMAN, J. 1997. Heat-generation rate and general energy balance for insertion battery systems. *Journal of the Electrochemical Society,* 144**,** 2697-2704.
83. SMITH, K.&WANG, C.Y. 2006. Power and thermal characterization of a lithium-ion battery pack for hybrid-electric vehicles. *Journal of Power Sources,* 160**,** 662-673.
84. ZHU, C., LI, X., SONG, L.&XIANG, L. 2013. Development of a theoretically based thermal model for lithium ion battery pack. *Journal of Power Sources,* 223**,** 155-164.
85. LEAL, L.G. 2007. *Advanced transport phenomena : fluid mechanics and convective transport processes,* New York, Cambridge University Press.
86. NAGASUBRAMANIAN, G. 2001. Electrical characteristics of 18650 Li-ion cells at low temperatures. *Journal of Applied Electrochemistry,* 31**,** 99-104.
87. PLICHTA, E.J.&BEHL, W.K. 2000. Low-temperature electrolyte for lithium and lithium-ion batteries. *Journal of Power Sources,* 88**,** 192-196.

88. SMART, M.C., RATNAKUMAR, B.V.&SURAMPUDI, S. 1999. Electrolytes for Low-Temperature Lithium Batteries Based on Ternary Mixtures of Aliphatic Carbonates. *Journal of the Electrochemical Society,* 146**,** 486-492.
89. EIN-ELI, Y., MCDEVITT, S.F.&LAURA, R. 1998. The superiority of asymmetric alkyl methyl carbonates. *Journal of the Electrochemical Society,* 145**,** L1-L3.
90. SMART, M.C., RATNAKUMAR, B.V., WHITCANACK, L.D., CHIN, K.B., SURAMPUDI, S., CROFT, H., TICE, D.&STANIEWICZ, R. 2003. Improved low-temperature performance of lithium-ion cells with quaternary carbonate-based electrolytes. *Journal of Power Sources,* 119-121**,** 349-358.
91. SHIAO, H.C., CHUA, D., LIN, H.P., SLANE, S.&SALOMON, M. 2000. Low temperature electrolytes for Li-ion PVDF cells. *Journal of Power Sources,* 87**,** 167-173.
92. HERREYRE, S., HUCHET, O., BARUSSEAU, S., PERTON, F., BODET, J.M.&BIENSAN, P. 2001. New Li-ion electrolytes for low temperature applications. *Journal of Power Sources,* 97-98**,** 576-580.
93. SMART, M.C., RATNAKUMAR, B.V., CHIN, K.B.&WHITCANACK, L.D. 2010. Lithium-ion electrolytes containing ester cosolvents for improved low temperature performance. *Journal of the Electrochemical Society,* 157**,** A1361-A1374.
94. SMART, M.C., LUCHT, B., DALAVI, S., KRAUSE, F.&RATNAKUMAR, B. 2012. The Effect of Additives upon the Performance of MCMB/LiNixCo1-xO2 Li-Ion Cells Containing Methyl Butyrate-Based Wide Operating Temperature Range Electrolytes. *J. Electrochem. Soc.,* 159**,** A739-A751.
95. SMART, M.C., RATNAKUMAR, B.V.&SURAMPUDI, S. 2002. Use of organic esters as cosolvents in electrolytes for lithium-ion batteries with improved low temperature performance. *Journal of the Electrochemical Society,* 149**,** A361-A370.
96. ZHANG, S.S., XU, K., ALLEN, J.&JOW, T. 2002. Effect of propylene carbonate on the low temperature performance of Li-ion cells. *J. Power Sources,* 110**,** 216-221.
97. WANG, C., APPLEBY, A.J.&LITTLE, F.E. 2002. Low-temperature characterization of lithium-ion carbon Anodes via microperturbation measurement. *Journal of the Electrochemical Society,* 149**,** A754-A760.
98. FAN, J. 2003. On the discharge capability and its limiting factors of commercial 18650 Li-ion cell at low temperatures. *Journal of Power Sources,* 117**,** 170-178.
99. SURESH, P., SHUKLA, A.&MUNICHANDRAIAH, N. 2002. Temperature dependence studies of a.c. impedance of lithium-ion cells. *J. Appl. Electrochem.,* 32**,** 267-273.
100. ZHANG, S.S., XU, K.&JOW, T.R. 2002. A new approach toward improved low temperature performance of Li-ion battery. *Electrochemistry Communications,* 4**,** 928-932.
101. ZHANG, S.S., XU, K.&JOW, T.R. 2003. Low-temperature performance of Li-ion cells with a LiBF4-based electrolyte. *Journal of Solid State Electrochemistry,* 7**,** 147-151.
102. ZHANG, S.S., XU, K.&JOW, T.R. 2003. The low temperature performance of Li-ion batteries. *Journal of Power Sources,* 115**,** 137-140.
103. ZHANG, S.S., XU, K.&JOW, T.R. 2006. An improved electrolyte for the LiFePO4 cathode working in a wide temperature range. *Journal of Power Sources,* 159**,** 702-707.
104. JANSEN, A.N., DEES, D.W., ABRAHAM, D.P., AMINE, K.&HENRIKSEN, G.L. 2007. Low-temperature study of lithium-ion cells using a LiySn micro-reference electrode. *Journal of Power Sources,* 174**,** 373-379.
105. ABRAHAM, D., HEATON, JR., KANG, S., DEES, D.&JANSEN, A. 2008. Investigating the low-temperature impedance increase of lithium-ion cells. *J. Electrochem. Soc.,* 155**,** A41-A47.
106. HUANG, C.K., SAKAMOTO, J.S., WOLFENSTINE, J.&SURAMPUDI, S. 2000. Limits of low-temperature performance of Li-ion cells. *Journal of the Electrochemical Society,* 147**,** 2893-2896.

107. LIN, H.P., CHUA, D., SALOMON, M., SHIAO, H.C., HENDRICKSON, M., PLICHTA, E.&SLANE, S. 2001. Low-temperature behavior of Li-ion cells. *Electrochemical and Solid-State Letters,* 4**,** A71-A73.
108. ZHANG, S.S., XU, K.&JOW, T.R. 2006. Charge and discharge characteristics of a commercial LiCoO2-based 18650 Li-ion battery. *Journal of Power Sources,* 160**,** 1403-1409.
109. SIDES, C.R.&MARTIN, C.R. 2005. Nanostructured electrodes and the low-temperature performance of li-ion batteries. *Advanced Materials,* 17**,** 125-128.
110. ALLEN, J.L., JOW, T.R.&WOLFENSTINE, J. 2006. Low temperature performance of nanophase Li4Ti5O12. *Journal of Power Sources,* 159**,** 1340-1345.
111. LIAO, X., MA, Z., GONG, Q., HE, Y., PEI, L.&ZENG, L. 2008. Low-temperature performance of LiFePO4/C cathode in a quaternary carbonate-based electrolyte. *Electrochem. Commun.,* 10**,** 691-694.
112. FAN, J.&TAN, S. 2006. Studies on charging lithium-ion cells at low temperatures. *Journal of the Electrochemical Society,* 153**,** A1081-A1092.
113. GU, W.B.&WANG, C.Y. 2000. Thermal-Electrochemical Modeling of Battery Systems. *Journal of The Electrochemical Society,* 147**,** 2910-2922.
114. AMIRIBAVANDPOUR, P., SHEN, W., MU, D.&KAPOOR, A. 2015. An improved theoretical electrochemical-thermal modelling of lithium-ion battery packs in electric vehicles. *Journal of Power Sources,* 284**,** 328-338.
115. JI, Y., ZHANG, Y.&WANG, C.Y. 2013. Li-ion cell operation at low temperatures. *Journal of the Electrochemical Society,* 160**,** A636-A649.
116. NEWMAN, J.&TIEDEMANN, W. 1975. Porous-electrode theory with battery applications. *AIChE Journal,* 21**,** 25-41.
117. SAFARI, M.&DELACOURT, C. 2011. Modeling of a commercial graphite/LiFePO 4 cell. *Journal of the Electrochemical Society,* 158**,** A562-A571.
118. DARLING, R.&NEWMAN, J. 1997. Modeling a porous intercalation electrode with two characteristic particle sizes. *Journal of the Electrochemical Society,* 144**,** 4201-4208.
119. NEWMAN, J.&THOMAS-ALYEA, K.E. 2012. *Electrochemical Systems,* Hoboken, Wiley.
120. DE VIDTS, P., DELGADO, J., WU, B., SEE, D., KOSANOVICH, K.&WHITE, R.E. 1998. A nonisothermal nickel-hydrogen cell model. *Journal of the Electrochemical Society,* 145**,** 3874-3883.
121. BOTTE, G.G., JOHNSON, B.A.&WHITE, R.E. 1999. Influence of some design variables on the thermal behavior of a lithium-ion cell. *Journal of the Electrochemical Society,* 146**,** 914-923.
122. KUZMINSKII, Y.V., NYRKOVA, L.I.&ANDRIIKO, A.A. 1993. Heat generation of electrochemical systems Batteries. *Journal of Power Sources,* 46**,** 29-38.
123. KUZ'MINSKII, Y.V.&GORODYSKII, A.V. 1988. Thermal analysis of electrochemical reactions. Part I. Kinetic method of determining Peltier heats. *Journal of Electroanalytical Chemistry,* 252**,** 21-37.
124. NEWMAN, J. 1995. Thermoelectric effects in electrochemical systems. *Industrial & Engineering Chemistry Research,* 34**,** 3208-3216.
125. LAMPINEN, M.J.&FOMINO, M. 1993. Analysis of free energy and entropy changes for half-cell reactions. *Journal of the Electrochemical Society,* 140**,** 3537-3546.
126. XU, Q., KJELSTRUP, S.&HAFSKJOLD, B. 1998. Estimation of single electrode heats. *Electrochimica Acta,* 43**,** 2597-2603.
127. GIBBARD, H.F. 1978. THERMAL PROPERTIES OF BATTERY SYSTEMS. *Journal of the Electrochemical Society,* 125**,** 353-358.
128. LI, J., CHENG, Y., JIA, M., TANG, Y., LIN, Y., ZHANG, Z.&LIU, Y. 2014. An electrochemical-thermal model based on dynamic responses for lithium iron phosphate battery. *Journal of Power Sources,* 255**,** 130-143.
129. PATANKAR, S. 1980. *Numerical Heat Transfer and Fluid Flow,* New York, CRC Press.

130. ZENG, Y., ALBERTUS, P., KLEIN, R., CHATURVEDI, N., KOJIC, A., BAZANT, M.Z.&CHRISTENSEN, J. 2013. Efficient conservative numerical schemes for 1D nonlinear spherical diffusion equations with applications in battery modeling. *Journal of the Electrochemical Society,* 160**,** A1565-A1571.
131. PRADA, E., DI DOMENICO, D., CREFF, Y., BERNARD, J., SAUVANT-MOYNOT, V.&HUET, F. 2012. Simplified Electrochemical and Thermal Model of LiFePO4-Graphite Li-Ion Batteries for Fast Charge Applications. *Journal of The Electrochemical Society,* 159**,** A1508-A1519.
132. WANG, W.Y., LUO, G.H., WEI, F.&LUO, J. 2009. Electrical conductivity and thermal properties of acrylonitrile-butadiene- styrene filled with multiwall carbon nanotubes. *Polymer Engineering and Science,* 49**,** 2144-2149.
133. VALØEN, L.O.&REIMERS, J.N. 2005. Transport properties of LiPF6-based Li-Ion battery electrolytes. *Journal of the Electrochemical Society,* 152**,** A882-A891.
134. CHEN, M., ZHOU, D., CHEN, X., ZHANG, W., LIU, J., YUEN, R.&WANG, J. 2015. Investigation on the thermal hazards of 18650 lithium ion batteries by fire calorimeter. *Journal of Thermal Analysis and Calorimetry,* 122**,** 755-763.
135. WU, P., ROMBERG, J., FENG, X., ZHANG, M., LU, L., HE, X.&OUYANG, M., *Thermal runaway propagation within module consists of large format Li-Ion cells*, in *Lecture Notes in Electrical Engineering*. 2016. p. 117-123.
136. SCHUSTER, E., ZIEBERT, C., MELCHER, A., ROHDE, M.&SEIFERT, H.J. 2015. Thermal behavior and electrochemical heat generation in a commercial 40 Ah lithium ion pouch cell. *Journal of Power Sources,* 286**,** 580-589.
137. STORAGE, E., accessed in 20 Feb 2016,http://www.mute-automobile.de.
138. INCROPERA, F.P.&DEWITT, D.P. 1996. *Fundamentals of Heat and Mass Transfer,* New York, John Wiley & Sons.
139. FAN, J. 2004. Studies of 18650 cylindrical cells made with doped linio2 positive electrodes for military applications. *Journal of Power Sources,* 138**,** 288-293.
140. SMART, M.C., RATNAKUMAR, B.V., SURAMPUDI, S., WANG, Y., ZHANG, X., GREENBAUM, S.G., HIGHTOWER, A., AHN, C.C.&FULTZ, B. 1999. Irreversible capacities of graphite in low-temperature electrolytes for lithium-ion batteries. *Journal of the Electrochemical Society,* 146**,** 3963-3969.
141. RATNAKUMAR, B.V., SMART, M.C.&SURAMPUDI, S. 2001. Effects of SEI on the kinetics of lithium intercalation. *Journal of Power Sources,* 97-98**,** 137-139.
142. ZHANG, S.S., XU, K.&JOW, T.R. 2002. Low temperature performance of graphite electrode in Li-ion cells. *Electrochimica Acta,* 48**,** 241-246.
143. NEWMAN, J.S. 1991. *Electrochemical Systems*.
144. JOW, T.R., MARX, M.B.&ALLEN, J.L. 2012. Distinguishing Li + charge transfer kinetics at NCAelectrolyte and graphite-electrolyte interfaces, and NCAelectrolyte and LFPelectrolyte interfaces in Li-ion cells. *Journal of the Electrochemical Society,* 159**,** A604-A612.
145. SHARAFI, A., MEYER, H.M., NANDA, J., WOLFENSTINE, J.&SAKAMOTO, J. 2016. Characterizing the Li-Li7La3Zr2O12 interface stability and kinetics as a function of temperature and current density. *Journal of Power Sources,* 302**,** 135-139.